Laser Fabrication of Microstructured Polymer-based Ultra Thin Layer Chromatography Platforms

Rónán McCann B.Sc. (Hons.)

May 22, 2018

A thesis submitted for the degree of
Philosophiæ Doctor (Ph.D.)
from
Dublin City University,
School of Mechanical & Manufacturing Engineering,
Faculty of Engineering & Computing

Supervisor: Prof. Dermot Brabazon of Dublin City University
Co-supervisors: Dr. Mercedes Vázquez & Prof. Apryll Stalcup

Declaration

I hereby certify that this material, which I now submit for assessment on the programme of study leading to the award of PhD, is entirely my own work, and that I have exercised reasonable care to ensure that the work is original, and does not to the best of my knowledge breach any law of copyright, and has not been taken from the work of others save and to the extent that such work has been cited and acknowledged within the text of my work.

Signed: _____ (Candidate) ID No.: 55455189 Date: 22/05/2018

Rónán McCann, B.Sc. (Hons.)

Advanced Processing Technology Research Centre,
School of Mechanical and Manufacturing Engineering,
Faculty of Engineering and Computing

&

Irish Separation Science Cluster,
National Centre for Sensor Research

&

National Centre for Plasma Science and Technology

Publication Declaration

Supplementary to the previous declaration, I hereby declare that this thesis contains information from three original manuscripts published in peer-reviewed journals and one currently under preparation for submission. The theme of this thesis is the laser fabrication of polymer platforms for application in planar chromatography. To that end, investigations into the polymer processing via laser ablation were performed first, which form a basis for the ongoing work.

The ideas, direction and implementation of the research, and authorship of the manuscripts were entirely the work of myself while a student in the School of Mechanical and Manufacturing Engineering under the supervision of Prof. Dermot Brabazon.

The inclusion of co-authors reflects the fact that this work was produced while working in a dynamic, multi-disciplinary research group with input from the various group members at all stages. This inclusion does not prejudice my contribution but rather highlights the collaborative spirit of the members of the Advanced Processing Technology Research Centre, Irish Separation Science Cluster and National Centre for Plasma Science and Technology.

With regards to Chapters Three, Four, Five and Six, my contribution to the resulting publications were the following:

Chapter	Publication Title	Publication Status	Nature and Extent of Candidate's Contribution
3	"Microchannel fabrication on cyclic olefin polymer substrates via 1064nm Nd:YAG laser ablation"	Published, App. Surf. Sci., 2015	First author, experiment design, data collection and analysis, primary manuscript author.
4	"Taguchi method modelling of Nd:YAG laser ablation of microchannels on cyclic olefin polymer films	Published, Opt. Laser. Technol. 2018	First author, experiment design, data collection and analysis, primary manuscript author.
5	"Pulsed laser deposition of plasmonic nanostructured gold on flexible transparent polymers at atmospheric pressure"	Published, J. Phys. D., 2017	First author, experiment design, data collection and analysis, primary manuscript author.
6	"Direct laser fabrication of microstructured cyclic olefin polymer-based planar chromatography platforms"	Manuscript under preparation	First author, experiment design, data collection and analysis, primary manuscript author.

Signed: _____ ID No.: 55455189 Date: 22/05/2018

Mr. Ronán McCann

Signed: _____ Date: _____

Prof. Dermot Brabazon

List of Publications

Journal Publications:

1. Bagga K, McCann R, Wang M, Stalcup A, Vázquez M, Brabazon D. Laser assisted synthesis of carbon nanoparticles with controlled viscosities for printing applications. J Colloid Interface Sci;447:263–8.
2. McCann R, Bagga K, Groarke R, Stalcup A, Vázquez M, Brabazon D. Microchannel fabrication on cyclic olefin polymer substrates via 1064 nm Nd:YAG laser ablation. Appl Surf Sci;387:603–8.
3. Bagga K, McCann R, O'Sullivan F, Ghosh P, Krishnamurthy S, Stalcup A, Vázquez M, Brabazon D. Nanoparticle functionalized laser patterned substrate: an innovative route towards low cost biomimetic platforms. RSC Adv;7(13):8060–9.
4. McCann R, Bagga K, McCarthy E, Groarke R, Al-Hamaoy A, Stalcup A, Vázquez M, Brabazon D. Carbon Nanoparticle Functionalization of Laser Textured Polymer Surfaces for Chemical and Biological Speciation. Lasers Eng. 2017;36(1–3):63–72.
5. McCann R, Hughes C, Bagga K, Stalcup A, Vázquez M, Brabazon D. Pulsed laser deposition of plasmonic nanostructured gold on flexible transparent polymers at atmospheric pressure. J Phys D Appl Phys. 2017;50(24):245303.
6. McCann R, Bagga K, Duaux G, Stalcup A, Vázquez M, Brabazon D. Taguchi method modelling of Nd:YAG laser ablation of microchannels on cyclic olefin polymer film. Opt Laser Technol. 2018;106:265-71
7. Hughes C, McCann R, Eguileor J, Bagga K, Stalcup A, Groarke R, Vázquez M, Brabazon D. Modelling and optimisation of single-step laser-based gold nanostructure deposition with tunable optical properties. Opt Laser

Technol. (Accepted)

Conference Proceedings Papers:

1. McCann R, Bagga K, Stalcup A, Vázquez M, Brabazon D. "Laser micro-engineering of functionalised cyclic olefin polymers for microfluidic applications", Proc. SPIE 9351, Laser-based Micro- and Nanoprocessing IX, 93511N.
2. Bagga K, McCann R, Brasi Q, Coussy J, Stalcup A, Vázquez M, Brabazon D. "Laser-assisted synthesis of ultrapure nanostructures for biological sensing applications", Proc. SPIE 9928, Nanobiosystems: Processing, Characterization, and Applications IX, 99280O.

Oral Presentations:

1. McCann R, Bagga K, McCarthy E, Groarke R, Al-Hamaoy A, Stalcup A, Vázquez M, Brabazon D. "Carbon nanoparticle functionalisation of laser textured polymer surfaces for chemical and biological speciation" 38th Matador Conference, Taipei, ROC.
2. McCann R, Hughes C, Bagga K, Stalcup A, Vázquez M, Brabazon D. "Picosecond Nd:YAG laser ablation of cyclic olefin polymer substrates for sensing platform fabrication" ICASS 2015, 27 – 30 July 2015, Shanghai, PRC.
3. McCann R, Bagga K, Stalcup A, Vázquez M, Brabazon D. "Single-step laser deposition of nanostructured gold thin films on flexible polymer substrates" 20th International ESAFORM Conference on Material Forming, 26 – 28 April 2017, Dublin, Ireland.
4. McCann R, Delaney B, Bagga K, Stalcup A, Vázquez M, Costello J T, Brabazon D. "Single-step laser deposition of nanostructured gold thin films on flexible polymer substrates" Photonics Ireland, 13 – 15 September 2017, Galway, Ireland

Poster Presentations:

1. McCann R, Bagga K, Peissker T, Xiaoyun H, Fox E, Grandjean D, van Bael M, Lievens P, Stalcup A, Vázquez M, Brabazon D. "Deposition of gold-

platinum nanoclusters onto thin film chromatography polymeric sheers for sensing applications" Analytical Research Forum 2014, London UK

2. Bagga K, McCann R, Stalcup A, Vázquez M, Brabzon D. "Laser micro-engineering of functionalised cyclic olefin polymers for microfluidic applications" SPIE Photonics West 2015, San Francisco, USA.
3. McCann R, Bagga K, Stalcup A, Vázquez M, Brabzon D. "Characterisation of laser-textured and carbon nanoparticle coated polymer surfaces" NANOSMAT 2015, Dublin, Ireland.
4. McCann R, Bagga K, Stalcup A, Vázquez M, Brabzon D. "Confined atmospheric pulsed laser deposition of nanostructured ultrathin films" International Conference on Laser Ablation 2015, 31 Aug – 4 Sept, Cairns, Australia.
5. McCann R, Hughes C, Freeland B, Bagga K, Groarke R, Stalcup A, Vázquez M, Brabzon D. "Confined atmospheric pulsed laser deposition: A new route to nanostructured ultrathin films" IOP Spring Meeting 2016, Belfast, Northern Ireland.
6. Freeland B, Bagga K, McCann R, McCarthy É, Foley G, O'Kennedy R, Brabazon. "Laser assisted synthesis of carbon nanostructures with controlled viscosity for printing and biological sensing applications" ANGEL, 9–12 May 2016, Essen, Germany.
7. Hughes C, McCann R, Bagga K, Groarke R, Regan F, Barron N, Brabazon D. "Pulsed laser ablation (PLA) and confined atmospheric-pulsed laser deposition (CA-PLD) based nano-biosensor production" Biosensors 2016, 25-27 May 2016, Gothenburg, Sweden.
8. Bagga K, McCann R, Brasi Q, Coussy J, Stalcup A, Vázquez M, Brabzon D. "Laser-assisted synthesis of ultrapure nanostructures for biological sensing applications" SPIE Optics + Photonics, 28 Aug – 1 Sept 2016, San Diego, USA.
9. McCann R, Bagga K, Groarke R. Stalcup A, Vázquez M, Brabzon D. "Laser fabricated cyclic olefin polymer-based ultra thin layer chromatography platforms" 31st International Symposium on Chromatography, 28 Aug – 1 Sept 2016, Cork, Ireland.
10. Groarke R, Skrobisz T, Hughes C, McCann R, Scigliano A, Brabazon D. "Next Generation High Performance Thin Layer Chromatography (HP-

TLC) Using Additively Manufactured Acrylate Based Polymer Stationary Phases" 31st International Symposium on Chromatography, 28 Aug – 1 Sept 2016, Cork, Ireland.

11. Hughes C, McCann R, Ul Ahad I, Bagga K, Regan F, Brabazon D. "Metal Nanostructured Film Deposition on Flexible Polymer" 20th International ESAFORM Conference, 26 – 28 Apr 2017, Dublin, Ireland.
12. Bagga K, McCann R, Vázquez M, Brabazon D "'Green' laser-based synthesis nanoparticles towards waste water treatment applications" 7th International Colloids Conference, 18-21 Jun 2017, Barcelona, Spain.
13. Freeland B, McCann R, Bagga K, Pulito P, Nogue A, Foley G, Brabazon D. "Optimisation of Multi-wavelength continuous nanoparticle fabrication via Pulsed Laser Ablation in Liquids" International Conference on Laser Ablation 2017, 3 – 8 Sept 2017, Marseille, France.

Dedication

To my mother Deirdre, for instilling in me the value of a good education, and to my father Austin, the best engineer I know.

Acknowledgments

First and foremost, thank you to Prof. Dermot Brabazon for your guidance and encouragement throughout the last four years. You constantly pushed me to be a better student, and I have learnt much about how to be a researcher, a scientist and an engineer from you for which I am very grateful.

To my co-supervisors Prof. Apryll Stalcup and Dr. Mercedes Vázquez, thank you for all the productive conversations throughout the project. Your insights and outside perspectives were invaluable to the work, and I am thankful for all the time and support you gave me.

To Dr. Komal Bagga, thank for you teaching me everything you know about lasers and nanoparticles. Every day was a pleasure to work with you, even when things were getting stressful in the lab.

To all who I have had a pleasure to work alongside – Rob, Cian, Inam, Éanna, Shadi, Muhannad, Inam, and all past and present members of APT, thank you for all your help through the years. My special thanks to Brian and Paul – if ever the was a problem to fix, or a coffee to drink you both were there to make being in the lab more enjoyable. The funding for this project came from Science Foundation Ireland, and my thanks to them for providing the opportunity to undertake this project.

Many thanks to Dr. Dorota Wencel in the School of Physical Sciences and Michael May, Alan Meehan and Liam Domican in the School of Mechanical and Manufacturing Engineering, and all the technical staff for showing me the ropes of the equipment used during the project and lending a hand when needed. Thanks to all the administration staff, in particular Sheila Boughton, Caoimhe O'Broin, and Suzanne Dockery, for helping me along the way.

Having a wealth of friends to work with makes every day something to look forward to. To Adam, Aoife, Ben, Cezar, Claire, Cleo, Conor, David, Huw and Stephen, thank you for the help (and distraction!) when needed over the years. My

special thanks to Prof. Bert Ellingboe in the Plasma Research Laboratory - I am positive that without your coffee machine this thesis would not have been finished!

To my friends Brian, Singo, Jimmy, Eamonn, Dónall, Kev, Louis, Dave, Jen, Deco and Shimbo and many others – thank you for your years friendship, for keeping me sane when things get a bit crazy, and for putting up with my bad puns!

To Paul, none of this would have been possible without your constant encouragement. You showed me what's important in life and you make every moment together something special. You make me a better person, and there are no words to describe how grateful I am to have you in my life.

To my siblings, Saoirse, Ciarán, Linus and Ting Ting, we are sometimes separated by half the world, but it never feels that way. Even when times are tough, we are there to help each other, to make each other smile, (and occasionally get on each other's nerves!) – I am lucky to have such a fantastic family to go home to.

And finally, to my parents Austin and Deirdre, I cannot begin to count the ways in which you have helped me throughout my life. You always pushed me to better myself. I am who I am today because of your guidance and patience, and for that I am enterally grateful. I dedicate this work to you both.

Table of Contents

List of Figures

List of Tables

Abstract

Rónán McCann

Laser Fabrication of Microstructured Polymer-based Ultra Thin Layer Chromatography Platforms

This thesis presents an investigation into the fabrication and characterisation of microstructured Ultra Thin Layer Chromatography (UTLC) systems and their application towards chemical separation. These systems were fabricated using laser direct-write processing of polymer substrates.

ULTC systems, which are becoming a topic of increasing interest in the fields of nanomaterials and chromatography, employ substrates with porous functional layers for chemical separation which are typically on the order of 10 µm thick. Techniques for fabrication of the sorbent layer include atomic layer deposition, polymer electrospinning and sol-gel deposition. Though these processes are capable of both deposition of materials with the required functionality, and creation of feature sizes on the scales needed for UTLC, they are high cost and have low-throughput. Contrastingly, laser direct-write processing offers an adaptable, scalable, environmentally-friendly and cost-effective method for rapid fabrication of micron-scale features on various substrates.

Cyclic Olefin Polymer (COP), was chosen as the substrate material based on its superior optical properties and chemical resistance compared to other polymers commonly used in analytical applications. Microchannels were fabricated on COP substrates via laser ablation utilising a 1064 nm Nd:YAG solid-state laser. The ability to create microchannels ranging from 20 to 120 µm deep and 60 to 160 µm wide was demonstrated. An investigation into modelling of this ablation process was also presented. A route towards the single-step functionalisation of COP via a novel atmospheric pulsed laser deposition process was also examined.

Towards the development of a UTLC platform, the flow behaviour of different microstructured surfaces was examined. A 45° crosshatched microchannel design was chosen and the effectiveness of this platform when compared with commercially available platforms examined. The separation on the COP's native functionality is also compared with that of the COP after two surface modifications: an oxygen plasma treatment and silanisation via (3-Aminopropyl)triethoxysilane (APTES) exposure.

Chapter 1
Introduction

1.1 Motivation

This thesis presents the development of a new planar analytical chromatography platform fabricated via laser material processing. The term “chromatography” refers to a branch of analytical chemistry concerned with the physical separation of mixed, multi-component samples into its individual constituents, known as analytes [1]. This separation can be used as a form of purification prior to the sample later utilisation in which case it is referred to as Preparative Chromatography. Alternatively, if the purpose of the separation is to aid in the identification of the analytes within the sample it is referred to as Analytical Chromatography [2].

Within chromatography, there are a number of individual techniques which are distinguished by the matter phase of the sample during separation, such as Gas Chromatography (GC) or Liquid Chromatography (LC). Though frequently overlooked in favour of competing techniques such as LC, GC or their modern variants, Thin Layer Chromatography (TLC) performed in the liquid phase is distinguished by being performed using thin porous layers coated on inert substrates [3]. TLC remains the technique of choice in a number of areas where low cost, or fast development and optimisation times are required, such as method development for LC separations.

Though approaching a century old, TLC is undergoing a recent resurgence of interest being driven by a number of research groups globally [4,5]. This renewed appeal is in part due to the application of nanomaterials and advanced manufacturing techniques to fabricate novel platforms for planar separations. When these nanomaterial planar platforms are applied towards separations, the technique is

commonly referred to as Ultra Thin Layer Chromatography (UTLC). The use of these novel nanomaterials allows the fabricated platforms to have unique capabilities, outperforming those of traditional commercial TLC plates with UTLC having faster separations and requiring less sample and reagent volumes.

As analytical devices have reduced in size, the required volumes of samples and reagents have also reduced. This makes the devices very cost-effective to use, however the reduced manufacturing dimensions can pose a challenge to fabricate. To-date, the fabrication of UTLC devices have focussed on utilising advanced materials and manufacturing techniques such as Chemical Vapour Deposition, Atomic Layer Deposition and Nanowire Electrospinning. Though these techniques are excellently suited to the fabrication of advanced nanomaterials, for this application they are not considered rapid or low-cost manufacturing methods.

Conversely, laser material processing is suited towards both the rapid development and low-cost manufacture of polymer-based analytical devices. Therefore, the objective of this thesis is to examine the use of laser manufacturing towards the fabrication of a UTLC platform.

1.2 Research Thesis and Objectives

The primary supposition of this thesis is that:

A technique based around laser-material processing can be developed such that microstructured planar chromatographic platforms can be fabricated which are effective relative to commercial platforms, as evidenced by proof-of-concept applications of said platforms for organic chemical separations.

This aim of the thesis was achieved through a number of objectives:

1. The identification of a laser-based approach capable of the fabrication of micron-sized structures on the surface of a polymer which is compatible with common chromatographic solvents and reagents.
2. The full characterisation of the laser process and resultant substrate morphology and surface chemistry.
3. Examination of potential routes for functionalisation of the chromatographic platforms.

4. Application of the platform for proof-of-concept separations and comparison of results with commercial TLC plates.

1.3 Overview of work and thesis structure

This thesis is comprised of seven chapters: Chapter 1 introduces this work and provides context for the following chapters. Chapter 2 will present an introduction to the theory and core-concepts of TLC and present an overview of the areas of active research in UTLC. As a laser-based fabrication approach is being investigated, the capabilities of laser fabrication techniques towards the production of nano- and micron-sized features on polymers is also presented. Finally, some alternative and complimentary material processing techniques which can also achieve the desired feature sizes are discussed.

Chapter 3 presents the use of laser ablation using an infrared laser to fabricate microchannels on a cyclic olefin polymer substrate. A detailed examination of channel morphology, changes in surface chemistry and the effect of process parameters on microchannel dimensions is reported.

In Chapter 4, the development of a model suitable for predicting microchannel depth and width is presented. A Design of Experiments approach, based on the Taguchi Method, is used to produce a model for the prediction of microchannel width and depth on three different grades of cyclic olefin polymer. The robustness of the model and the produced microchannel morphology are discussed in the context of model predictive control of laser ablation of microchannel on polymer substrates.

In Chapter 5, the possibility of utilising a novel method of atmospheric pulsed laser deposition to functionalise polymer substrates is presented. Gold was used as the test material, deposited at a range of laser conditions. Full characterisation was performed on the substrate after deposition, including examination of surface morphology, surface chemistry and the crystalline structure of the deposited gold material.

In Chapter 7, the laser-fabricated platforms are applied towards the separation of organic dyes. The design of a laser fabricated, polymer UTLC plate is presented. Flow behaviours and sample application characteristics were investigated, and the capabilities of the platform compared to commercially available TLC plates. Subsequent routs of chemical and plasma surface modification, and the effect of the modification on the separation capabilities were also examined.

Chapter 8 concludes the thesis and presents an outlook as to where the output from this thesis can lead and what further work is needed in this research domain.

References

[1] Touchstone JC, Dobbins MF. Practice of Thin Layer Chromatography. 2nd ed. New York: John Wiley & Sons, Inc.; 1983.

[2] Wall PE. Thin-Layer Chromatography. Thin-Layer Chromatography: A Modern Practical Approach. Cambridge: Royal Society of Chemistry; 2005.

[3] Spangenberg B, Poole CF, Weins C. Quantitative Thin-Layer Chromatography. Berlin, Heidelberg: Springer Berlin Heidelberg; 2011.

[4] Poole C. Instrumental Thin-Layer Chromatography. Amsterdam: Elsevier B.V.; 2015.

[5] Patel RB, Gopani MC, Patel MR. UTLC: An Advanced Technique in Planar Chromatography. Chromatographia. 2013 Jun 8;76(19–20):1225–31.

Chapter 2
Theory, background and state of the art

This chapter will present a broad overview of the core-concepts and principles of TLC and how it is utilised as an analytical technique. Fabrication techniques for TLC platforms are also discussed as well as more recent advances in thin layer chromatography such as Ultra-Thin Layer Chromatography (UTLC).

Alternative fabrication techniques including laser processing and plasma processing are presented. These techniques are discussed in the context of fabrication of micron-scale features. Though these techniques have yet to be applied to UTLC plate fabrication, their ability to create features on the scale required makes them suitable candidate processes for examination. Special attention will be given to laser processing as this is the fabrication technique which was chosen in this thesis. Finally, the suitability of laser processing as a route toward UTLC plate fabrication is discussed.

2.1 Principles of Thin Layer Chromatography

Planar chromatography is a group of analytical techniques for chemical and biological separation performed on planar substrates. Planar chromatography has two main branches: (1) Paper Chromatography, performed on paper substrates, and (2) TLC and derivatives of TLC such as High-Performance Thin Layer Chromatography (HP-TLC) and later UTLC. TLC differs from paper chromatography as the separation is performed on a substrate coated with a porous sorbent material [1,2]. These techniques contrast with Liquid Chromatography (LC) which is conducted under high pressure in a column packed with a porous sorbent material. TLC has been applied for both

qualitative and quantitative analysis in a variety of fields from environmental [3] and forensic analysis [4] to food [5] and pharmaceutical quality assurance testing [6].

TLC separation systems are fabricated on an inert planar substrate, referred to as a "plate" (typically made from glass, aluminium foil or polycarbonate) which is coated with a porous sorbent layer known as the "stationary phase". The typical analytical protocol is shown in Figure 2.1. Analysis is performed by spotting a liquid sample on one end of the plate, away from the plate edge, typically 5 – 10 mm. The spotted plate is dried and then placed in contact with a solvent, known as the "mobile phase", in a sealed chamber to prevent evaporation. This mobile phase moves through the sorbent layer via capillary action and separation occurs via differential interactions of the individual analytes in the sample with the stationary phase as compared to the mobile phase.

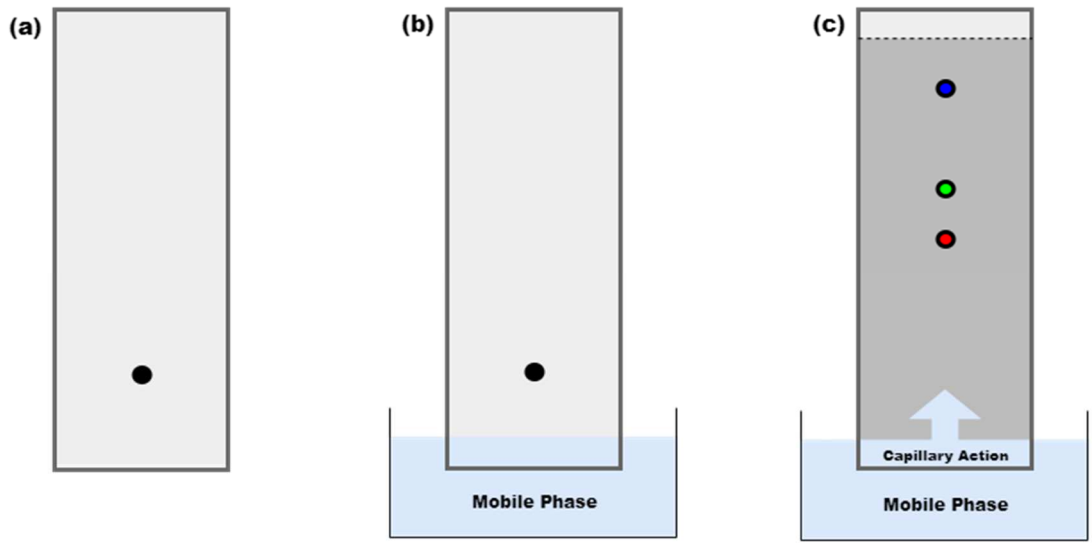

Figure 2.1: The typical TLC protocol: (a) the sample is spotted on the TLC plate (black spot) and dried, (b) the plate is introduced to the mobile phase and (c) the mobile phase moves though the stationary phase via capillary action, with separation of the sample components (blue, green and red spots) occurring over the length of the plate.

Historically, TLC was first described as "Spot Chromatography" which was applied for the separation of plant extracts [7], but the technique did not gain recognition until 1949 when it was applied to the separation of terpene compounds in essential oils [8]. Initially TLC suffered from large experimental errors, due in part to lack of sorbent layer reproducibility from plate to plate. As plate fabrication

techniques became more robust these experimental errors were reduced, making TLC a viable alternative to liquid chromatographic techniques.

2.1.1 Stationary Phase

Silica is by far the most commonly used stationary phase, with coatings comprised of particles on the order of tens of microns. Silica stationary phases are available as polar or non-polar functionalized preparations, though there are many different stationary phases available suited to specific separations. Table 2.1 lists some of the most common applications for commercially produced stationary phases. A binder such as a calcium sulphate or polyvinyl compound is typically employed for the sorbent layer to adhere to the substrate and is combined with the stationary phase during coating. Substrate materials commonly used are thin glass, inert polymer or aluminium sheets. The resultant coatings typically have a porous structure with macropores diameters of approximately 1 – 2 μm and mesopores of diameters ranging from 4 – 8 nm diameters for silica gel layers [9,10]. Various preparations of silica gel impregnated with other materials are also available for enhanced detection (such as fluorescent detection) or selective separation of specific compounds [1].

The exact retention mechanism which results in analyte separation can vary depending on the sorbent layer material and required application. There are three main physicochemical processes exploited in TLC: adsorption, partition and ion exchange [11].

Adsorption occurs in TLC when contact is made between the analytes and the stationary phase. This adsorption is driven by mechanisms such as van der Waal forces and dipole interactions. In TLC, the adsorption must be physical (as opposed to chemical) to allow analytes to reversibly interact with the stationary phase at differing rates. Analytes with high affinity for the stationary phase will bind to the sorbent layer and thus be retained preferentially. Those with lower affinities for the stationary phase will bind more weakly and will tend towards remaining in the mobile phase and therefore travelling further from the initial spot position. Adsorption is the primary mode of separation for silica gel, aluminium oxide and magnesium silicate stationary phases, and is suited for separation of hydrophobic substances with a low or medium polarity [1].

Partition mode separations are governed by the hydrophobicity of the analytes with respect to the mobile phase. In this mode, the mobile phase is saturated with a buffer (usually water) which binds strongly to the stationary phase. This buffer will act as a liquid stationary phase and analytes with a lower solubility in the mobile phase (and a higher solubility in the buffer) are retained in the buffer, closer to the application site than those with a higher solubility in the mobile phase [11]. In this way, planar separations in which partition mode is the primary mechanism are a form of liquid-liquid chromatography [1]. The separation is typically controlled by altering the mobile phase composition, though there is a limited effect of the stationary phase material (typically cellulose or diatomaceous earth) on the resulting separation. Partition mode TLC is particularly useful for separation of hydrophilic inorganic and polar organic compounds.

Ion-exchange is another separation mode of TLC in which there is electrostatic forces occurring between the polar parts of the analytes and the ionic centres of the sorbent surface. Ion-exchange mode TLC is primarily performed using polyethyleneimine (PEI) modified cellulose stationary phases, and is useful in the separation of compounds such as amino acids [2].

Another noteworthy mode of TLC separation is known as Reversed Phase TLC (RP-TLC), in which a non-polar stationary phase is coupled with a polar mobile phase such as water. The most commonly available RP-TLC stationary phase is silica gel functionalised with covalently-bonded hydrocarbon chains. RP-TLC is suited towards the separation of highly similar hydrophobic analytes.

Table 2.1: Some common TLC stationary phase materials with typical applications [1,2].

Sorbent	**Compounds separated**
Silica gel	All classes of compounds.
Aluminium oxide	Basic compounds (alkaloids, amines, etc.), steroids, terpenes, aromatic and aliphatic hydrocarbons.
Magnesium silicate	Steroids, pesticides, lipids and alkaloids
Cellulose	Amino-acids and derivatives, food dyes (acidic and basic), carbohydrates.
Diatomaceous earth	Carbohydrates, aflatoxins, herbicides, tetracyclines.
Amino-bonded silica gel	Particularly good for carbohydrates, sulfonic acids, phenols, carboxylic acids, nucleotides, nucleosides.
Cyano-bonded silica gel	Many classes of compounds, particularly good for pesticides, steroids, preservatives.
Diol-bonded silica gel	Many classes of compounds, particularly good for steroids, hormones.
Chiral-modified silica gel	Enantiomers of amino-acids, N-alkyl and a-methyl amino-acids, simple peptides, a-hydroxycarboxylic acids (catecholamines).

2.1.2 Sample Application

TLC analysis is typically performed using sample volumes on the order of a single microliter. Application can be performed using a standard laboratory or glass microcapillary pipette with the sample directly applied to the plate, which allows for the application of volumes as small as 100 nL. For higher throughput, sample application can be automated sample application [12]. This automatic application is achieved via a Plate Spotter, which can automatically dispense a known volume of sample on the desired area (or areas) of a plate.

Care must also be taken when applying the sample to not overload the TLC plate with volumes large enough to block the pores of the stationary phase which will

negatively affect the resultant separation. One potential route to avoid overloading is to apply the sample as a band, rather than a single spot. While this can be difficult manually, automated sample spotters have the capability for both band and spot application.

The initial spot size has a large effect on both the spot capacity of the plate and the final spot size of the developed analyte. The initial spot diameter d, assuming no evaporation during drying, is given by:

$$d = \left[\frac{V}{\pi \times \ell \times \varepsilon_i(1-\varepsilon_e)}\right]^{\frac{1}{2}} \qquad \textbf{Eqn. 2.1.1}$$

where V is the applied spot volume, ℓ is the layer thickness of the TLC plate and ε_i and ε_e are the inter-and intra-particle porosity respectively [2].

2.1.3 Mobile Phase and Plate Development

After sample application, the plate is developed using a solvent or "mobile phase". The development is performed by placing the TLC plate in a reservoir of the mobile phase. The mobile phase is then drawn through the stationary phase layer by capillary action. Typically, the TLC plate is developed in a sealed container known as a "development chamber". These can be single-bottomed, where there is only a single reservoir for the mobile phase, or twin-bottomed in which there are two separate reservoirs [12].

Prior to separation, the reservoir is filled with a solvent which is allowed to evaporate, changing the composition of the vapour phase inside the chamber. This technique is known as preconditioning. The chamber alone, or both the chamber and plate can be preconditioned depending on the separation. If a twin-bottomed development chamber is used, the chamber can be preconditioned with a composition different to that of the mobile phase if this is required. Preconditioning is typically performed for between 5 and 30 minutes, depending on the solvents used and their volatility.

One measure of the separation is the degree of analyte retention known as the Retardation Factor, R_f, also known as the Retention Factor. The initial spot position on the TLC plate is defined as $R_f = 0$, and the final position of the solvent front defined as $R_f = 1$ (shown in Figure 2.2). The retention factor of an analyte is thus a ratio of the

distance travelled by the analyte, Z_x, to the distance travelled by the mobile phase, Z_f, such that:

$$R_f = \frac{Z_x}{Z_f} \qquad \textbf{Eqn. 2.1.2}$$

This value of R_f is characteristic of each analyte within the sample under the specific chromatographic conditions applied, and allows for unknown analytes to be compared with known standards. The value of R_f will depend on the stationary and mobile phases, and can vary from plate to plate and thus analyte comparison must typically be performed on the same plate. Though it is of limited use to compare retention factors between two discrete separations for different mobile and stationary phase conditions, comparison can yield information on how analytes behave in contact with different functional groups.

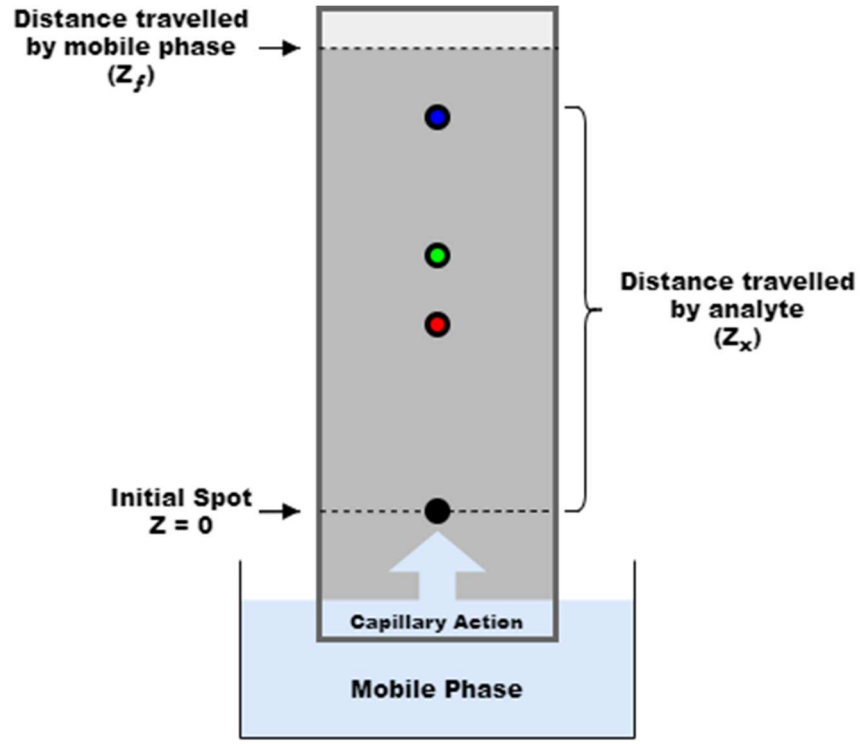

Figure 2.2: Schematic showing the analyte retention post-separation. The distance travelled by the mobile phase, Z_f, is defined as an $R_f = 1$, while initial sample (black spot) position is defined as $R_f = 0$. The distance travelled by the individual analytes (red, green and blue spots), Z_x, are then used to determine the Retention Factor for each analyte.

As the plate develops, the individual analytes will spread out over the length of the plate, hence for a separation over a given length, there are a finite number of analytes the can be successfully resolved. This property of the TLC plate is known as the "spot capacity" or "separation number" (SN) which is given by the equation:

$$SN = \left[0.425\sqrt{N} \times \left(\frac{b_1 - b_0}{b_1 + b_0}\right)\right] - 1 \qquad \textbf{Eqn. 2.1.3}$$

where N is the "number of theoretical plates" (a quantification of the effectiveness of medium for a given separation) for a substance with an $R_f = 1$, and b_1 and b_0 are the

width of the spot at a R_f of 1 and 0 respectively, which can be determined experimentally [2]. Equation 2.1.3 can be further simplified using the expression[1] [2]:

$$N = \left(\frac{Z_f}{b_1 - b_0}\right)^2 \times 5.54 \qquad \textbf{Eqn. 2.1.4}$$

which yields the expression:

$$SN = \frac{Z_f}{b_0 + b_1} - 1 \qquad \textbf{Eqn. 2.1.5}$$

Logically, this leads to the result that a smaller initial spot size will result in a higher spot capacity, however, it is seen in practice that as diffusion occurs over the separation, area spot diameters converge on a similar value as long as the plate is not overloaded [12]. From Equation 2.1.4 it is possible to then determine the number of theoretical plates (N):

$$N = 5.54\left[\frac{Z_x}{b_x - b_0}\right]^2 \qquad \textbf{Eqn. 2.1.6}$$

where b_x is the spot diameter of the separated analyte. Once N is known, this can be used to get the plate height (H) through the expression:

$$H = \frac{Z_x}{N} \qquad \textbf{Eqn. 2.1.7}$$

or more generally:

$$H = \frac{(b_x - b_0)^2}{5.54 Z_x} \qquad \textbf{Eqn. 2.1.8}$$

[1] Equation 2.1.4, and the 5.54 coefficient therein, is defined in World Health Organisation International Pharmacopeia, 4th Edition, Volume 2 Methods of Analysis, Section 1.14.4 (and various national and supranational pharmacopeia) as the standard for measuring the efficiency of a chromatographic media.

The value for b_0 is extrapolated from an assumed linear proportionality of the spot width b_x for each analyte in the sample as a function of migration distance. As the analytes closer towards a position of Z_f are assumed to have a larger spot diameter than the initial spot at position Z_0, this allows an extrapolation of the initial spot diameter b_0. It should be noted that this extrapolated value for b_0 will typically exceed that of the measured spot size prior to development, due in part to the initial reshaping of the spot when the mobile phase first comes in contact with the spot.

In terms of development of TLC plates, it is typically performed in a single step, with the mobile and stationary phases chosen to result in an optimum separation. For similar compounds, or samples with a large number of analytes, the separation can be done in multiple stages. One technique to improve separations is multiple development whereby the plate is developed, dried and the development is repeated.

Another technique for separating highly similar compounds is to develop the TLC plate normally, dry the plate, and repeat the development at 90° with respect to the original development. This technique is known as two-dimensional TLC (2D-TLC) and can be successful when the sample has more analytes than the plate capacity. The second development also allows for different mobile phase compositions to be used for each dimension. Typical spot capacities for platforms used in 1D separations are upwards of 30, while the same platforms used for 2D separations can have spot capacities that exceed 250 [12]. This technique can also be coupled with multiple development for further increased sensitivity.

2.1.4 Post-Separation Analysis

There are a number of methods for post-separation analysis including densitometry, UV-Vis-NIR absorption and fluorescence spectroscopies [13] and mass spectrometry [14] which are presented in detail below.

Densitometry

Densitometry is perhaps the most common post-separation detection technique, due in part to its simplicity. In this technique, a developed TLC plate is subject to illumination via transmitted or remitted (scattered or reflected) white light, or UV illumination (typically 366 nm or 254 nm). Under this illumination, the plate is imaged using a CCD camera, and an image of the plate recorded. In the case of UV illumination, this allows for imaging of fluorescent analytes which may be optically

transparent under white light. Analysis is typically done by measuring the greyscale intensity along the length of the plate, allowing for accurate position of each analyte along the plate to be determined.

If the compounds are not visualisable, either optically or via UV illumination, post-separation visualisation may be performed using a number of alternative methods. One method for visualisation of optically inactive compounds is the addition of a fluorescent indicator to the stationary phase. Indicators such as fluorescent indicator green (F_{254}, Zn_2SiO_4) are added to the stationary phase during plate coating, in this case allowing visualisation via illumination at 254 nm. When an analyte is present, this fluorescence is quenched, thus showing up as a dark area under 254 nm illumination. It should be noted that any additive to the stationary phase can participate in the separation, and thus the presence of an indicator may negatively affect the separation capabilities of the plate.

Another method for post-separation visualisation is through derivatisation whereby the compound to be visualised is exposed to a volatile gas, typically iodine vapour in the case of TLC derivatisation. Upon exposure, the compounds will become brownish in colour, due to the iodine binding to the compounds and thus are able to be densitometrically observed.

UV-Vis-NIR Absorption and Fluorescence Spectroscopy

Another common method for TLC quantification is via UV-Vis or fluorescence spectroscopy. These techniques can be performed in either transmittance or reflectance mode with the spectral response of the analytes differing between both. It is distinguished from densitometry through the use of a monochromator, allowing for wavelength-dependent absorption or fluorescence information to be collected. This additional information can be useful in fingerprinting the separated analytes.

For transmission or absorption measurements, the Beer-Lambert law is applied which states that the transmitted light intensity $I(\lambda)$ at a wavelength (λ) is:

$$I(\lambda) = I_0(\lambda)e^{\epsilon c l} \qquad \textbf{Eqn. 2.1.9}$$

where $I_0(\lambda)$ is the incident light intensity, ϵ is the molar absorption coefficient ($mol^{-1} \cdot mm^{-1}$), c the concentration of the sample (mol) and l the pathlength through the

sample (mm). By examining the ratio of the incident light intensity to the transmitted intensity it is possible to obtain a value for the absorbance (A) of the sample, where:

$$A = \ln\left(\frac{I(\lambda)}{I_0(\lambda)}\right) = \epsilon c \ell \qquad \textbf{Eqn. 2.1.10}$$

Similarly, for reflectance spectroscopy, the relative change in reflectance of the sorbent layer with and without the presence of an analyte is compared. This change, the wavelength-dependant reflectance $R_\infty(\lambda)$, (assumed to caused by absorption on an infinitely thick layer) is defined as the ratio of the reflectance intensity such that:

$$R_\infty(\lambda) = \ln\left(\frac{I(\lambda)}{I_0(\lambda)}\right) \qquad \textbf{Eqn. 2.1.11}$$

where $I(\lambda)$ and $I_0(\lambda)$ are the wavelength-dependant intensity distribution of the analyte zone and a clean zone respectively [15]. An equation developed by Kubelka and Munk allows for this principle to be extended to TLC analysis [12]. Their proposed model reduces the complexity by assuming that the scattering occurs isotopically and homogenously on the surface of the TLC plate, with no absorption or reflection from the sorbent layer, such that:

$$\frac{(1-R_\infty)^2}{2R_\infty} = \frac{a}{s} = 2.3\frac{\varepsilon}{s}c = 2.3\frac{\varepsilon}{s}\frac{n}{dA} \qquad \textbf{Eqn. 2.1.12}$$

where a is the absorptivity, ε is the molar absportion coefficient, s is the scattering coeffient, c is the TLC spot concentration, n is the analyte amount, d is the TLC plate layer thickness and A is the spot area.

Infrared Spectroscopy

Infrared spectroscopy allows for the analysis of the chemical structure of materials via probing their vibrational and ro-vibrational bonds. Three main IR spectroscopic techniques are applicable to TLC: Diffuse Reflectance Fourier-Transfer Infrared

Spectroscopy (DRIFT), Attenuated-Total Reflectance Fourier-Transfer Infrared Spectroscopy (ATR-FTIR) and Raman Spectroscopy.

DRIFT utilises an infrared beam which is scanned over the surface of the TLC plate, collecting the wavenumber-dependent intensity as a function of position over the TLC plate. In ATR-FTIR, an area of interest is placed in contact with the spectrometer aperture, and the total measured IR reflectance analysed. Even though this required manual placement of the sample does not allow for the full plate to be scanned, its relatively simple setup allows for individual areas of interest to be analysed. As ATR-FTIR requires pressure to be applied to the sample to ensure good contact with the spectrometer aperture, it is not suited for analysis of samples on soft layers such as silica gel, however it may be suited towards the analysis of separations on more stable monolithic UTLC layers.

Mass Spectrometry

Another potential technique for post-separation detection in TLC is mass spectrometry (MS). In TLC-MS, the sample in question is removed from the TLC plate for analysis, injected into the MS where it undergoes ionisation. After ionisation, the resulting molecule fragments are separated by their mass-to-charge ratio (m/z) allowing for detailed analysis of the sample in question.

The analytes are removed from the TLC plate using a TLC-MS elution head, through the successive injection of solvent and elution of the sample. By injecting solvent around the dried analyte spot on the plate, it is possible to suspend the analytes in the solvent, and then a collection port can be used to remove the liquid analyte/solvent mix before injection into the MS. This liquid sample can then be aerosolised via electrospray ionisation (ESI) whereby the application of a high voltage to a liquid results in both aerosolisation and ionisation.

An alternative ionisation technique is matrix-assisted laser-desorption ionisation (MALDI). A slightly more complicated technique than ESI, MALDI is first performed by mixing the liquid sample with a crystalline matrix material. This sample-matrix mix is then dried on a metal plate, after which a high-pulse power laser is used to ablate the sample. After ablation, ionisation occurs, and this ionised plume, which is in either the plasma or gas phase, is then injected into the MS. As this matrix material is simply used primarily to solidify a liquid sample for laser-induced desorption, it has

been demonstrated that it is possible to directly perform MALDI on TLC plates with sub-micrometre silica particles [16].

The degree of molecular fragmentation can be controlled via variation of the ion energy, itself related to the voltage applied (in the case of ESI) or the laser fluence used to ablate the sample (in the case of MALDI). Higher energy collisions can break apart larger compounds, in a process referred to as "fragmentation" or "cracking", thus allowing additional information to be gained. Both ESI and MALDI are typically referred to as a "soft" ionisation techniques whereby large molecules and compounds can be ionised with little cracking. After ionisation, the resulting ionised mass fragments are separated based on their m/z ratio using electric or magnetic fields and detected at the ion collector.

2.1.5 High Performance Thin Layer Chromatography

The next major advancement in TLC came in the form of "High-Performance Thin Layer Chromatography" (HP-TLC). It was demonstrated in 1973 that by reducing the average particle size of sorbent silica gel layers (down to the order of single microns), separation sensitivities could be improved by an order of magnitude, while reducing analysis time [17]. These new sorbent layers also required less mobile phase and had shorter development distances thus allowing plate sizes to be reduced.

The only sorbent currently utilized for HP-TLC is silica gel, typically prepared via a sol-gel process. The use of silica sol-gel is due in part to the ability for both pore and particle size to be controlled in a highly reproducible manner resulting in high separation repeatability. Layer thicknesses in HP-TLC are on the order of 100 – 200 µm which is comparable with TLC. However, as the average particle size is reduced, it allows smaller sample volumes to be used. In general, for the same separations, HP-TLC has higher efficiency than TLC, while also having shorter sample migration distance of 3 – 6 cm and reduced separation times of 3 – 20 minutes.

Various groups reported hydrophobic, or "reversed-phase", HP-TLC plates which are now commercially available. Similarly, developed at the same time were amino-, cyano- and diol-bonded silica gel stationary phases which were again subsequently commercially available [2,18]. The functionality of these plates further extends the capabilities of TLC and HP-TLC for specific applications.

Amino-bonded TLC plates, functionalised with aminopropyl groups, have some hydrophobic properties, and as such behave as normal- or reversed-phase depending

on the solvent choice [2]. Cyano-bonded plates, which are functionalised with cyanopropyl groups via a siloxane bond, have intermediate properties and as such fill a gap between RP and normal phase TLC [2]. This dual nature allows for 2D-TLC to be performed in both normal or reversed phase, or a combination of both phases. Plates functionalised with diol alkyl ether groups, known as diol-bonded TLC plates, have similar properties to cyano-bonded plates, though are more suited towards normal phase separations [2]. Both cyano- and diol-bonded plates are useful for the separation of compounds such as steroids and hormones, while amino-bonded plates are suited towards the separation of nucleotides, nucleosides and sulfonic and carboxylic acids.

With advances in computing and spectroscopy occurring rapidly at the time, fully automated optical spectroscopy and densiometric scanning of TLC plates became common, further enhancing accuracy and limits of detection for quantitative TLC [19]. For densiometric detection, the exposure to reagents such as iodine vapour or ammonia vapour is utilized which allows for the visualization of various optically transparent compounds.

Recently, work has been progressing on chiral-based TLC separations using both chiral-selective mobile phase additives and stationary phases [20]. There is significant interest in this area within the pharmaceutical sector, where chiral selective analysis is needed for quality assurance, which to date has typically performed using liquid chromatographic techniques [21].

2.1.6 Ultra-thin Layer Chromatography

As HP-TLC developed, the advantage of small particle size for enhanced separation was widely recognized. Advances in sol-gel methods allowed for particle sizes and layer heights of monolithic porous silica films to be reduced even further, resulting in separations of high sensitivity [22]. With the sorbent layer height being reduced to an order of magnitude lower compared to HP-TLC, this new technique was named "Ultra-Thin Layer Chromatography" (UTLC) following on from the nomenclature developed for liquid chromatography.

UTLC is an emerging form of thin layer chromatography distinguished by the use of thin or monolithic stationary phase layers on the order of 10 µm, compared with 100 – 200 µm layer thickness for HP-TLC [23]. Typically, chemical bonding is employed for a stationary phase layer to adhere to a glass or polymeric substrate. The use of monolithic (i.e. single-piece) layers also removes the need for the addition of

binder material to the stationary phase since monolithic layers are chemically bound to the substrate by covalent bonding. This use of bound monolithic sorbent layers results in two main advantages: firstly, it allows a reduction in layer thickness by reducing the volume of material within the sorbent layer; secondly, as the analytes within a sample will have an affinity for binder material, its removal by the use of the monolithic sorbent results in increased separation efficiency. The decrease in stationary layer thickness also results in reduced migration distances, and faster separations along with low mobile phase solvent consumption [9,22]. There is also increased sensitivity leading to lower limits of detection when compared with TLC and HP-TLC, as outlined in Table 2.2.

The reduction in the size of the sorbent layer also presents some challenges. The reduced layer height results in lower capacity for both sample and mobile phase with application of samples on the order of nanolitres required. Furthermore, detection (especially colorimetric) can be difficult due to small sample volume. To mitigate this, the use of UV-Vis and fluorescence spectroscopies and mass spectrometry, as opposed to the typical densitometric detection, has become common practice for post-separation analysis in UTLC.

Table 2.2: Comparison of silica coatings used in various planar chromatographic techniques [24,25].

Parameter	TLC	HP-TLC	UTLC
Plate size (cm)	20 × 20	10 × 10	6 × 3.6
Layer thickness (µm)	100 – 250	100 – 200	10
Particle Size (µm)	10 – 12	4 – 6	Monolithic
Particle size range (µm)	5 – 20	4 – 8	
Maximum value for Z_f (cm)	7 – 15	3 – 7	1 – 3
Separation time (min)	30 – 200	3 – 20	1 – 5
Average plate height (µm)	35 – 75	23 – 25	< 10
Typical spot application volume (µL)	1 – 5	0.1 – 0.5	0.01 – 0.1
Maximum initial spot diameter (mm)	3 – 6	1 – 1.5	0.5 – 0.1
Detection limits (reflectance)			
UV-vis (ng)	1 – 5	0.1 – 0.5	0.5
Fluorescence (pg)	50 – 100	5 – 10	5

2.2 Current Fabrication Techniques for UTLC Platforms

There are a number of possible methods for fabrication of UTLC plates. As a rule, these methods must achieve small layer thicknesses without the need for a binding agent to adhere the stationary phase to the substrate.

2.2.1 Polymer Electrospinning

Electrospinning is a method of thin film deposition whereby a high electric field is placed between a polymer solution (fed from a nozzle or syringe connected to a pump) and a conductive collector plate, as shown in Figure 2.3. An electric field is applied causing the formation of a “Taylor cone” on the nozzle. This Taylor cone is formed

by the solution distorting from the shape formed via surface tension at the aperture of the nozzle as a result of the applied electromagnetic field. When the surface tension of the polymer solution is overcome, the polymer solution is pulled from the nozzle towards the plate [26]. This technique has been successfully used to create carbon- and polymer-based nanofiber-coated stationary phases on aluminium foil substrates [27–29].

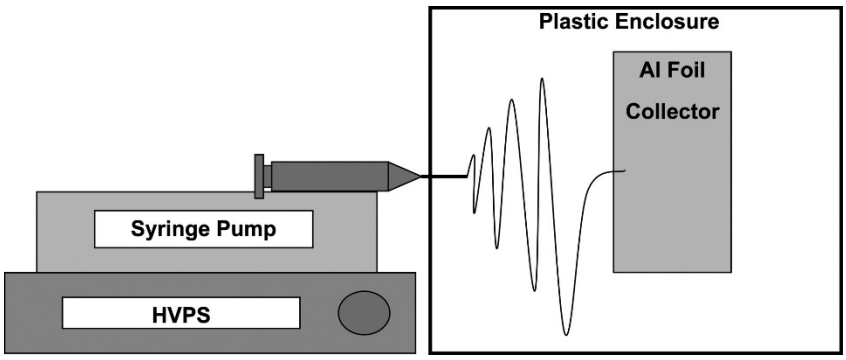

Figure 2.3: Experimental setup for fabrication of UTLC plates using electro-spinning. A polymer solution is placed in a syringe and pumped in the presence of a strong electric field (between nozzle and collector) provided by a high voltage power supply (HVPS), and the solution is then incident on an aluminium foil substrate [27].

One example utilized a 10% polyacrylonitrile (PAN) solution in dimethylformamide (DMF) [30]. The polymer solution was stirred for 24 hours to ensure that the solution was homogeneous prior to use. The optimized experimental parameters were as follows: a solution pump rate of 0.025 ml/min, a tip-to-collector distance of 10 cm, an applied electric field of 10 kV, and relative humidity of 50%. The solution was extruded onto an aluminium foil substrate placed above a stainless-steel collector plate. The resultant UTLC plate is shown in Figure 2.4. When examined using SEM, the electrospun fibres have been seen to have macroscopic lengths (on the order of 1 – 100 cm) but nanoscopic diameters of approximately 400 nm.

After coating, the substrates were cut into 3 × 6 cm plates from portions of the foil found to have uniform deposition thickness. The plates exhibited good mechanical strength and the coating was seen to be bonded well to the substrate, thus eliminating the need for a binding agent to be used [24].

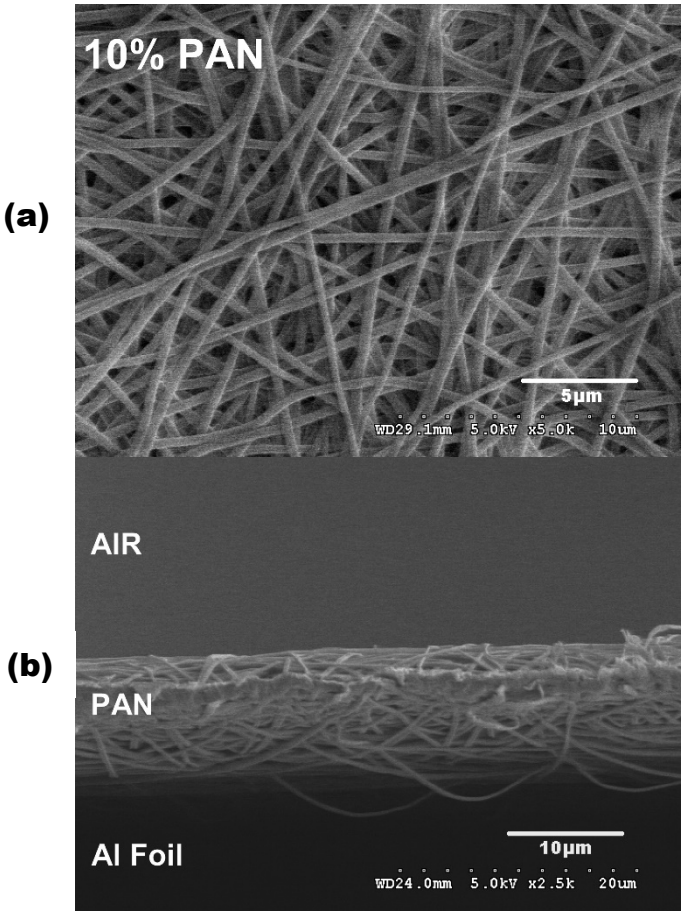

Figure 2.4: (a) Top-down and (b) cross-sectional SEM images of an electrospun PAN-based UTLC plate fabricated on an aluminium substrate [27].

Supplementary techniques employed in conjunction with electrospun nanofibers included pyrolysis and the use of photoresistive polymers allowing further texturing of the stationary phase [30] thus increasing the surface area available for interaction with the analyte. A method for producing aligned electrospun fibres has also been documented, which when applied to separations led to shorter detection times and improved reproducibility when compared to non-aligned fibres [28].

Electrospun PVA fibre-based UTLC plates have been compared with commercial silica HP-TLC plates (produced via a sol-gel process) for the separation of fluorescently-tagged (in this case fluorescein isothiocyanate-tagged) amino acids [27]. The polarity exhibited by PVA fibres due to the presence of hydroxyl groups proved an issue, with an intermediate step for decreasing the water-solubility of PVA required prior to use [31]. This was done via crosslinking of the polymer chains during electrospinning using glutaraldehyde (GA) with hydrochloric acid as a catalyst or via a post-spinning treatment with GA combined with an acetone surface treatment. The

crosslinking during electrospinning produced better results, with little change in the morphology when compared to post-treated plates which showed signs of partial dissolution. These PVA-based UTLC plates also showed higher efficiencies than commercial silica sol-gel based HP-TLC plates.

2.2.2 Microstereolithography

Recently additive manufacturing (AM), also referred to as 3D printing (3DP), via microstereolithography (μSL) has been applied for the direct fabrication of planar chromatography platforms [32]. μSL utilizes a curable photopolymer resin which is jetted in layers onto a surface and cured using a UV photodiode. As each layer is cured, a subsequent layer is printed onto the surface and again cured in place, allowing the technique to build up a 3-dimensional solid part. If any internal voids or surface features are required, a support material is printed and partially cured in place. This support material can be removed after production via a wash in organic solvents, or weak solutions of bases such as sodium hydroxide depending on the support material composition.

Work by MacDonald et al. utilising a Stratasys PolyJet3D, demonstrated the direct fabrication of a planar chromatography plate and high-surface area functional microchannels on the plate surface in a single build [32]. These microchannels were fabricated using an acrylate-based photopolymer (Veroclear RGD810 with SUP707 support material) with channel depths of between 100 – 200 μm, separated by an interchannel distance of 20 μm (Figure 2.5). The plates with larger depths showed better mechanical properties resulting from the appearance of crosslinking structures between channel walls, with less cracking occurring as the plate cured. The larger depth plates also demonstrated enhanced linear homogeneity, allowing for uniform channel flow profiles on each plate.

The 3D printed plates showed favourable separation capabilities when compared to traditional cellulose TLC plates when applied to the separation of organic dyes and fluorescently-tagged proteins. Some “streaking” of the eluents was seen on the 3D printed plates, however in all cases the individual analytes were successfully resolved on the plates.

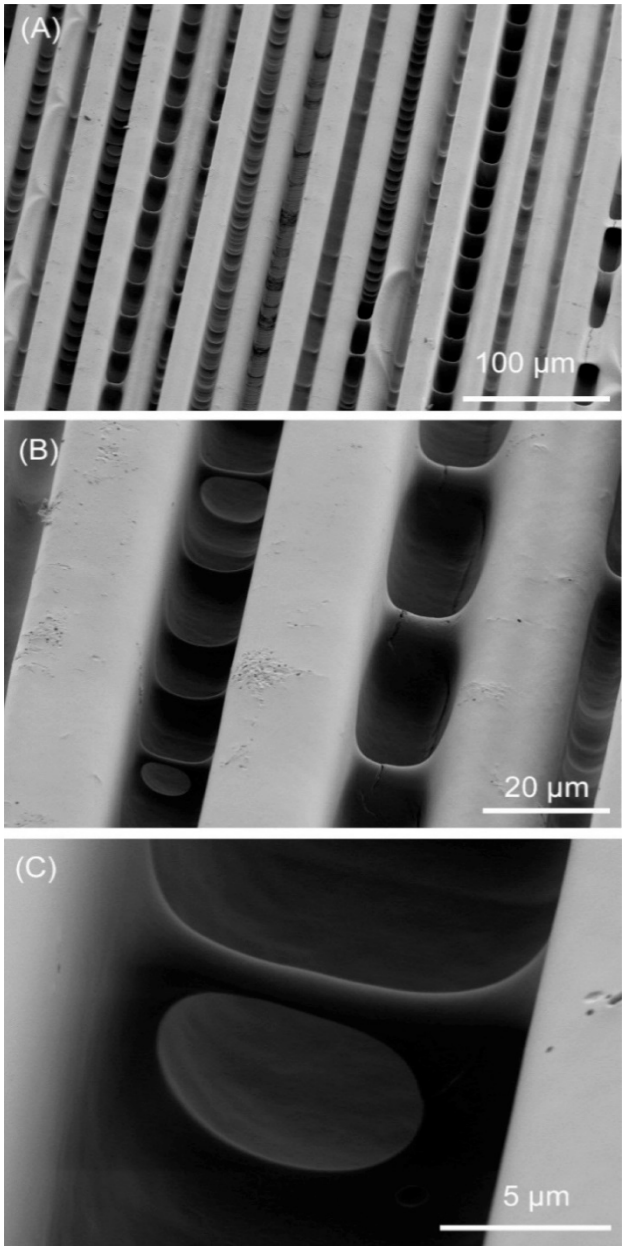

Figure 2.5: SEM images of 3D-printed TLC plates with scale bars of (a) 100 µm, (b) 20 µm and (c) 5 µm [32].

2.2.3 Polymer Monolith Deposition

Polymer-based monolithic stationary phases have been extensively used in capillary and microchip-based LC [33,34]. Recently, a method for the production of porous polymer monolithic layers on glass substrates for ultra-thin layer chromatography was reported [35]. This method utilized a poly(butyl methacrylate-co-ethylene dimethacrylate) monolithic film which was then photografted with functional groups. The monomer solution was first deaerated, applied to the surface of a glass substrate, and subsequently irradiated using 264 nm UV source. After curing, the polymer

monolith was washed with methanol and vacuum dried. The resultant coatings were monolithic in nature and between 50 – 200 µm in thickness. These plates were then applied in the separation of peptides and proteins using both UV spectroscopy and Matrix-Assisted Laser-Desorption Ionization Time-of-Flight Mass Spectrometry (MALDI-TOF-MS) as the detection techniques.

2.2.4 Silica Monolith Deposition

The sol-gel process, which is widely used in the creation of silica monoliths for separation applications such as high-performance liquid chromatography, uses sequential hydrolysis and polycondensation of a liquid alkoxysiloxane on a non-reactive substrate (typically a glass plate, inert polymer or aluminium sheet) resulting in a highly pure, monolithic (i.e. single piece) meso- and macroporous structure forming on the substrate [22,36–38]. The resultant film being monolithic in nature required no binder [9,39]. In one example a stationary layer formed was approximately 10 µm thick, with mesopores of 3 – 4 nm optimizing retention, and macropores of 1 – 2 µm which minimized flow resistance [25].

Silica-based UTLC plates fabricated using a silica sol-gel process were applied to the separation of amino acids, pharmaceutically active ingredients, phenols, and plasticizers with all the separations showing increased efficiency with respect to sensitivity, speed and solvent consumption [9,22].

Another recent development towards depositing silica gel layers for planar separation has come about using additive manufacturing. By modifying a commercial fused deposition modelling 3D-printer (Prusa i3) to extrude a silica slurry, it was possible to 3D-print a porous silica layer suitable for planar chromatography [40]. The printed layers had a thickness of 200 µm, and the printer was capable of printing over areas of 10 cm × 10 cm in 5 minutes. This opens new routes towards the fabrication of planar chromatography platforms with tailored thickness, porosity and, through the possibility of printing different materials, tailored stationary phases or phase-combinations.

2.2.5 Glancing Angle Deposition

Another process successful in the creation of UTLC plates is a modified form of Atomic Layer Deposition (ALD) known as Glancing-Angle Deposition (GLAD) [41–45]. The GLAD process uses an electron-beam to evaporate a target of known

composition which is then incident on a substrate (Figure 2.6). By altering the angle of the vapor flux (Θ) it is possible to control the porosity and density of the deposited film, while manipulation of the azimuthal angle (φ) via stepper motors alters the geometry for the deposited nanowire [44].

Figure 2.7 shows SEM images of SiO_2 nanowires created using GLAD. Deposition was conducted under ultra-high vacuum ($P < 6 \times 10^{-7}$ Torr), using a 99.99% pure SiO_2 target and a glass substrate [42]. The resulting structures had nanowire morphology, and through adjusting the deposition angle, it was possible to produce zig-zag shaped nanowires (Figure 2.7b). Also demonstrated was the ability to serially deposit material resulting in grouped nanowire structures, shown in Figure 2.7c.

Other nanomaterials deposited using GLAD include TiO_2 and ZrO_2, with layer thicknesses of 2.6 µm achieved, while deposited Al_2O_3 reached a thickness of 1.3 µm [44]. Deposition rates strongly depended on the target material used, with rates of up to 0.5 nm/s for ZrO_2 at a beam current of 460 – 500 mA and 1.3 nm/s for SiO_2 at a beam current of 180 mA [44] resulting in deposition times taking up to 90 minutes.

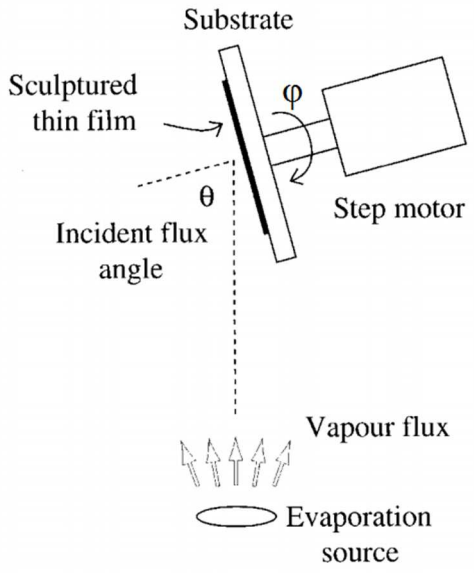

Figure 2.6: Schematic of the GLAD deposition setup [41].

Polarity-adjustable GLAD UTLC plates have also been demonstrated through silanization of the nanowires, coupled with oxygen plasma treatment for tailored hydrophobicity [46]. Further morphological modification through the use of reactive-ion etching and annealing of GLAD films has also been demonstrated for tailoring of

elution behaviours via alteration of the porosity of the sorbent layer [43]. Furthermore, it has been possible to create anisotropic nanostructures using GLAD allowing for two-dimensional separations [47].

UTLC plates fabricated via GLAD have been applied to the separation of various organic dye mixtures [43–46]. Also demonstrated was the use of GLAD fabricated UTLC plates coupled with both desorption electrospray ionization mass spectrometry (DESI-MS) [48] and matrix-assisted laser desorption mass spectrometry (MALDI-MS) [49] allowing for small molecule analysis and increased sensitivity. In-situ optical imaging during development has also been used with GLAD UTLC plates, allowing for insight into the physical and chemical processes occurring during separation on GLAD fabricated UTLC plates [50].

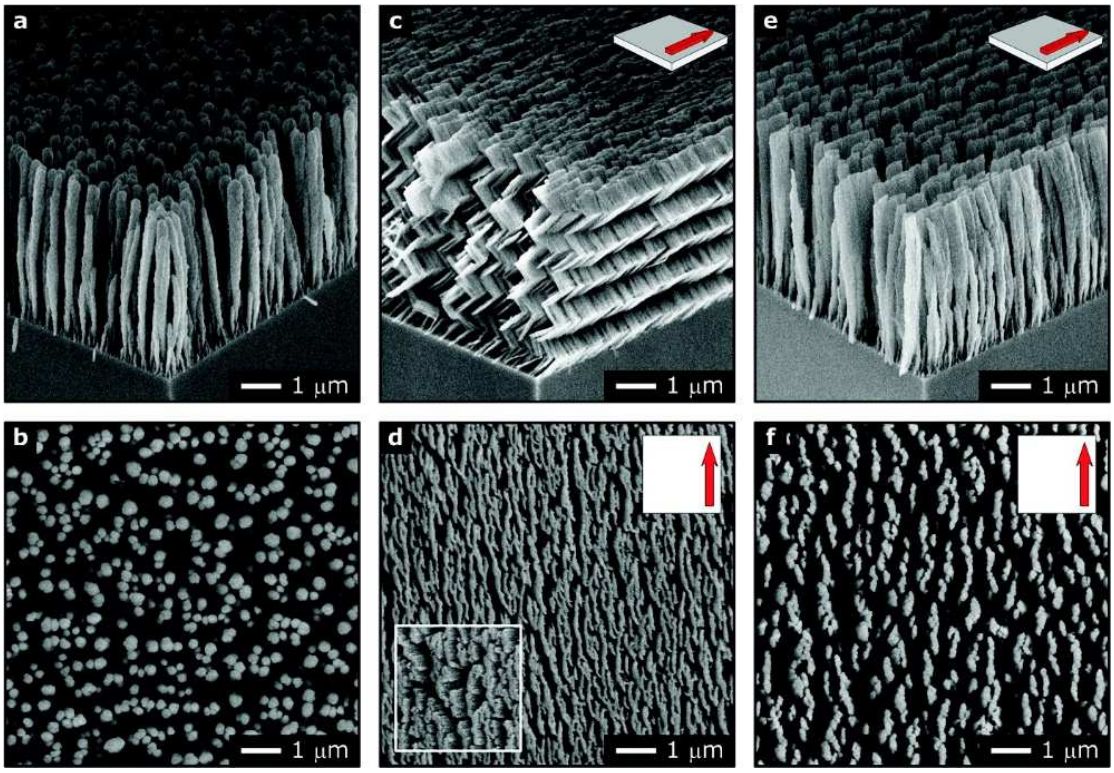

Figure 2.7: SEM images of (a and b) isotropic, (c and d) anisotropic and grouped (e and f) mesoporous Al_2O_3 structures created using GLAD. The isotropy of the deposited film can be controlled via altering the angle of the deposition flux with respect to the substrate [42].

2.2.6 Chemical Vapour Deposition

Chemical Vapour Deposition (CVD) is a deposition technique whereby a substrate is placed in contact with a reactive precursor gas, typically under vacuum conditions. When the reactant comes in contact with the substrate, deposition occurs via chemical reaction with the substrate or thermal decomposing of the gas, resulting in material deposition on the substrate. CVD is widely used in the semiconductor industry for the creation of nano- and microscale features, however it has recently been exploited to produce silicon-carbon core-shell nanotubes (SiCNTs) substrates which have been applied to planar separations [51]. Firstly, an ethylene-hydrogen low-pressure chemical vapour deposition (LP-CVD) was performed on a silicon substrate. The substrate was patterned via photolithography along with the deposition of a dual catalyst stack consisting of first 30 nm layer of alumina (Al_2O_3) followed by a 3 nm layer of iron. The resulting LP-CVD resulted in the formation of a vertically aligned carbon nanotube (CNT) forest. Subsequently, a silane LP-CVD was performed to

deposit an amorphous silicon film on the CNT forest. The substrate was annealed at 700 °C for 12 – 14 hours resulting in the formation of SiCNTs.

SiCNT UTLC plates have been applied for separation of analgesic compounds [52] and organic dyes [51,53,54]. It was seen that the catalyst layer thickness (t) greatly affected both the growth of the SiCNTs and the subsequence separation capability [52]. The surface area of the SiCNT layer when grown using an iron catalyst of thickness t_{Fe} was as seen to scale as $1/t_{Fe}^2$. An iron layer thickness of between 4 – 6 nm was seen to be ideal, with separation of analgesic compounds (caffeine, phenacetine and propyphenazone) examined as test separations. Furthermore, these SiCNT-based plates have been demonstrated as suitable platforms for coupling with Desorption Electrospray Ionization (DESI) and Direct Analysis in Real Time (DART) mass spectroscopy techniques [54]. The fabrication of SiCNT-based planar chromatography platforms have also been demonstrated with ALD [55] with a simplified fabrication procedure when compared to CVD.

2.3 Laser Microfabrication

Laser processing has been demonstrated for microdrilling of glass [56] and polymers [57–59] along with laser-induced modification of the surface chemistry [60], which also has been recently employed in surface modification of metals [61]. To date, no study has examined the possibility for fabrication of TLC plates using laser techniques. However, various types of laser processing of polymers have been shown to be capable of creating features on the same order as those required for the manufacturing of UTLC plates.

2.3.1 Laser Direct-write Processing

Laser direct-write (LDW) processing refers to the patterning or modification of a material by direct laser irradiation. When material removal is the primary aim (as opposed to surface chemical modification) it is more specifically referred to as “Laser Direct-Write Subtractive, or “LDW−“. The laser-material interaction during LDW− can range from physical effects (typically photothermal in nature) to chemical changes (e.g. photochemical ablation or laser irradiation of photoresistive materials). Laser direct-writing allows rapid, scalable and cost-effective processing. The term direct-write can be used to describe processing done using either continuous wave or pulsed laser irradiation, though the term pulsed laser ablation (PLA) more specifically refers

to the latter. PLA can also specifically refer to high-power pulsed laser irradiation where the primary mechanism of material removal is sublimation along with thermal and electronic sputtering.

LDW– has been applied to various polymer materials using different laser wavelengths and powers for the creation of micron-scale features. For example, it was possible to both cut and create microtrenches of 8 – 12 µm width and 2 – 4 µm depth in poly-caprolactone (PCL) with minimal damage to the heat affected zone using a third-harmonic Nd:YAG laser at 355 nm [62].

LDW– processing of PMMA using a CO_2 laser allowed for the production of various channel widths in the range of 140 – 900 µm [63]. The depth of the channels formed was proven to scale with laser power, while post-process surface smoothing was performed using a single thermal anneal cycle. However, one drawback of this method is the lack of repeatability in the surfaces produced, especially where smooth surfaces are needed. Chemical modification of the resulting substrates was performed using organosilane chemistry for attachment of functional perfluoroalkyl, amino and sulfhydryl groups for surface passivation and immobilisation of bio-recognition molecules.

A CO_2 laser was also used to create microchannels on a cyclic olefin copolymer (COC) substrate by direct-write laser processing. Although the resultant channels were of lesser quality than those which were created using a micromilling machine, laser-direct write was found highly suitable for rapid and low-cost prototyping of microfluidic devices [64]. Further work on COC substrates using an ArF excimer laser showed a lower laser penetration depth when compared to PMMA, which allowed for a finer control of the resulting surface morphology [65].

One study, which investigated LDW– using a pulsed Nd:YAG laser on PMMA submerged in water, demonstrated the capability of producing features 90 – 500 µm wide and 100 – 500 µm deep [59]. Substrate submersion led to reduced thermal damage while minimising solidification of ablated material in and around the microchannels, which can be exploited if smooth microchannels are required.

Channels of 1 µm width and 500 nm depth were also produced on porphyrin-doped PMMA substrates using a 405 nm laser with little or no ablation taking place [66,67]. The primary mechanism of channel formation was a result of changes in surface tension due to melt while the porphyrin dopant allowed for increased UV and optical absorption of the applied radiation. A finer control over the surface patterning was

possible when the same process was applied to SU-8 photoresist due to both physical and chemical effects taking place.

The above techniques rely on the direct absorption of the laser radiation. However, as many polymers are highly transparent to radiation from the UV-A band to IR-A band (280 nm – 1400 nm), LDW– can be an inefficient process with many common laser systems. One method to increase the absorbance of the material involved is the use of metallic nanoparticles dispersed in a polymer mixture as a surface coating, which improved the efficiency of texturing an optically transparent polymer using a 532 nm Nd:YVO_4 [68].

Another method currently being reported for nanostructuring of polymers via laser irradiation is Laser-Induced Periodic Surface Structuring (LIPSS). This technique exploits interference of the incident and refracted/reflected light at the target surface resulting in the formation of features on the range of hundreds of nanometres in depth, which exhibit a periodic structure [69]. LIPSS can be performed both above and below the ablation threshold of the material, and has been reported for many laser wavelengths and pulse durations [69–71].

Another technique, referred to as Laser-Induced Backside Wet Etching (LIBWE) exploits laser ablation of a target, in which the ablation side is in contact with a liquid and illumination of the target area occurs through the polymer bulk [72]. Work conducted using a nanosecond pulsed XeCl excimer laser (308 nm) found etch rates of up to 20 nm/pulse on poly(tetrafluoroethylene-co-hexafluoropropylene) (FEP) when in contact with a pyrene/tetrahydrofuran solution, with the resultant microchannels being clear of debris [73].

2.3.2 Pulsed Laser Ablation

Pulsed Laser Ablation (PLA) is an effective method of surface texturing and has been demonstrated with various polymers such as polyetheretherketone (PEEK) [74], polycarbonate (PC), poly(methyl methacrylate) (PMMA) [74–77], polyethylene chloride (PEC) [78], and polytetrafluoroethylene (PTFE) [79] and biopolymers such as collagen and gelatine [80]. To optimise these methods, the physical and chemical processes occurring during polymer ablation are still an important area of investigation.

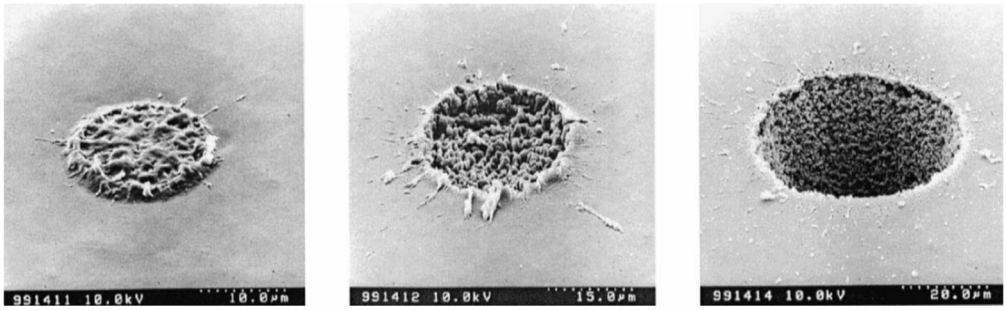

Figure 2.8: SEM images of a PMMA substrate after (a) 1, (b) 5 and (c) 10 laser shots [76].

Work conducted with a 150 fs Ti:sapphire laser (800 nm) was used to ablate the surface of PC and PMMA at a fluence of 3 J/cm^2 [76]. Surfaces post-ablation showed significant changes in their morphological profile over a range of laser shots, with surface restructuring occurring for single-shot passes on PMMA, and melt ejection for higher fluences, shown in Figure 2.8 [76]. Work conducted by Serafetinides et al. demonstrated that laser etch rates for different polymers vary with a number of laser parameters such as wavelength, fluence and pulse width [81].

Further work by Tokarev and Kaplan [82] on the suppression of melt-flows during pulsed laser ablation showed how laser ablation of polymers and ceramics (both materials with large Prandtl numbers[2]) could be explained purely by thermal mechanisms, allowing for the easy optimisation of laser polymer ablation methods. The generation of carbon nanostructures using PLA has also been demonstrated [83] and could be deployed in conjunction with the PLA of a polymer surface to provide the texture required for chemical separations [51,84]. Furthermore, PLA has been combined with transparent substrates in contact with a metallic target for the creation of nanoparticle coatings [85], allowing for the opportunity of laser-based stationary phase deposition.

Specific polymers designed for laser microstructuring based on cinnamylidene malonic acid ester groups showed the possibility for high-resolution ablation based structures, with the resultant polymer film having stability during wet-etch processes [86].

[2]The Prandtl number (Pr, unitless) is a ratio of the viscosity (ν) and the thermal diffusivity (α) of a given material such that $\mathrm{Pr} = \nu / \alpha$.

2.3.3 Extreme Ultraviolet Processing

Extreme Ultra-Violet (EUV; 10 – 124 nm) radiation has proved very successful at texturing polymer surfaces. Unlike longer wavelength radiation, EUV radiation has a low penetration depth (< 100 nm) which makes it an efficient method of texturing polymer surfaces without altering the bulk properties of the material [87]. The resulting surface morphology post-EUV treatment varies depending on the polymer used, with feature sizes ranging from the nanoscale up to tens of microns [88].

Modification of the surface morphology of polyethylene terephthalate (PET), polyvinyl fluoride (PVF), polyethylene naphthalate (PEN) and Kapton FN (poly-oxydiphenylene-pyromellitimide) was possible using a laser-EUV source in the wavelength range of 9 – 70 nm [89]. The source consisted of a gas puff target irradiated under high vacuum (10^{-5} mbar) by a 1064 nm Nd:YAG operating at a pulse energy of 0.8 J, a pulse repetition rate of 10 Hz and a pulse width of 3 ns. The gas target was high-Z gas such as xenon or krypton, contained within a steam of helium to limit expansion of the target gas within the vacuum chamber.

Figure 2.9 shows surfaces resulting from single shot exposure at a fluence of 60 mJ/cm^2 which produced nanostructures of 200 – 300 nm high, while multiple shot exposures produced similar structures with larger characteristic sizes (for 10 shots, features of over 1 µm were seen) [88]. When texturing poly(vinylidenefluoride) (PVDF) intense material ablation was produced for high fluence shots, while defluorination and carbon enrichment occurred for low fluence shots [90]. Further nanostructuring of the surface was performed via acetone exposure [91] which in this case led to an increase in the biocompatibility of the resultant polymer surfaces [92].

Recently, EUV treatment using 13.5 nm radiation also led to the production of micron-scale features with high dimensional accuracy (1 µm diameter, 4 µm depth) on PMMA and PDMS surfaces [93]. Though EUV processing has yet to be applied to the fabrication of UTLC systems, the resultant feature sizes and morphology would make suitable substrates for UTLC plates once functionalised.

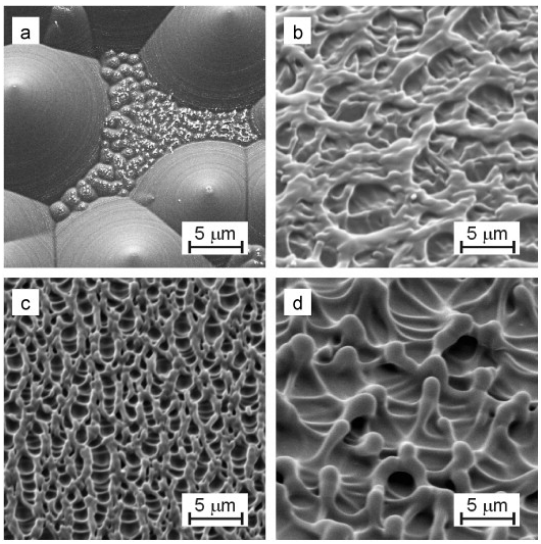

Figure 2.9: SEM images showing the surface of (a) Kapton HN, (b) PVF, (c) PEN and (d) PVDC after EUV exposure [89].

2.4 Alternative Fabrication Methods

There are several other alternative manufacturing methods also capable of producing features on the scale required for the fabrication of UTLC plates. Those summarised here include Matrix-assisted Pulsed Laser Evaporation, Thermal Annealing, and Plasma Processing. Both plasma processing and annealing have been utilised as a supplementary technique in the production of UTLC plates [43,44,46,94]. However, as with laser processing, to date, none of these techniques have yet to be utilised as the primary technique for UTLC plate fabrication.

2.4.1 Matrix-Assisted Pulsed Laser Evaporation

Two techniques known as Matrix-Assisted Pulsed Laser Evaporation (MAPLE) and MAPLE direct-write (MAPLE DW) have been demonstrated for use in the production of thin-films of organic materials. In this process, the matrix (a solution of a solvent and the desired polymer) is subject to high-power laser irradiation which causes desorption of the matrix from the target. The material is then allowed to impact upon a substrate allowing deposition to take place. MAPLE DW is conducted under atmospheric conditions, where the target solution is coated on a transparent ribbon and shows similar capabilities to MAPLE with a less complicated process setup [95].

Depositions of fluoroalcoholpolysiloxane polymer (SXFA) for the fabrication of chemiresistor gas sensors were conducted using MAPLE. The process was shown to

be capable of producing thin-films on the order of 100 nm thickness, with a surface roughness ($R_{RMS} \approx 20$ nm) lower than that of conventional spray-coated SXFA films. This technique could be utilised for the deposition of functional thin polymer film stationary phases on inert planar substrates for TLC applications, though to date no study has examined this possibility.

2.4.2 Thermal Annealing

Thermal annealing is a process which involves heating a material beyond its melting point then allowing cooling to take place for a certain time. Thermal annealing has proved a very effective and simple method for texturing polymer surfaces whereby crystallisation of polymer chains and stress relaxation resulted in an increase in surface roughness [96]. Some such preparation work was conducted on PTFE showing changes in surface morphology when annealed [96]. PTFE sheets of 4 mm thickness were cut into 18 mm squares, polished and washed in ethanol in an ultrasonic bath. Samples were annealed at 350 °C for between 10 and 120 minutes, and cooled for between 0 to 150 minutes. Figure 2.10 shows the resultant samples at various annealing times. The main texturing processes seen were stress relaxation and crystallisation, leading to the formation of dendrites and warts on the surface on the order of 1 – 3 µm. Samples annealed for all temperatures showed some degree of change in surface roughness values.

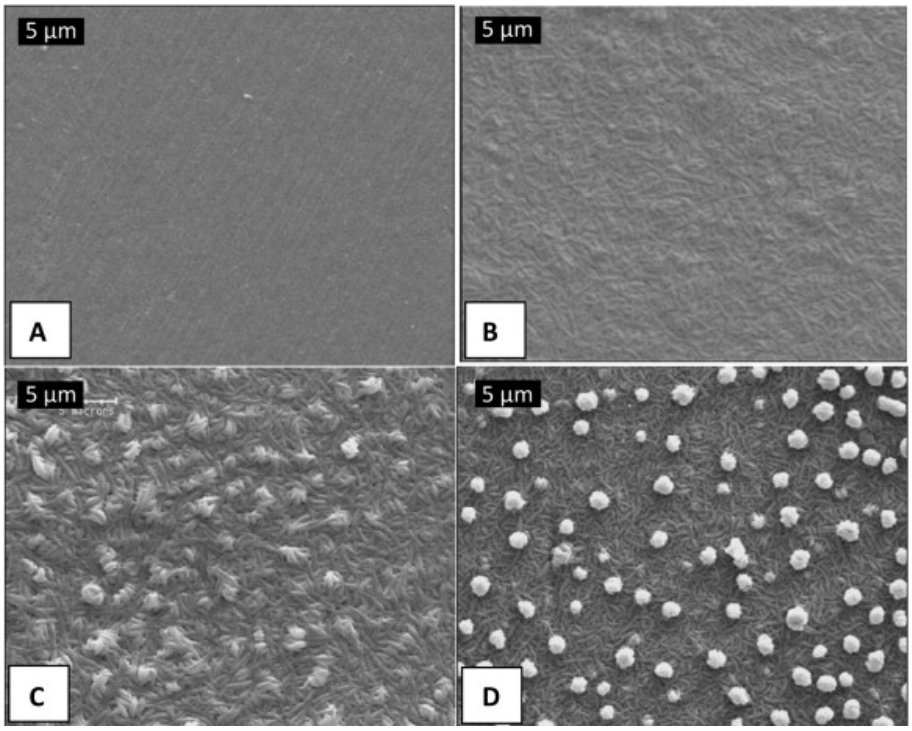

Figure 2.10: SEM images of (a) untreated and annealed PTFE samples at 350 °C for a duration of (b) 10 min; (c) 20 min and (d) 75 min [96].

Thermal annealing has yet to be applied in the fabrication of UTLC systems, however it could be considered a complimentary to techniques such as LDW−. Annealing would allow for increasing surface roughness of polymer surfaces which could then be used in LDW− processing and subsequently functionalised. The resultant substrate would have high-surface area for improved sample-stationary phase interaction to take place.

2.4.3 Plasma Etch Processing and Surface Modification

Plasma processing is widely used in applications such as semiconductor manufacturing, material deposition, substrate etching and surface modification. This form of processing has also been applied to the modification of polymer surfaces and has been used in the creation of polymer-based microfluidic devices. Plasma processing is capable of long-term modification of both the surface morphology, wettability and chemistry of polymer surfaces [97]. This modification is a combination of processes such as bond breakage, radical generation and polymer chain truncation and crosslinking. These processes lead to an increased surface micro-roughness and thus an increase in surface area for both chemical and physical interaction.

Argon and argon-oxygen plasma treatments were shown to greatly increase the hydrophilicity of cyclic olefin polymer surfaces, with a reduction in the contact angle from 90° to 68° after plasma exposure [98]. A plasma surface treatment of polyetheretherketone (PEEK) using an RF-driven Ar/O plasma was demonstrated to be capable of forming 1 μm size fibrous structures on PEEK surfaces [99]. The resultant surfaces are shown in Figure 2.11. One notable result was the change in the contact angle after plasma, laser and both laser and plasma exposure. The native contact angle for pristine PEEK was measured at 75° which was reduced to 0° after plasma exposure.

When combined with LDW− both micro- and nanostructures were evident on the substrate surface as a result of the laser and plasma processing respectively [99]. The contact angle increased to 110° for substrates which were solely laser processed, and when plasma exposure was followed by laser processing a contact angle of 120° was seen. This super-hydrophobic behaviour was attributed to both the increased surface roughness as a result of both laser-texturing and plasma exposure, and the change in surface chemistry, though the exact mechanism was not determined.

Though plasma processing has yet to be applied to the creation of UTLC systems, the above examples exemplify plasma processing as both a standalone and complimentary process to LDW−. Plasma processing also allows for fine control over the wettability characteristics of the polymer surfaces which has previously been exploited for the creation of microfluidic devices [97].

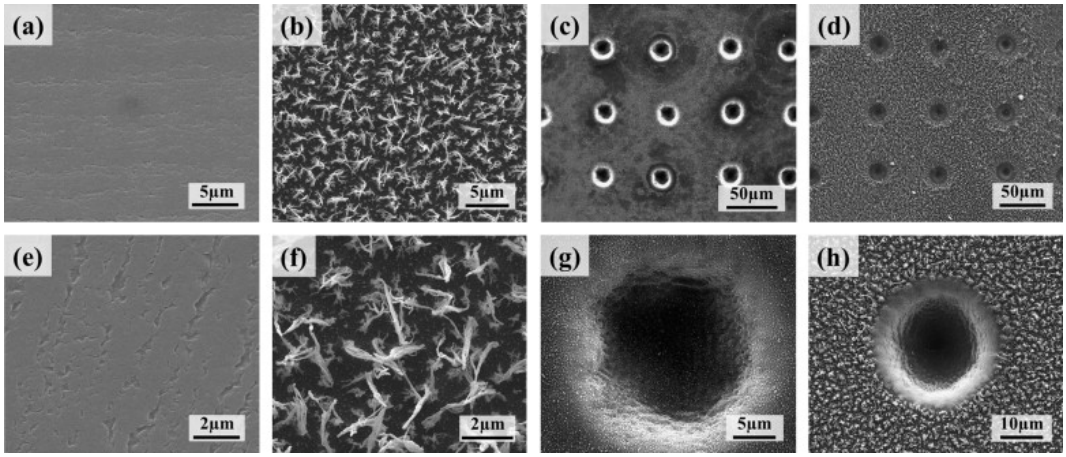

Figure 2.11: PEEK (a) Untreated, (b) plasma processed, (c) laser processed and (d) plasma and laser treated; (e–h) show higher magnified images of (a-d) in the same order [99].

2.5 Conclusions

Ultra-thin layer chromatography is a fast-evolving, emerging field of planar chromatography with efficiencies comparable or better than existing HP-TLC processes. Although conventional TLC has typically been employed as a method for protocol development for liquid chromatographic techniques, TLC has proved to be a powerful analytical technique in itself due to advances such as HP-TLC, UTLC and increased robustness in TLC plate preparation. As a result of the achieved faster separations and lower limits of detection when compared to TLC, HP-TLC is now used in a variety of analytical applications, and has been deployed in conjunction with mass spectrometry techniques such as MALDI for enhanced detection [16,35].

UTLC represents the next stage in the development of thin layer chromatography. The reduction in sorbent layer thickness requires the use of advanced fabrication techniques such as atomic layer deposition or electrospinning. This reduction in layer thickness also presents problems unique to UTLC. One such issue is reduced sample and mobile phase capacity within the sorbent layer when compared to HP-TLC. This issue has been solved through new sample application methods. Indeed, sample application and detection for UTLC through adaption of existing HP-TLC equipment, as well as office printers and scanners has been presented [100].

There are a number of techniques reported to date which form the majority of the reports of the creation of UTLC stationary phases such as chemical deposition of

monolithic films (through either photopolymerisation or a sol-gel process), glancing angle deposition (GLAD) of inorganic metal nanorods, and electrospun polymer nanowires. Though these constitute the majority of the published literature on UTLC, there are a number of other research groups utilising different techniques in the field, such as CVD and 3DP. To date, these have been applied to and proven effective in a number of separation applications, including the separation of organic dye solutions.

GLAD has been demonstrated as extremely effective in the creation of metal oxide nanowire coatings; however, the process is both slow and quite complex, requiring a high-vacuum environment for depositions. Similarly, the sol-gel process is both labour and time intensive. Electrospinning of polymer nanowires has proven effective in the creation of UTLC stationary phases but requires the use of environmentally harmful solvents such as DMF for the polymer to be extruded. Furthermore, each of the three techniques mentioned are slow techniques, removing the possibility for rapid prototyping of devices.

Of all the methods presented in the literature for the fabrication of UTLC platforms, one technique which has not been examined to-date is laser material processing techniques such as laser ablation and LDW-. These techniques offer fast and scalable method for fabrication of micron-scale features on surfaces. Laser processing also offers cost-effective production, which is essential for planar chromatographic platform fabrication, as commercial plate costs are low.

Furthermore, laser processing is capable of the creation of feature sizes in the range of single to tens of microns, which is critical in UTLC plate fabrication. The speed at which devices can be created via laser processing allows for rapid prototyping, reducing optimisation time, as well as the potential for much more efficient mass scale production, both of which may further reduce device costs at a commercial level. This contrasts with the previously demonstrated techniques for UTLC plate fabrication, such GLAD and CVD which, though commercially compatible, do not have the capability for rapid prototyping. Additionally, GLAD and CVD utilise precursor gases and produce by-products which are environmentally harmful. manufacturing has moved towards environmentally-friendly production techniques, laser processing offers a “green” route production route for the of UTLC plates`.

Overall, the adaptability, capabilities and speed of laser processing made it the selected process for examination for the fabrication of novel polymer-based UTLC plates in this thesis.

References

[1] Touchstone JC, Dobbins MF. Practice of Thin Layer Chromatography. 2nd ed. New York: John Wiley & Sons, Inc.; 1983.

[2] Wall PE. Thin-Layer Chromatography. Thin-Layer Chromatography: A Modern Practical Approach. Cambridge: Royal Society of Chemistry; 2005.

[3] Agarwal R, Behari JR. Screening for Mercury in Aqueous Environmental Samples and Urine Samples Using Thin Layer Chromatography. Water Environ Res. 2007 Nov 1;79(12):2457–63.

[4] Adam CD, Sherratt SL, Zholobenko VL. Classification and individualization of black ballpoint pen inks using principal component analysis of UV-vis absorption spectra. Forensic Sci Int. 2008 Jan 15;174(1):16–25.

[5] Takeshita R. Application of column and thin-layer chromatography to the detection of artificial sweeteners in foods. J Chromatogr A. 1972 Apr;66(2):283–93.

[6] Ferenczi-Fodor K, Végh Z, Renger B. Thin-layer chromatography in testing the purity of pharmaceuticals. TrAC Trends Anal Chem. 2006 Sep;25(8):778–89.

[7] Izmailov M, Shraiber M. Spot Chromatographic Adsorption Analysis and its Application in Pharmacy Communication. Farmatsiya. 1938;3:1–7.

[8] Meinhard JE, Hall NF. Surface Chromatography. Anal Chem. 1949;21:185–8.

[9] Hauck HE, Schulz M. Ultra Thin-Layer Chromatography. Chromatographia. 2003;57(1):S313-5.

[10] Hauck H, Bund O, Fischer W, Schulz M. Ultra-thin layer chromatography (UTLC) — A new dimension in thin-layer chromatography. J Planar Chromatogr – Mod TLC. 2001 Aug;14(4):234–6.

[11] Cserháti T, Ester F. Introduction to Techniques and Instrumentation. In: Fried B, Sherma J, editors. Practical Thin-Layer Chromatography: a multidisciplinary approach. Boca Raton, Florida, USA: CRC Press, Inc; 1996. p. 1–18.

[12] Spangenberg B, Poole CF, Weins C. Quantitative Thin-Layer Chromatography. Berlin, Heidelberg: Springer Berlin Heidelberg; 2011.

[13] Li R, Wang L, Gao X, Du G, Zhai H, Wang X, et al. Rapid separation and sensitive determination of banned aromatic amines with plastic microchip electrophoresis. J Hazard Mater. 2013 Mar 15;248–249:268–75.

[14] Cheng S-C, Huang M-Z, Shiea J. Thin-layer chromatography/laser-induced

acoustic desorption/electrospray ionization mass spectrometry. Anal Chem. 2009 Nov 15;81(22):9274–81.

[15] Tuzimski T. Advanced Spectroscopic Detectors for Identification and Quantification. In: Instrumental Thin-Layer Chromatography. Elsevier; 2015. p. 239–48.

[16] Zhang Z, Ratnayaka SN, Wirth MJ. Protein UTLC-MALDI-MS using thin films of submicrometer silica particles. J Chromatogr A. 2011 Oct 7;1218(40):7196–202.

[17] Halpaap H. Achievement of reproducible separations by the application of standardized sorbents in specified systems. J Chromatogr A. 1973 Apr;78:77–87.

[18] Sherma J. Planar chromatography. Anal Chem. 1992;64(12):134R–147R.

[19] Poole C. Instrumental Thin-Layer Chromatography. Amsterdam: Elsevier B.V.; 2015.

[20] Del Bubba M, Checchini L, Lepri L. Thin-layer chromatography enantioseparations on chiral stationary phases: a review. Anal Bioanal Chem. 2013 Jan 17;405(2–3):533–54.

[21] Ferenczi-Fodor K, Végh Z, Renger B. Impurity profiling of pharmaceuticals by thin-layer chromatography. J Chromatogr A. 2011 May;1218(19):2722–31.

[22] Hauck HE, Schulz M. Ultrathin-Layer Chromatography. J Chromatogr Sci. 2002 Nov 1;40(10):550–2.

[23] Mennickent S, de Diego M, Vega M, Diego M, Vega M. Ultrathin-Layer Chromatography (UTLC). Chromatographia. 2013 Oct 26;76(19–20):1233–8.

[24] Newsome TE, Olesik S V. Silica-based nanofibers for electrospun ultra-thin layer chromatography. J Chromatogr A. 2014 Oct 17;1364:261–70.

[25] Poole SK, Poole CF. High performance stationary phases for planar chromatography. J Chromatogr A. 2011 May 13;1218(19):2648–60.

[26] Steach JK, Clark JE, Olesik S V. Optimization of electrospinning an SU-8 negative photoresist to create patterned carbon nanofibers and nanobeads. J Appl Polym Sci. 2010 Oct 5;118(1):405–12.

[27] Clark JE, Olesik S V. Technique for ultrathin layer chromatography using an electrospun, nanofibrous stationary phase. Anal Chem. 2009 May 15;81(10):4121–9.

[28] Beilke MC, Zewe JW, Clark JE, Olesik S V. Aligned electrospun nanofibers

for ultra-thin layer chromatography. Anal Chim Acta. 2013 Jan 25;761:201–8.

[29] Moheman A, Alam MS, Gupta A, Dhakate SR, Kumar A, Mohammad A, et al. Fabrication of nanofiber stationary phases from chopped polyacrylonitrile co-polymer microfibers for use in ultrathin layer chromatography of amino acids. RSC Adv. 2016;6(93):90100–10.

[30] Clark JE, Olesik S V. Electrospun glassy carbon ultra-thin layer chromatography devices. J Chromatogr A. 2010 Jul 2;1217(27):4655–62.

[31] Lu T, Olesik S V. Electrospun polyvinyl alcohol ultra-thin layer chromatography of amino acids. J Chromatogr B Anal Technol Biomed Life Sci. 2013 Jan 1;912:98–104.

[32] Macdonald NP, Currivan SA, Tedone L, Paull B. Direct Production of Microstructured Surfaces for Planar Chromatography Using 3D Printing. Anal Chem. 2017 Feb 21;89(4):2457–63.

[33] Soper SA, Henry AC, Vaidya B, Galloway M, Wabuyele M, McCarley RL. Surface modification of polymer-based microfluidic devices. Anal Chim Acta. 2002 Oct;470(1):87–99.

[34] Vázquez M, Paull B. Review on recent and advanced applications of monoliths and related porous polymer gels in micro-fluidic devices. Anal Chim Acta. 2010 Jun 4;668(2):100–13.

[35] Bakry R, Bonn GK, Mair D, Svec F. Monolithic porous polymer layer for the separation of peptides and proteins using thin-layer chromatography coupled with MALDI-TOF-MS. Anal Chem. 2007 Jan 15;79(2):486–93.

[36] Siouffi AA-M. Silica gel-based monoliths prepared by the sol-gel method: facts and figures. J Chromatogr A. 2003;1000(1–2):801–18.

[37] Zou H, Huang X, Ye M, Luo Q. Monolithic stationary phases for liquid chromatography and capillary electrochromatography. J Chromatogr A. 2002 Apr;954(1–2):5–32.

[38] Tanaka N, Kobayashi H, Ishizuka N, Minakuchi H, Nakanishi K, Hosoya K, et al. Monolithic silica columns for high-efficiency chromatographic separations. J Chromatogr A. 2002 Aug;965(1–2):35–49.

[39] Frolova AM, Konovalova OY, Loginova LP, Bulgakova A V, Boichenko AP. Thin-layer chromatographic plates with monolithic layer of silica: Production, physical-chemical characteristics, separation capabilities. J Sep Sci. 2011 Jul 18;34:n/a-n/a.

[40] Fichou D, Morlock GE. Open-Source-Based 3D Printing of Thin Silica Gel Layers in Planar Chromatography. Anal Chem. 2017 Feb 7;89(3):2116–22.

[41] Robbie K, Brett MJ. Sculptured thin films and glancing angle deposition: Growth mechanics and applications. J Vac Sci Technol A Vacuum, Surfaces, Film. 1997 May;15(3):1460–5.

[42] Jim SR, Taschuk MT, Morlock GE, Bezuidenhout LW, Schwack W, Brett MJ. Engineered Anisotropic Microstructures for Ultrathin-Layer Chromatography. Anal Chem. 2010 Jun 15;82(12):5349–56.

[43] Jim SR, Oko AJ, Taschuk MT, Brett MJ. Morphological modification of nanostructured ultrathin-layer chromatography stationary phases. J Chromatogr A. 2011 Oct 7;1218(40):7203–10.

[44] Wannenmacher J, S. Jim M, Taschuk T, Brett MJ, Morlock GE, Jim SR, et al. Ultrathin-layer Chromatography on SiO2, Al2O3, TiO2 and ZrO2 nanostructered thin films. J Chromatogr A. 2013 Nov;1318:234–43.

[45] Bezuidenhout LW, Brett MJ. Ultrathin layer chromatography on nanostructured thin films. J Chromatogr A. 2008 Mar 7;1183(1–2):179–85.

[46] Hall JZ, Taschuk MT, Brett MJ. Polarity-adjustable reversed phase ultrathin-layer chromatography. J Chromatogr A. 2012 Nov 30;1266:168–74.

[47] Oko AJ, Jim SR, Taschuk MT, Brett MJ. Analyte migration in anisotropic nanostructured ultrathin-layer chromatography media. J Chromatogr A. 2011 May 13;1218(19):2661–7.

[48] Kauppila TJ, Talaty N, Salo PK, Kotiaho T, Kostiainen R, Cooks RG. New surfaces for desorption electrospray ionization mass spectrometry: porous silicon and ultra-thin layer chromatography plates. Rapid Commun Mass Spectrom. 2006 Jul 30;20(14):2143–50.

[49] Salo PK, Salomies H, Harju K, Ketola RA, Kotiaho T, Yli-Kauhaluoma J, et al. Analysis of small molecules by ultra thin-layer chromatography-atmospheric pressure matrix-assisted laser desorption/ionization mass spectrometry. J Am Soc Mass Spectrom. 2005 Jun;16(6):906–15.

[50] Oko AJ, Jim SR, Taschuk MT, Brett MJ. Time resolved chromatograms in ultra-thin layer chromatography. J Chromatogr A. 2012 Aug 3;1249:226–32.

[51] Song J, Jensen DS, Hutchison DN, Turner B, Wood T, Dadson A, et al. Carbon-Nanotube-Templated Microfabrication of Porous Silicon-Carbon Materials with Application to Chemical Separations. Adv Funct Mater. 2011 Mar

22;21(6):1132–9.

[52] Kanyal SS, Jensen DS, Miles AJ, Dadson AE, Vail MA, Olsen R, et al. Effects of catalyst thickness on the fabrication and performance of carbon nanotube-templated thin layer chromatography plates. J Vac Sci Technol B, Nanotechnol Microelectron Mater Process Meas Phenom. 2013 May;31(3):031203.

[53] Jensen DS, Kanyal SS, Gupta V, Vail MA, Dadson AE, Engelhard M, et al. Stable, microfabricated thin layer chromatography plates without volume distortion on patterned, carbon and Al2O3-primed carbon nanotube forests. J Chromatogr A. 2012 Sep;1257:195–203.

[54] Kanyal SS, Häbe TT, Cushman C V., Dhunna M, Roychowdhury T, Farnsworth PB, et al. Microfabrication, separations, and detection by mass spectrometry on ultrathin-layer chromatography plates prepared via the low-pressure chemical vapor deposition of silicon nitride onto carbon nanotube templates. J Chromatogr A. 2015 Jul;1404:115–23.

[55] Jensen DS, Kanyal SS, Madaan N, Miles AJ, Davis RC, Vanfleet R, et al. Ozone priming of patterned carbon nanotube forests for subsequent atomic layer deposition-like deposition of SiO_2 for the preparation of microfabricated thin layer chromatography plates. J Vac Sci Technol B, Nanotechnol Microelectron Mater Process Meas Phenom. 2013;31(3):031803.

[56] Zhou Y, Hong MH, Fuh JYH, Lu L, Lukyanchuk BS, Wang ZB. Near-field enhanced femtosecond laser nano-drilling of glass substrate. J Alloys Compd. 2008 Jan;449(1–2):246–9.

[57] Caiazzo F, Curcio F, Daurelio G, Minutolo FMC. Laser cutting of different polymeric plastics (PE, PP and PC) by a CO2 laser beam. J Mater Process Technol. 2005 Feb;159(3):279–85.

[58] Choudhury IA, Shirley S. Laser cutting of polymeric materials: An experimental investigation [Internet]. Vol. 42, Optics & Laser Technology. Elsevier; 2010. p. 503–8.

[59] Prakash S, Acherjee B, Kuar AS, Mitra S. An experimental investigation on Nd:YAG laser microchanneling on polymethyl methacrylate submerged in water. Proc Inst Mech Eng Part B J Eng Manuf. 2013 Apr 7;227(4):508–19.

[60] Ozdemir M, Sadikoglu H. A new and emerging technology: Laser-induced surface modification of polymers. Trends Food Sci Technol. 1998 Apr;9(4):159–67.

[61] Chikarakara E, Naher S, Brabazon D. High speed laser surface modification of Ti-6Al-4V. Surf Coatings Technol. 2012 Mar;206(14):3223–9.

[62] Tiaw KSS, Hong MHH, Teoh SHH. Precision laser micro-processing of polymers. J Alloys Compd. 2008 Jan;449(1–2):228–32.

[63] Cheng J-Y, Wei C-W, Hsu K-H, Young T-H. Direct-write laser micromachining and universal surface modification of PMMA for device development. Sensors Actuators B Chem. 2004 Apr;99(1):186–96.

[64] Bundgaard F, Perozziello G, Geschke O. Rapid prototyping tools and methods for all-Topas® cyclic olefin copolymer fluidic microsystems. Proc Inst Mech Eng Part C J Mech Eng Sci. 2006 Jan 1;220(11):1625–32.

[65] Sabbert D, Landsiedel J, Bauer H-D, Ehrfeld W. ArF-excimer laser ablation experiments on Cycloolefin Copolymer (COC). Appl Surf Sci. 1999 Aug;150(1–4):185–9.

[66] Lyutakov O, Huttel I, Siegel J, Švorčík V. Regular surface grating on doped polymer induced by laser scanning. Appl Phys Lett. 2009 Oct 26;95(17):173103.

[67] Lyutakov O, Tůma J, Huttel I, Prajzler V, Siegel J, Švorčík V. Polymer surface patterning by laser scanning. Appl Phys B. 2013 Jan 9;110(4):539–49.

[68] Yagyu H. Visible laser microfabrication of transparent plastic using Au nanoparticles-dispersed polymer film. J Mater Process Technol. 2010 Jun;210(9):1153–8.

[69] Rebollar E, Castillejo M, Ezquerra TA. Laser induced periodic surface structures on polymer films: From fundamentals to applications. Eur Polym J. 2015 Dec 1;73:162–74.

[70] Li M, Lu QH, Yin J, Sui Y, Li G, Qian Y, et al. Periodic microstructure induced by 532 nm polarized laser illumination on poly(urethane-imide) film: orientation of the azobenzene chromophore. Appl Surf Sci. 2002 Jun 5;193(1–4):46–51.

[71] Sanz M, Rebollar E, Ganeev RA, Castillejo M. Nanosecond laser-induced periodic surface structures on wide band-gap semiconductors. Appl Surf Sci. 2013 Aug 1;278:325–9.

[72] Wang J, Niino H, Yabe A. One-step microfabrication of fused silica by laser ablation of an organic solution. Appl Phys A Mater Sci Process. 1999 Jan 1;68(1):111–3.

[73] Wang J, Niino H, Yabe A. Microfabrication of a Fluoropolymer Film Using Conventional XeCl Excimer Laser by Laser-Induced Backside Wet Etching. Jpn J Appl Phys. 1999 Jul 1;38(Part 2, No. 7A):L761–3.

[74] Serafetinides AA, Skordoulis CD, Makropoulou MI, Kar AK. Picosecond and subpicosecond visible laser ablation of optically transparent polymers. Appl Surf Sci. 1998;135(1–4):276–84.

[75] Chang T-C, Molian PA. Excimer pulsed laser ablation of polymers in air and liquids for micromachining applications. J Manuf Syst. 1999 Jan;18(2):1–17.

[76] Baudach S, Bonse J, Krüger J, Kautek W, Kruger J. Ultrashort pulse laser ablation of polycarbonate and polymethylmethacrylate. Appl Surf Sci. 2000 Feb;154–155:555–60.

[77] Marco C De, Eaton SM, Suriano R, Turri S, Levi M, Ramponi R, et al. Surface Properties of Femtosecond Laser Ablated PMMA. ACS Appl Mater Interfaces. 2010 Aug;2(8):2377–84.

[78] Kunz T, stebani J, Ihlemann J, Wokaun A. Photoablation and microstructuring of polyestercarbonates and their blends with a XeCl eximer laser. Appl Phys A Mater Sci Process. 1998;67:345–52.

[79] Urech L, Lippert T, Phipps CR, Wokaun A. Polymer ablation: From fundamentals of polymer design to laser plasma thruster. Appl Surf Sci. 2007 May;253(15):6409–15.

[80] Gaspard S, Forster M, Huber C, Zafiu C, Trettenhahn G, Kautek W, et al. Femtosecond laser processing of biopolymers at high repetition rate. Phys Chem Chem Phys. 2008 Oct 10;10(40):6174.

[81] Serafetinides A, Makropoulou MI, Skordoulis CDD, Kar AKK, Serafetubudes AA. Ultra-short pulsed laser ablation of polymers. Appl Surf Sci. 2001 Aug;180(1–2):42–56.

[82] Tokarev VN, Kaplan AFH. Suppression of melt flows in laser ablation: application to clean laser processing. J Phys D Appl Phys. 1999 Jul 7;32(13):1526–38.

[83] Al-Hamaoy A, Chikarakara E, Jawad H, Gupta K, Kumar D, Rao MSR, et al. Liquid Phase – Pulsed Laser Ablation: A route to fabricate different carbon nanostructures. Appl Surf Sci. 2014 May;302:141–4.

[84] Weng X, Bi H, Liu B, Kong J. On-chip chiral separation based on bovine serum albumin-conjugated carbon nanotubes as stationary phase in a microchannel.

Electrophoresis. 2006 Aug;27(15):3129–35.

[85] Donnelly T, Lunney JG. Confined laser ablation for single-shot nanoparticle deposition of silver. Appl Surf Sci. 2013 Oct;282:133–7.

[86] Lippert T, Wei J, Wokaun A, Hoogen N, Nuyken O. Polymers designed for laser microstructuring. Appl Surf Sci. 2000 Dec;168(1–4):270–2.

[87] Inam Ul Ahad, Bartnik A, Fiedorowicz H, Kostecki J, Korczyc B, Ciach T, et al. Surface modification of polymers for biocompatibility via exposure to extreme ultraviolet radiation. J Biomed Mater Res A. 2014 Sep 25;102(9):3298–310.

[88] Bartnik A, Fiedorowicz H, Jarocki R, Kostecki J, Szczurek M, Chernyayeva O, et al. EUV-induced physico-chemical changes in near-surface layers of polymers. J Electron Spectros Relat Phenomena. 2011 Apr;184(3–6):270–5.

[89] Bartnik A, Fiedorowicz H, Jarocki R, Kostecki J, Szczurek M, Wachulak PW. Laser-plasma EUV source dedicated for surface processing of polymers. Nucl Instruments Methods Phys Res Sect A Accel Spectrometers, Detect Assoc Equip. 2011 Aug;647(1):125–31.

[90] Bartnik A, Fiedorowicz H, Jarocki R, Kostecki J, Szczurek M, Wachulak PW. Efficient micromachining of poly(vinylidene fluoride) using a laser-plasma EUV source. Appl Phys A. 2011 Nov 11;106(3):551–5.

[91] Bartnik A, Fiedorowicz H, Burdyńska S, Jarocki R, Kostecki J, Szczurek M. Combined effect of EUV irradiation and acetone treatment on PET surface. Appl Phys A. 2010 Aug 20;103(1):173–8.

[92] Reisinger B, Fahrner M, Frischauf I, Yakunin S, Svorcik V, Fiedorowicz H, et al. EUV micropatterning for biocompatibility control of PET. Appl Phys A Mater Sci Process. 2010 Jun 22;100(2):511–6.

[93] Torii S, Makimura T, Okazaki K, Nakamura D, Takahashi A, Okada T, et al. Micromachining of polydimethylsiloxane induced by laser plasma EUV light. In: Juha L, Bajt S, London RA, editors. 2011. p. 807714-807714–6.

[94] Jim SR, Foroughi-Abari A, Krause KM, Li P, Kupsta M, Taschuk MT, et al. Ultrathin-layer chromatography nanostructures modified by atomic layer deposition. J Chromatogr A. 2013 Jul 19;1299:118–25.

[95] Piqué A, Auyeung RC., Stepnowski J., Weir D., Arnold C., McGill R., et al. Laser processing of polymer thin films for chemical sensor applications. Surf Coatings Technol. 2003 Jan;163–164:293–9.

[96] Glaris P, Coulon J-F, Dorget M, Poncin-Epaillard F. Thermal annealing as a new simple method for PTFE texturing. Polymer (Guildf). 2013 Oct;54(21):5858–64.

[97] Roy S, Yue CY, Lam YC. Influence of plasma surface treatment on thermal bonding and flow behavior in Cyclic Olefin Copolymer (COC) based microfluidic devices. Vacuum. 2011 Jun;85(12):1102–4.

[98] Roy S, Yue CY, Lam YC, Wang ZY, Hu H. Surface analysis, hydrophilic enhancement, ageing behavior and flow in plasma modified cyclic olefin copolymer (COC)-based microfluidic devices. Sensors Actuators B Chem. 2010 Oct 28;150(2):537–49.

[99] Akkan CK, Hammadeh M, Brück S, Park HW, Veith M, Abdul-Khaliq H, et al. Plasma and short pulse laser treatment of medical grade PEEK surfaces for controlled wetting. Mater Lett. 2013 Oct;109:261–4.

[100] Morlock GE, Oellig C, Bezuidenhout LW, Brett MJ, Schwack W. Miniaturized Planar Chromatography Using Office Peripherals. Anal Chem. 2010 Apr;82(7):2940–6.

Chapter 3

Microchannel fabrication on cyclic olefin polymer substrates via 1064 nm Nd:YAG laser ablation

Publication Status: Published

McCann R, Bagga K, Groarke R, Stalcup A, Vázquez M, Brabazon D. Microchannel fabrication on cyclic olefin polymer substrates via 1064 nm Nd:YAG laser ablation. Appl Surf Sci 2016;387:603-608.

DOI: 10.1016/j.apsusc.2016.06.059

Abstract

This chapter presents the first development of a method for fabrication of microchannels on Cyclic Olefin Polymer (COP) films using an infrared Nd:YAG laser, with an aim to the development of substrates suitable for novel polymer-based UTLC platforms. Though the focus of this work is an investigation into the production of microchannels on COP substrates for UTLC, it is also of interest towards applications in areas such as microfluidics and chemical sensing. Continuous microchannels were fabricated on 188-µm-thick cyclic olefin polymer substrates using a picosecond pulsed 1064 nm Nd:YAG laser. The effect of laser fluence on the microchannel dimension and morphology was analysed via scanning electron microscopy and optical profilometry. Single laser passes were found to produce v-shaped microchannels with depths ranging from 12 to 47 µm and widths from 44 to 155 µm. The ablation rate during processing was lower than predicted theoretically. Multiple laser passes were applied to examine this process for achieving a further degree of control over the resultant microchannel dimensions, with channel depths ranging from 22 µm to 77 µm and channel widths from 58 µm to 155 µm for between three and eleven passes. For up to five repeat passes, acceptable reproducibility was found in the produced microchannel morphology. Infrared spectroscopy revealed oxidation and dehydrogenation of the polymer surface via the laser ablation process. These results were compared to other works conducted on cyclic olefin polymers.

3.1 Introduction

Until recently, the typical materials of choice for microfluidic devices and micro-total analysis systems have been glass or polymers such as polymethyl methacrylate (PMMA), polycarbonate (PC), and polydimethylsiloxane (PDMS). These materials have good mechanical properties, allowing for easy processing but often lack good optical transparency in the mid-ultraviolet spectrum (200 – 300 nm). Optical transparency in this range is crucial for the optical analysis of many organic compounds such as aromatics, proteins and nucleic acids. Cyclic-olefin polymer (COP) and co-polymer (COC) are emerging new classes of polymers which have been noted for their low cost, high chemical resistance, biocompatibility and high optical transparency from NIR to mid-UV wavelengths [1]. COPs are also recognized for their low water absorption and high mechanical and dimensional stability when in contact with liquids, and as such make extremely suitable platforms for microfluidic devices when compared with previously used alternatives. Owing to these exceptional properties, COP-based devices have been utilised for various applications such as substrates for chromatographic stationary phases [2] and microfluidic devices for the analysis of drugs [3], IR waveguide coatings [4] and as substrates for laser deposited nanomaterials [5].

For microfluidic device fabrication, techniques such as xurography [6], micromilling [7], UV-polymerisation [8] and, more recently, 3D printing [9,10] allow for fast and flexible prototyping of devices leading to shorter periods of device optimisation. For large-scale fabrication of devices, techniques such as hot embossing [11] or injection moulding [12] tend to be used due to their cost-effectiveness. However, these lack the ability for rapid prototyping due to the requirement of expensive moulds or negatives to be fabricated. Contrastingly, laser processing provides a fast, repeatable, clean and cost-efficient method of microfluidic device manufacturing. The use of laser processing [13–15] and pulsed laser ablation [16] has been demonstrated to be capable of both surface modification and creation of micro- and nanoscale structures on polymer surfaces, along with the incorporation of nanoparticles onto the substrate surface for functionalisation and nanotexturing [17].

Neodymium-doped yttrium aluminium garnet (Nd:YAG) lasers are widely used in industry for materials processing [18], however, very few studies have examined the

feasibility of using Nd:YAG lasers for the processing of cyclic olefin polymers [6]. Various alternative laser systems, such as ultra-violet and extreme ultra violet laser systems and femtosecond lasers, have been utilized for polymer processing in the past. UV excimer lasers have been used for the processing of optically transparent polymers [19], and specifically COC [20]. The low ablation depth per pulse for COC, which was found to be smaller when compared to PMMA, would allow for the creation of small features although the extent of ablation was seen to be dependent on the norbornene content of the copolymer [21]. However, UV excimer lasers tend to have higher operating cost and lower beam quality when compared to solid-state laser systems. Extreme ultraviolet (EUV) lasers, typically used in microelectronics manufacturing, have also been shown to be capable of nanoscale changes in depth and surface roughness of polymer surfaces due to low penetration depth of EUV radiation [22,23]. Despite these advantages, EUV lasers require a vacuum and highly specialised optics for operation and therefore are not well suited for the fabrication of low-cost microfluidic systems.

Femtosecond lasers, which interact with materials through non-linear photon absorption, have been demonstrated for the efficient processing of materials transparent to the wavelength of the laser used [16]. For COP processed using a femtosecond titanium sapphire (800 nm) laser, low surface roughness of the processed area was reported [24]. However, some degradation in optical transmission was seen due to a combination of oxidation and dehydrogenation when compared with PMMA or polystyrene (PS) processed under the same conditions. While the fast delivery of the laser photonic energy by femtosecond lasers allows for efficient processing of materials that have low absorption to the wavelength of the laser, these systems tend to be both more expensive and complicated to maintain than laser processing systems typically used in industry.

In this work, we examine the use of an infrared picosecond-pulsed Nd:YAG laser for direct-write fabrication of continuous microchannels on the surface of thin COP substrates. The use of multiple laser passes for a higher level of control of microchannel dimensions and morphology was also examined. Optical profilometry was used for dimensional analysis of the microchannels and scanning electron microscopy was performed to analyse changes in surface morphology. Raman and infrared spectroscopy were performed to examine the effect of laser processing on the surface chemistry.

3.2 Material and Methods

3.2.1 Materials

The substrate material used was ZeonorFilm ZF14-188 (Zeon Chemical, Japan) cyclic olefin polymer purchased from Ibidi (Germany), with a thickness of 188 µm. The polymer sheet was cut, cleaned with isopropanol and dried using compressed clean dry air to ensure the substrate was pristine prior to laser processing.

3.2.2 Laser processing and substrate fabrication

The direct-write laser system used consisted of a 1064 nm WEDGE HF Q-switched, diode-pumped solid-state neodymium-yttrium aluminium garnet laser (BrightSolutions Italy), specifications of which are listed in Table 3.1. A 2D scanning galvanometer (SS-12, Raylase, Germany) was used to raster the beam in the xy-plane, and a movable z-stage (M-404 4PD, PI, Germany) was used to control the position of the sample. The laser beam was focussed to a spot size of 140 µm and scanned unidirectionally across the sample at a speed of 1.2 mm/s to form parallel channels separated by 200 µm. The COP films were mechanically fastened to the sample stage for the duration of processing. Further details of the processing parameters are listed in Table 3.2.

Table 3.1: Specifications of the 1064 nm laser processing system.

Wavelength	1064 nm
Maximum Average Output Power	4.5 W
Maximum Pulse Energy	45 mJ
Repetition Rate	7.5 – 100 kHz
Pulse width	0.7 – 5.2 ns
Beam diameter	140 µm

Table 3.2: Process parameters used during laser processing of COP substrates.

Process Parameter	Single Pass	Multiple Passes
Fluence (J/cm^2)	0.15 – 0.78	0.51
Scan Rate (mm/s)	1.2	1.2
Beam diameter (µm)	140	140
Pulse Width (ps)	750	750
Pulse Repetition Frequency (kHz)	7.5	7.5
No. of passes	1	2 to 10

3.2.3 Characterisation

Scanning electron microscopy was conducted using an EVO LS15 (Zeiss, Switzerland) with LaB_6 filament, accelerating voltage of 10 kV, and a beam current intensity of 25 pA. Samples were gold coated using a ScanCoat Six (Edwards, UK) sputter coater set at a deposition current of 25 mA for 80 s, resulting in a coating thickness of 34 nm.

The profile of the microchannels was examined using a VHX-2000 (Keyence, Japan) 3D Optical Microscope. Samples were previously coated with a 68-nm-thick film of gold using the ScanCoat Six sputter coater, which was sufficient to reduce the transmission in the visible range by approximately 90% [25] and allow the sample surface to be imaged optically. Images were taken at 0.43 µm increments upwards from the base of the channel at 1000x magnification. For each sample, the average depth and width of four profiles from four channels were examined, for a total of 16 profiles per sample. For the figures presented hereafter, the error bars relate to a 90% confidence interval of the measured microchannels width and depth. To determine the accuracy of the applied fits to the microchannel depth and width plots, both the adjusted coefficient of determination (adjusted R-squared) and the Pearson's R-squared were calculated, while for non-linear fits, the adjusted R-squared and reduced Chi-squared were calculated.

The optical absorbance of the polymer film at the laser wavelength was examined using a Cary 50 (Varian, USA) UV-Vis spectrometer. Infrared spectroscopy was performed to examine changes to the substrate surface chemistry as a result of laser processing. Micro-Raman spectroscopy was conducted using a LabRam HR800 (Horiba Jobin Yvon, USA) system with an Ar^+ 488 nm air-cooled laser with 1 µm spot

size and an accumulation time of 20 s. The HR800 was operated in a backscattering configuration with a resolution of 1.1 cm^{-1}. FTIR spectroscopy was performed using a Perkin 100 spectrometer (PerkinElmer, USA) in attenuated total reflectance (ATR) mode which had a sampling depth of 1 – 2 μm. Spectra were collected with 4 scans at a resolution of 1 cm^{-1} over the range of 4000 – 650 cm^{-1}. A baseline correction was applied to the FTIR spectra using Origin Pro 9 (OriginLab, USA), to allow accurate comparison of relative peak intensities.

3.2.4 Calculation of ablation rate

The number of laser pulses, N, incident per unit area in a scanning beam can be estimated from the laser pulse repetition frequency, f, the beam waist, w_0, and scan rate, ν, as follows [26]:

$$N = \frac{w_0 f}{\nu} \qquad \textbf{Eqn. 3.2.1}$$

This allows determination of the experimental ablation rate, R_m, i.e. the amount of material removed per pulse, which can be estimated as the measured channel depth, d, divided by N:

$$R_m = \frac{d}{N} \qquad \textbf{Eqn. 3.2.2}$$

For the parameters used in this work, a value of 875 pulses per laser pass was calculated from Equation 3.2.1. Theoretical ablation rates, R_t i.e. the expected amount of material removed per pulse, can be calculated using:

$$R_t = \alpha^{-1} \times \ln\left(\frac{F}{F_{th}}\right) \qquad \textbf{Eqn. 3.2.3}$$

where F and F_{th} are the input and threshold fluences respectively. The "effective optical penetration depth", α^{-1}, from the *Beer-Lambert law* can be estimated from the

slope of the linear fit of a linear-log plot of the ablation rate versus fluence [27]. Predicted microchannel width, *W*, for an incident fluence of *F* can be estimated using w_0 and F_{th} [27] whereby:

$$W^2 = 2w_0^2 \times \ln\left(\frac{F}{F_{th}}\right) \qquad \textbf{Eqn. 3.2.4}$$

This equation assumes that the microchannel widths are equivalent to a single pulse ablation site rather than a scanning beam of multiple pulses. Some variation from the predicted values is expected as a result of the "incubation effect" [27], whereby defects generated by the interaction of multiple laser shots effectively lower the threshold fluence as the number of laser pulses increases. Despite this, Equation 3.2.4 can be used to estimate some of the expected variation between single and multiple scanning passes.

3.3 Results

3.3.1 Effect of laser fluence

The effect of laser fluence on the formation of microchannels on the substrate surface was investigated from the resultant 3D profiles. Both microchannel widths and depths were seen to increase logarithmically with laser fluence as shown in Figure 3.1. At the lowest fluence used (0.23 J/cm^2) microchannels 44 µm wide and 12 µm deep were formed. The highest fluence (0.79 J/cm^2) resulted in microchannels 154 µm in width and 47 µm in depth.

At all fluences trialled, microchannels with a V-shaped profile were formed, similar to the findings from other work conducted with COP [24], with re-cast ablation melt evident at the channel crests which reduced in size at higher fluences. For the maximum fluence used (0.79 J/cm^2) heat damage was evident through substrate warping and the appearance of large bubble-like formations on the substrate surface.

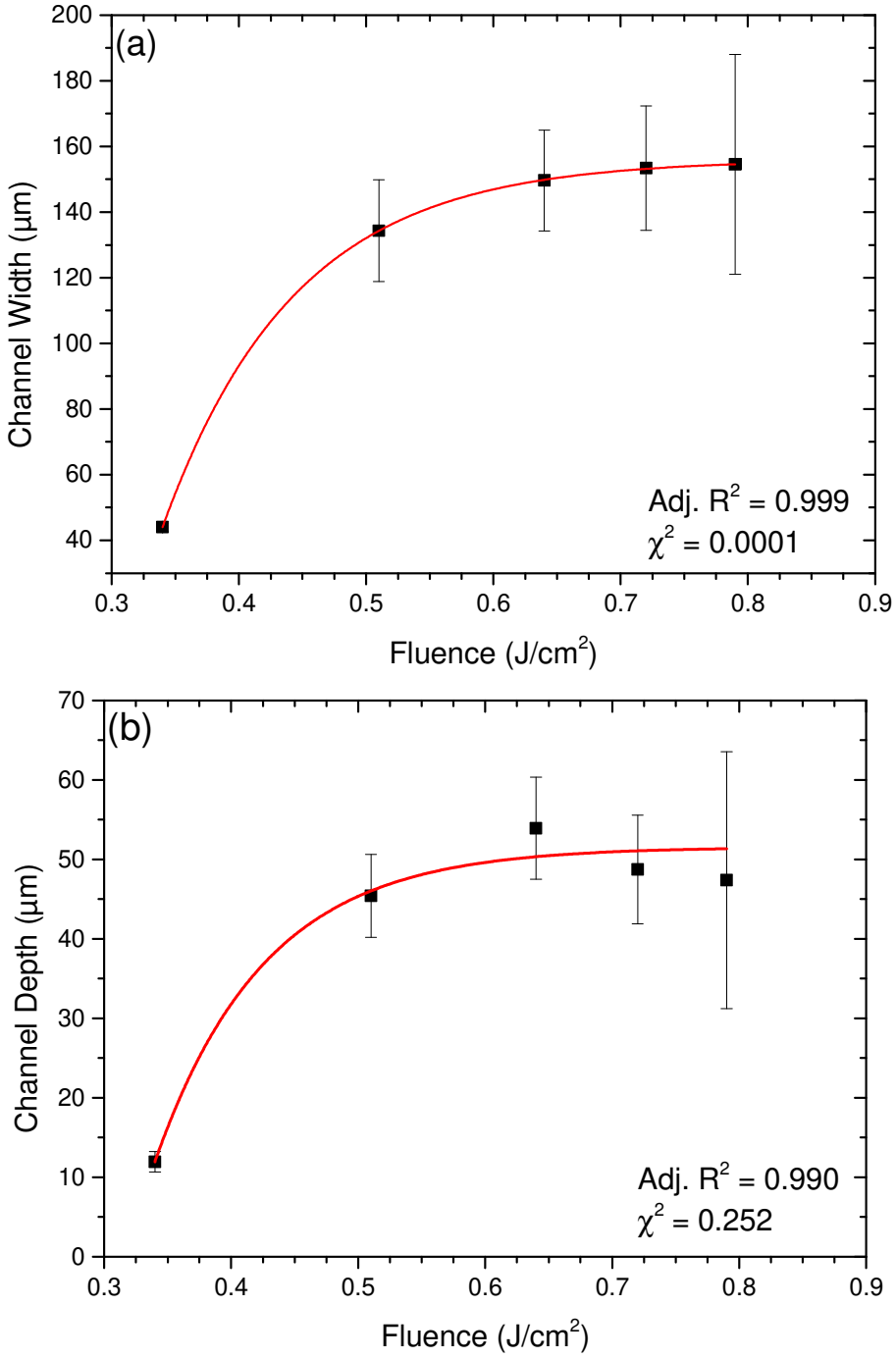

Figure 3.1: Measured microchannel (a) width and (b) depth as a function of laser fluence for a single laser pass. The error bars represent a 90% confidence interval.

Figure 3.2 shows 3D images of the microchannels taken using the optical profilometer. For the lower fluence pass (0.34 J/cm^2), a narrow and shallow V-shaped channel with condensed ablated material and melt around the channel edges was observed, see Figure 3.2a. A wider and deeper microchannel which contained

localised deeper ablation sites along the bottom of the channel resulted from the higher fluence pass (0.79 J/cm^2), see Figure 3.2b.

Both the width and depth data show increasing standard deviation with increasing fluence. The logarithmic fit applied on the depth vs. fluence data showed an adjusted R-Squared value of 0.990 suggesting a good fit, however the reduced Chi-Squared value was calculated at 0.252. Similarly, the logarithmic fit applied to the channel width showed a good Reduced R-Squared of 0.999, with a Reduced Chi-Squared of 0.0001.

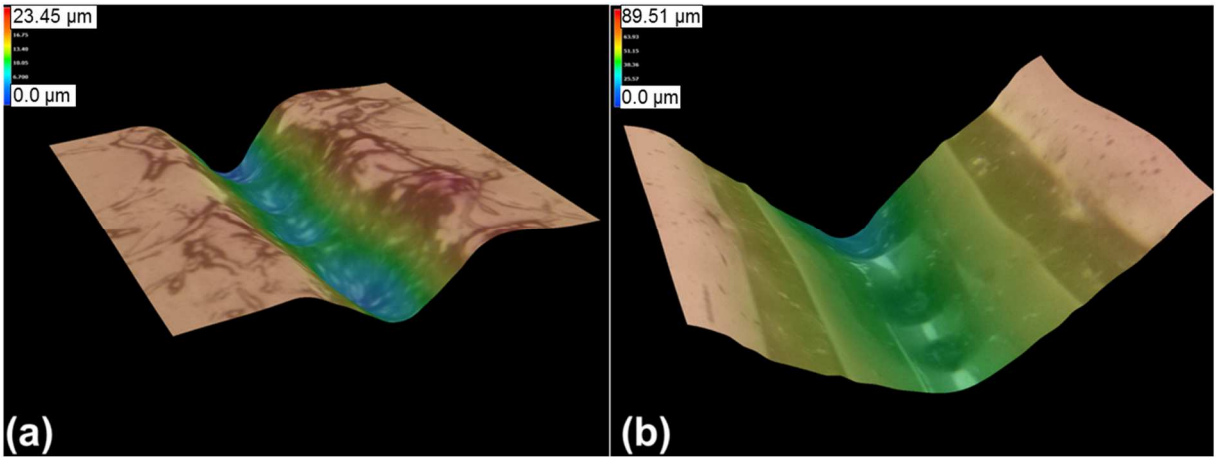

Figure 3.2: Optical profilometry images of microchannels produced from a single laser pass at a fluence (a) 0.34 J/cm^2 and (b) 0.79 J/ cm^2.

3.3.2 Ablation Rate

The ablation rate, i.e. the amount of material removed per laser pulse, was calculated to allow for insight into the laser ablation process. Figure 3.3 compares the experimental ablation rates (Equation 3.2.2) and calculated ablation rates (Equation 3.2.3). The threshold fluence (0.32 J/cm^2) used in Equation 3.2.3, was estimated from the x-axis intercept in Figure 3.1b. The effective optical penetration depth, α^{-1}, was determined from the slope of the linear fit applied to Figure 3.1b plotted on a semi-log scale, and was found to be 160 nm. For the lowest fluence used (0.34 J/cm^2) the experimentally determined value for ablation rate of 14 nm/pulse was higher than

predicted from the theory. For all other values above 0.34 J/cm^2, the measured ablation rate was lower than predicted, and was seen to plateau at a rate between 52 - 62 nm/pulse.

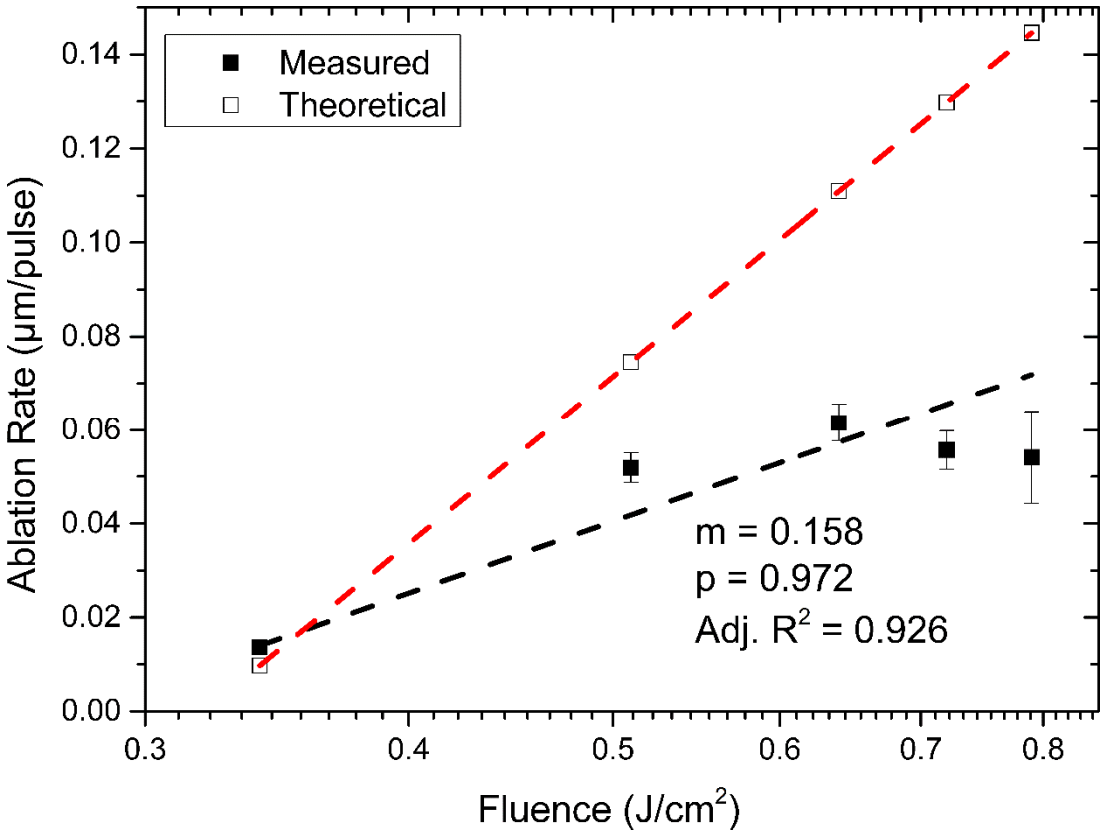

Figure 3.3: A comparison of the predicted and measured ablation rates for various laser fluences.

3.3.3 Effect of multiple laser passes

As before, the effect of multiple laser passes was examined using 3D optical profilometry. Both microchannel width and depth increased with successive laser passes (shown in Figure 3.4a and 3.4b respectively). Microchannel width was seen to increase with suggestive laser passes, ranging from 59 ± 13 µm for 3 laser passes, to 155 ± 37 µm for 11 passes. The microchannel depth was also seen to increase with successive laser passes, from 22 ± 3 µm for 3 laser passes, up to 77 ± 20 µm for 11 laser passes. For microchannel depth, there was a noted decrease in channel reproducibility for seven or more passes along with substrate warping during processing. For seven and eleven passes, debris was evident along the channel walls and crests see Figure 3.5. This debris became more rounded for higher number of laser

passes. 3D profilometry (inset Figure 3.5) showed isolated deep ablation sites along the base of the microchannel similar to that of microchannels produced via high fluence single laser passes.

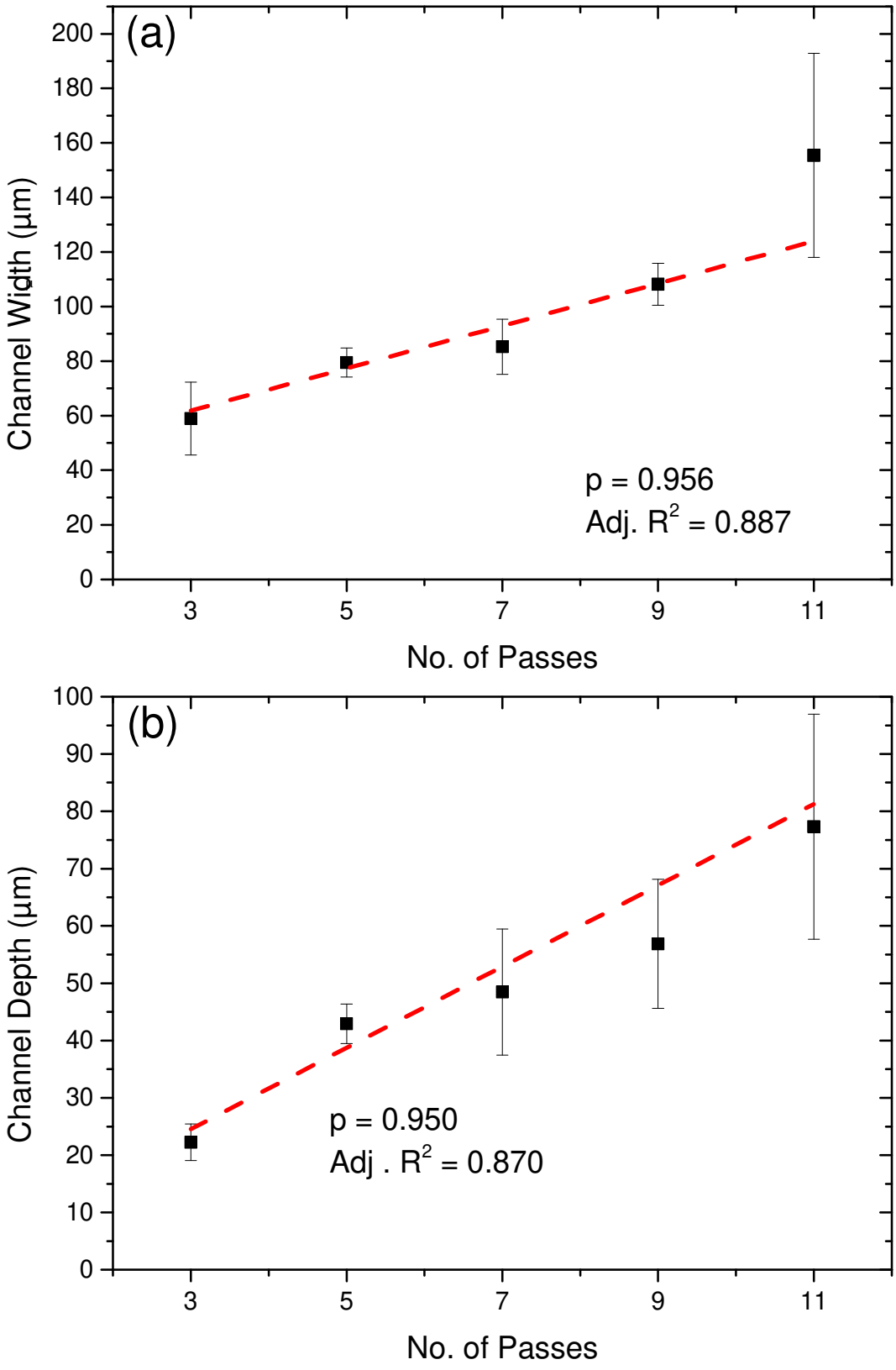

Figure 3.4: Measured microchannel (a) width and (b) depth as a function of number of laser passes. The error bars represent a 90% confidence interval.

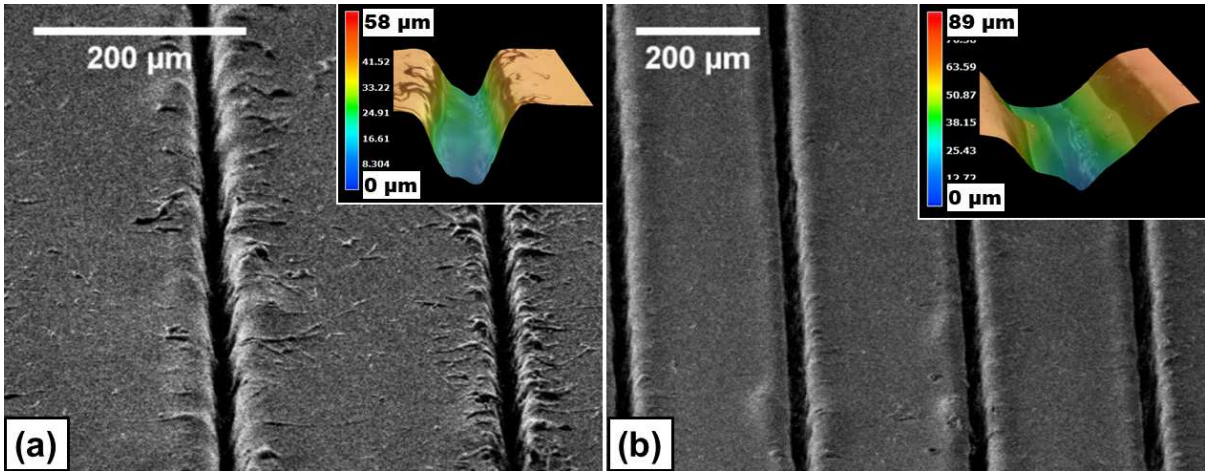

Figure 3.5: Scanning electron microscopy images of the COP substrate after (a) 7 and (b) 11 laser passes and corresponding 3D profiles (inset).

3.3.4 Surface Analysis

Raman and ATR-FTIR spectroscopy were performed to study the surface chemical composition after laser processing. Using Raman spectroscopy, the base of the microchannel was examined for changes, while the measurements from the interchannel areas (which were not processed), were used as a reference, as shown in Figure 3.6a. As the ATR-FTIR aperture was larger than the microchannel widths, the COP was analysed before and after laser processing. Both Raman and FTIR (Figure 3.6b and Figure 3.7) showed no significant differences in peak position for both the channel and interchannel areas. FTIR spectroscopy revealed oxidation after laser processing as evidenced by an increase in IR absorbance at the 1650 – 1750 cm^{-1} range. Dehydrogenation was also evident through a reduction in C-H absorbance at 2800 – 2950 cm^{-1}. The appearance of a broad band at 3100 – 3600 cm^{-1} was also observed which has been previously attributed to dehydrogenation causing the formation of C=C-H stretching in laser ablated COP [24].

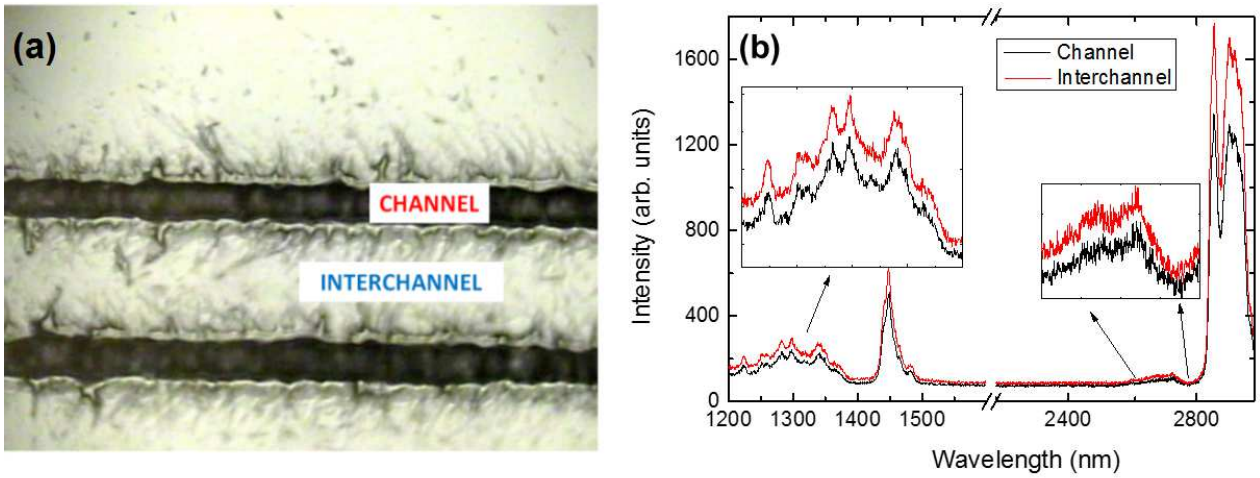

Figure 3.6: Optical image (a) and micro-Raman spectra (b) of the laser processed COP substrates.

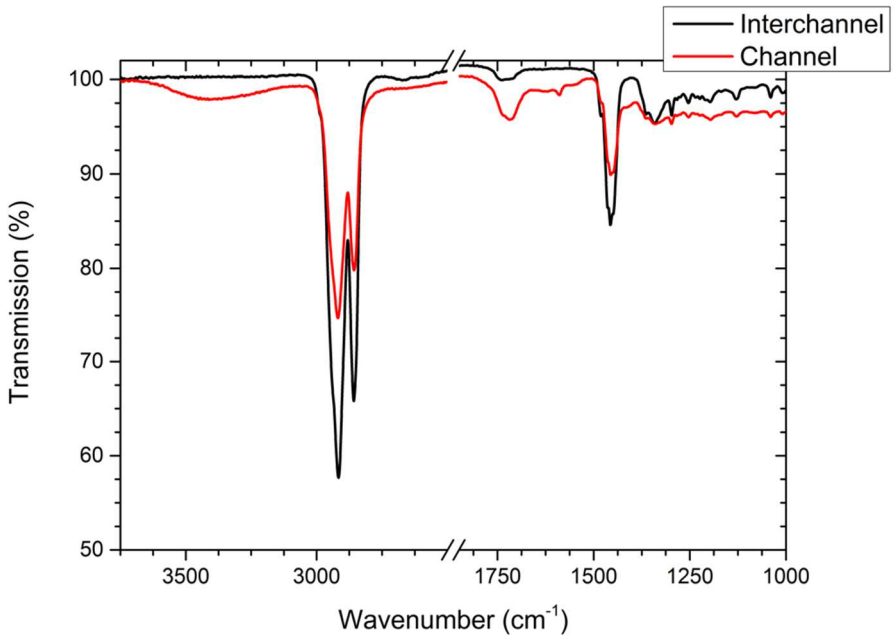

Figure 3.7: ATR-FTIR spectra of the COP substrate before and after laser processing.

3.4 Discussion

For the microchannels formed from a single laser pass, a logarithmic increase of both channel depth and width with increased fluence was seen. This is a reflection the underlying absorption mechanism which itself is logarithmically dependent on the ratio between the incident and transmitted laser intensities.

In terms of the applied logarithmic fits to the data, Reduced Chi-Squares of less than unity suggest that either the applied fit is improperly fitting noise, or there is a large overestimation error inside the fit. The low Reduced Chi-Squared values for the fits applied to the depth and width datasets, and the increasing error of both datasets as a function of fluence, suggests that it is the influence of noise which resulted in the low Reduced Chi-Squared values. This indicates there are other factors affecting microchannel depth at increasing fluences such as energy adsorption and interruption of the laser beam via the chaotic formation of condensed ablated polymer.

The reduction in height of recast material seen around the ablation sites may be attributed to thermal diffusion from the ablation site causing a localised melting of condensed debris. The increased build-up of heat in the processed area at higher fluences would be expected to result in increased levels of damage. The repetitive and localised nature of the ablation at the base of the microchannels followed the pattern of the applied laser pulsing.

The ablation rate predicted from Equation 3.2.1 was higher than that predicted from Equation 3.2.3 for all fluences greater than 0.34 J/cm^2. Equation 3.2.1 is based on a theoretical calculation for a single, isolated ablation site. It has been previously discussed that the production of microchannels can result in ablation rates which are higher than expected theoretically due to ablated material being allowed to escape from the previously processed area [26].

Furthermore, as the ablation rate calculation does not incorporate the reduction in the threshold fluence caused by of the “incubation effect” (see section 3.2.4) some deviation from the theory is expected. This accounts for the higher measured ablation rates compared to those calculated seen in

Figure **3.3** for fluences below 0.35 J/cm^2. The lower than predicted ablation rate for a fluences greater than 0.35 J/cm^2 was attributed to absorption within the laser-generated ablation plume attenuating the laser pulse energy during processing. For this experiment, an ablation rate of 0.14 nm/pulse was seen at the lowest fluence, plateauing at between 52 – 62 nm/pulse. Ablation rates of approximately 60 – 170 nm/pulse using an ArF excimer laser [20] and approximately 20 – 70 nm/pulse using a KrF excimer [21] laser have been observed over a range of laser fluences.

One further factor that may further account for the lower than expected ablation rate is the change in substrate morphology during processing. Equation 3.2.1 approximates all ablation occurring on a flat substrate, with no transmission or scatting

of the applied radiation. As material is ablated and the microchannel begins to form, the morphology of the ablation site changes from planar to v-shaped. The channel will have larger surface area than a flat ablation side, and as such the fluence will reduce as the channel forms.

The use of multiple laser passes showed the ability to further extend channel dimension beyond that achievable via single pass ablation at similar fluences. It is also of note that for certain conditions, the channel reproducibility was increased over that achieved via single-pass ablation. Keeping the number of passes at or below five was optimal when looking for reproducibility in microchannel depth. Similarly, high reducibility in microchannel width was seen for up to nine laser passes. This can be exploited to allow for fine control over the microchannel morphology, beyond that of single laser passes, while having good repeatability in microchannel dimensions. This decrease in channel reproducibility above five passes was attributed to the build-up of heat during processing, visibly evident by the appearance of substrate warping, resulting in the substrate surface moving within the laser focal plane. As this warping was evident at both high fluences and high number of passes, this highlights the possible need for active cooling of the substrate during processing is needed when wishing to extend this technique beyond the process space examined here. Use of a thicker substrate, which would have a larger thermal mass, could also be an alternative to minimise this damage.

Though a reduction in bonds containing hydrogen and an increase in the carbon signal was detected via infrared spectroscopy, the mechanisms of degradation found were consistent with that reported for other work on COP [24,28]. This suggests that the structure of the polymer remains mostly intact, and the COP should remain resistant to polar solvents, acids and bases which will be required for the microchannels to be exploited in analytical applications.

3.5 Conclusions

This chapter presents the first investigation into laser-texturing of microchannels on cyclic olefin polymer using an industrial 1064 nm Nd:YAG laser. The ability to tailor microchannel depth and width by varying laser fluence was demonstrated. Microchannels between 44 ± 1 µm and 155 ± 34 µm in width and 12 ± 1 µm and 47 ± 16 µm in depth were obtained over the fluence range examined. The channels at all

fluences presented a V-shape profile. The experimental ablation rate was calculated based on the microchannel depth and the number of incident laser pulses, and was compared to that expected from theory with ablation rates ranging from a minimum of 14 nm/pulse up to a maximum of 62 nm/pulse observed.

The use of multiple laser passes for fine-tuning of microchannel morphology was also examined with channel depths ranging from 22 ± 3 µm to 77 ± 20 and channel widths from 59 ± 13 µm and 155 ± 37 µm found. For up to five repeat laser passes, acceptable reproducibility in channel dimensions was observed allowing increased control over channel depths and widths with acceptable reproducibility and microchannel depth of 43 ± 3 µm. However, a large decrease in reproducibility of the microchannel depths occurred for seven passes and above, though channel widths had acceptable reproducibility for up to nine passes. The ability to create microchannels of defined aspect ratio (and surface area) is of great significance for chromatographic and analytical applications where increased surface area, and thus increased analyte-substrate interaction, results in increased separation efficiencies [29,30]. Furthermore, both infrared and Raman spectroscopy revealed oxidation and dehydrogenation as expected from previously reported work on laser processing of cyclic olefin polymers.

This work has provided a method for quick, single-step and relatively low-cost fabrication of reproducible microchannels on optically transparent substrates that have applications in lab-on-a-chip and microfluidic devices. Towards the final aim of this thesis, this technique will be employed as the fabrication technique for polymer microchannel-based chromatographic platforms.

References

[1] Nunes PS, Ohlsson PD, Ordeig O, Kutter JP. Cyclic olefin polymers: Emerging materials for lab-on-a-chip applications. Microfluid Nanofluidics. 2010 Apr 7;9(2–3):145–61.

[2] Faure K, Albert M, Dugas V, Crétier G, Ferrigno R, Morin P, et al. Development of an acrylate monolith in a cyclo-olefin copolymer microfluidic device for chip electrochromatography separation. Electrophoresis. 2008 Dec;29(24):4948–55.

[3] Yang Y, Li C, Kameoka J, Lee KH, Craighead HG. A polymeric microchip with integrated tips and in situ polymerized monolith for electrospray mass

spectrometry. Lab Chip. 2005 Aug 18;5(8):869–76.

[4] Shi Y-W, Wang Y, Abe Y, Matsuura Y, Miyagi M, Uyama H, et al. Fabrication of cyclic olefin polymer (COP)-coated silver hollow glass waveguides for the infrared. In: Bogner MS, Charles ST, Grundfest WS, Harrington JA, Katzir A, Lome LS, et al., editors. Proceedings of SPIE. San Jose, CA., USA: Surgical-Assist Systems; 1998. p. 96–102.

[5] Inguva S, Vijayaraghavan RK, McGlynn E, Mosnier J-P. Highly transparent and reproducible nanocrystalline ZnO and AZO thin films grown by room temperature pulsed-laser deposition on flexible Zeonor plastic substrates. Mater Res Express. 2015 Sep 1;2(9):096401.

[6] Azouz A Ben, Murphy S, Karazi S, Vázquez M, Brabazon D. Fast Fabrication Process of Microfluidic Devices Based on Cyclic Olefin Copolymer. Mater Manuf Process. 2014 Feb;29(2):93–9.

[7] Chen P-C, Pan C-W, Lee W-C, Li K-M. An experimental study of micromilling parameters to manufacture microchannels on a PMMA substrate. Int J Adv Manuf Technol. 2014 Jan 16;71(9–12):1623–30.

[8] Turri S, Levi M, Emilitri E, Suriano R, Bongiovanni R. Direct Photopolymerisation of PEG-Methacrylate Oligomers for an Easy Prototyping of Microfluidic Structures. Macromol Chem Phys. 2010 Apr 15;211(8):879–87.

[9] Zhang X, Jiang X., Sun C. Micro-stereolithography of polymeric and ceramic microstructures. Sensors Actuators A Phys. 1999 Oct;77(2):149–56.

[10] Shallan AI, Smejkal P, Corban M, Guijt RM, Breadmore MC. Cost-effective three-dimensional printing of visibly transparent microchips within minutes. Anal Chem. 2014 Mar 18;86(6):3124–30.

[11] Jena RK, Yue CY, Lam YC. Micro fabrication of cyclic olefin copolymer (COC) based microfluidic devices. Microsyst Technol. 2011 Oct 18;18(2):159–66.

[12] Matschuk M, Bruus H, Larsen NB. Nanostructures for all-polymer microfluidic systems. Microelectron Eng. 2010 May;87(5–8):1379–82.

[13] Cheng J-Y, Wei C-W, Hsu K-H, Young T-H. Direct-write laser micromachining and universal surface modification of PMMA for device development. Sensors Actuators B Chem. 2004 Apr;99(1):186–96.

[14] Lyutakov O, Tůma J, Huttel I, Prajzler V, Siegel J, Švorčík V. Polymer surface

patterning by laser scanning. Appl Phys B. 2013 Jan 9;110(4):539–49.

[15] Eaton SM, De Marco C, Martinez-Vazquez R, Ramponi R, Turri S, Cerullo G, et al. Femtosecond laser microstructuring for polymeric lab-on-chips. J Biophotonics. 2012 Aug;5(8–9):687–702.

[16] Baudach S, Bonse J, Krüger J, Kautek W, Kruger J. Ultrashort pulse laser ablation of polycarbonate and polymethylmethacrylate. Appl Surf Sci. 2000 Feb;154–155:555–60.

[17] Bagratashvili VN, Minaev N V., Rybaltovsky AA, Rybaltovsky AO, Tsypina SI, Panchenko VY, et al. Laser fabrication of periodic microstructures from silver nanoparticles in polymer films. Laser Phys. 2010 Jan 23;20(1):139–43.

[18] Prakash S, Acherjee B, Kuar AS, Mitra S. An experimental investigation on Nd:YAG laser microchanneling on polymethyl methacrylate submerged in water. Proc Inst Mech Eng Part B J Eng Manuf. 2013 Apr 7;227(4):508–19.

[19] Chen Y-T, Naessens K, Baets R, Liao Y-S, Tseng AA. Ablation of Transparent Materials Using Excimer Lasers for Photonic Applications. Opt Rev. 2005 Nov;12(6):427–41.

[20] Sabbert D, Landsiedel J, Bauer H-D, Ehrfeld W. ArF-excimer laser ablation experiments on Cycloolefin Copolymer (COC). Appl Surf Sci. 1999 Aug;150(1–4):185–9.

[21] Leech PW. Effect of norbornene content on laser ablation of cyclic olefin copolymers. Mater Des. 2010 Dec;31(10):4858–61.

[22] Inam Ul Ahad, Bartnik A, Fiedorowicz H, Kostecki J, Korczyc B, Ciach T, et al. Surface modification of polymers for biocompatibility via exposure to extreme ultraviolet radiation. J Biomed Mater Res A. 2014 Sep 25;102(9):3298–310.

[23] Bartnik A, Fiedorowicz H, Jarocki R, Kostecki J, Szczurek M, Chernyayeva O, et al. EUV-induced physico-chemical changes in near-surface layers of polymers. J Electron Spectros Relat Phenomena. 2011 Apr;184(3–6):270–5.

[24] Suriano R, Kuznetsov A, Eaton SM, Kiyan R, Cerullo G, Osellame R, et al. Femtosecond laser ablation of polymeric substrates for the fabrication of microfluidic channels. Appl Surf Sci. 2011 May;257(14):6243–50.

[25] Loebich O. The optical properties of gold. Gold Bull. 1972 Mar;5(1):2–10.

[26] Rodríguez A, Arriola A, Tavera T, Pérez N, Olaizola SM. Enhanced depth control of ultrafast laser micromachining of microchannels in soda-lime glass.

Microelectron Eng. 2012 Oct;98:672–5.

[27] Ben-Yakar A, Byer RL. Femtosecond laser ablation properties of borosilicate glass. J Appl Phys. 2004;96(9):5316.

[28] Liu C, Yu J, Sun X, Zhang J, He J. Thermal degradation studies of cyclic olefin copolymers. Polym Degrad Stab. 2003 Jan;81(2):197–205.

[29] Svec F. Quest for organic polymer-based monolithic columns affording enhanced efficiency in high performance liquid chromatography separations of small molecules in isocratic mode. J Chromatogr A. 2011;1228:250–62.

[30] Maya F, Svec F. A new approach to the preparation of large surface area poly(styrene-co-divinylbenzene) monoliths via knitting of loose chains using external crosslinkers and application of these monolithic columns for separation of small molecules. Polymer (Guildf). 2014 Jan 14;55(1):340–6.

Chapter 4

Taguchi method modelling of Nd:YAG laser ablation of microchannels on cyclic olefin polymer films

Publication Status: Published

Ronán McCann, Komal Bagga, Gabriel Duaux, Apryll Stalcup, Mercedes Vázquez, Dermot Brabazon. Taguchi method modelling of Nd:YAG laser ablation of microchannels on cyclic olefin polymer films. Opt Lasers Technol 2018;106:265-271. DOI: 10.1016/j.optlastec.2018.04.011

Abstract

This chapter presents the development of a model for Nd:YAG laser ablation of cyclic olefin polymer (COP) films. Two Taguchi orthogonal array experimental designs were implemented to produce a model for the prediction of microchannel depth and width produced on ZeonorFilm® ZF14 and ZF16 polymer films via laser ablation.

The width and depth of the produced microchannels were measured using 3D optical profilometry. Microchannels produced were seen to range in depths up to 50 µm, and widths up to 112 µm via single-pass ablation. Feature size was found to be dependent on the grade of COP and as expected, increasing feature size was found as the number of laser passes increased. The models are discussed in terms of adjusted coefficient of determination, signal to noise ratio and model significance. The effect of the process parameters such as fluence and scan speed on three different grades of COP were examined with an aim to produce a simple model suitable for predictive control of the surface microstructuring of COP and the production of microchannel-based UTLC platforms via laser ablation.

4.1 Introduction

Chapter 3 presented the first investigation into laser ablation of COP with an industrial Nd:YAG laser. The chapter also demonstrated the novelty of the process for microstructure and microchannel fabrication on COP. To fully exploit this new method for microstructure fabrication, it is imperative to fully understand and optimise the process. Though the parameters chosen in Chapter 3 allowed for investigation into channel morphology and changes in surface chemistry, these parameters were not optimised for idealised microchannel morphology or processing time. Therefore, to fully examine the capabilities of the laser processing system for the fabrication of microchannels on COP, and thus the microchannels themselves, a larger process space must be examined.

One approach used in both industrial and research environments is an experimental methodology known as Design of Experiments (DoE). More specifically, a DoE approach known as the Taguchi Method can be used to reduce the number of experiments needed to map the entire process and allow for swift optimisation. Previously, Taguchi method modelling has been used for the optimisation of laser processes such as laser welding [1–3] and laser microdrilling [4] for both metals and polymers.

In this chapter, we present an investigation into laser ablation of two grades of ZeonorFilm® ZF14 and ZF16 COP using the same 1064 nm laser system as described in Chapter 3. The effect of parameters such as laser fluence, beam scan speed and number of passes on the depth and width of the produced microchannels was examined using a Taguchi orthogonal array Design of Experiments (DoE). The data collected from the Taguchi array was then used to develop a model for the laser ablation of two grades and three thicknesses of COP with an aim to develop a simple protocol suitable for model predictive control for the laser machining of COP and the fabrication of microchannel-based UTLC platforms.

4.2 Methods and Materials

4.2.1 Experimental Setup and Characterisation

The laser system setup is the same as described in Section 3.2.2. The laser fluence for this work was calculated using the laser beam waist and the average power output, as measured using an A-10-D12-HPB-USB Laser Power Meter (Laserpoint, Italy). The laser power could be varied from 0 W to a maximum of 1.200 W ± 0.5 mW at a pulse repetition rate of 10 kHz. The beam waist was fixed at 140.0 ± 0.05 µm for this work, and was measured using a WinCamD-LCM2 CMOS laser beam profiler (Dataray, USA).

The microchannel morphology was examined using a VHX-2000 3-dimensional optical profilometer (Keyence, Japan) scanning upwards from the base of the channel in 1 µm increments. The average measurement of 16 channel profiles (four profiles across four channels) per sample at a 500x magnification were recorded where the channels were examined for two parameters: depth (defined as the length from the base of the channel to the mean height of the channel crests) and full-width half-max (FWHM, defined as the width of the channel measured at half the depth of the channel).

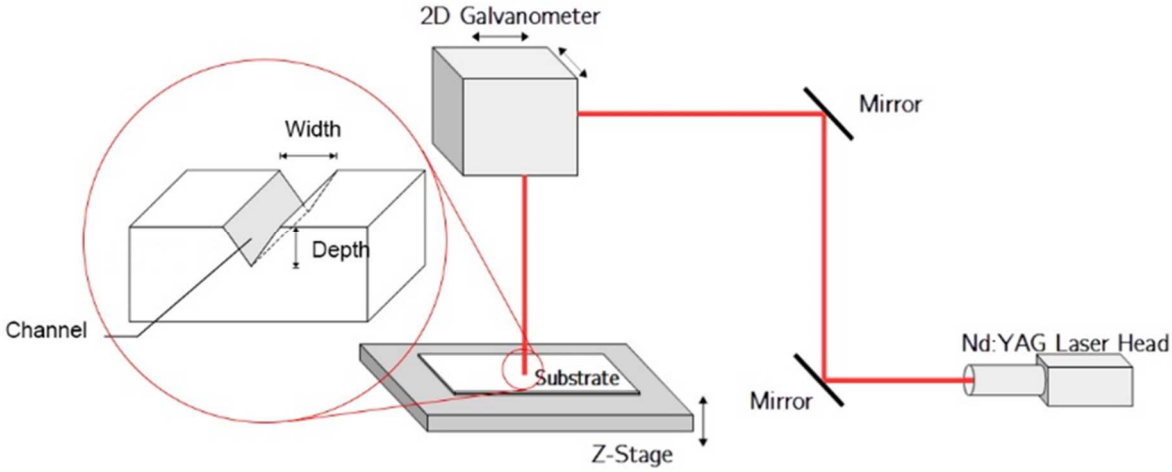

Figure 4.1: Schematic of the 1064 nm laser ablation setup and responses measured.

4.2.2 Materials

The substrates used in this experiment were ZeonorFilm® ZF14-188, ZF16-100 and ZF16-250 cyclic olefin polymer (Zeon Chemical LP, Japan) with film thicknesses of 188 µm, 100 µm and 250 µm respectively. Material properties of note are listed in Table 4.1.

Table 4.1: Properties of ZeonorFilm® ZF14 and ZF16 grades of cyclic olefin polymer [5].

Property	ZF14	ZF16
Water Absorption[3] (%)	<0.01	<0.01
Glass Transition Temperature (°C)[4]	136	163
Refractive Index	1.53	1.53
Birefringence (nm)	3	3

[3] As defined via ISO 62:2008 and ASTM D570 – 98(2010)e1 (Standard Test Method for Water Absorption of Plastics).

[4] The Glass Transition Temperature (T_g) is the point at which the viscosity, heat capacity and thermal expansion of a polymer or glass begins to increase.

4.2.3 Taguchi Orthogonal Array

The experimental design chosen for the study of laser ablation of ZF14 was a Taguchi orthogonal array L_{16} (with three factors at four levels, outlined in Table 4.2) and was produced and analysed using the Design-Expert 7 (Stat-Ease Inc., USA) and Minitab 17 (Minitab Inc., USA) software packages. The minimum fluence level of the design was chosen to be above the threshold fluence for ablation. Previous work by our group determined a threshold fluence for ZF14-188 of 0.32 J/cm^2 for a single laser pass and a beam scan speed of 1.2 mm/s [6]. A reduced quadratic model was developed using a backwards elimination to remove insignificant terms and increase model simplicity while maximising the adjusted coefficient of determination.

Table 4.2: Process parameters and design levels used. The thickness parameter was excluded from the ZF14 model.

Factors	Symbol	Unit	Level 1	Level 2	Level 3	Level 4
Fluence	F	J.cm^{-2}	0.652	0.785	0.896	0.983
Scan Speed	ν	mm.s^{-1}	1.8	2.5	3	3.5
Number of passes	N	unitless	1	2	3	4
Thickness	d	µm	100	250	-	-

Similarly, for the ZF16 ablation study, an L_{32} matrix ($2^1 + 4^9$) was used by coupling two L_{16} matrices using the same levels as before with a fourth factor, film thickness, added to the experimental design with two levels. A reduced quadratic model was developed for the ZF16 ablations with a backwards elimination applied as before. The full orthogonal arrays for the ZF14 and ZF16 models are listed in Table 4.3 and 4 respectively.

Table 4.3: Experimental factors of the Taguchi matrix L_{16} (4^5) used for the modelling ZF14 – 188 µm ZeonorFilm® ablation.

Sample	Fluence (J/cm^2)	Scan Speed (mm/s)	Number of Passes
1	0.652	1.8	1
2	0.652	2.5	2
3	0.652	3	3
4	0.652	3.5	4
5	0.785	1.8	2
6	0.785	2.5	1
7	0.785	3	4
8	0.785	3.5	3
9	0.896	1.8	3
10	0.896	2.5	4
11	0.896	3	1
12	0.896	3.5	2
13	0.983	1.8	4
14	0.983	2.5	3
15	0.983	3	2
16	0.983	3.5	1

Table 4.4: Experimental factors of the Taguchi matrix L_{32} ($2^1 + 4^9$) used for the ZF16 ZeonorFilm® ablation model.

Sample	Thickness (µm)	Fluence (J/cm^2)	Scan Speed (mm/s)	Number of Passes
1	100	0.652	1.8	1
2	100	0.652	2.5	2
3	100	0.652	3	3
4	100	0.652	3.5	4
5	100	0.785	1.8	2
6	100	0.785	2.5	1
7	100	0.785	3	4
8	100	0.785	3.5	3
9	100	0.896	1.8	3
10	100	0.896	2.5	4
11	100	0.896	3	1
12	100	0.896	3.5	2
13	100	0.983	1.8	4
14	100	0.983	2.5	3
15	100	0.983	3	2
16	100	0.983	3.5	1
17	250	0.652	1.8	1
18	250	0.652	2.5	2
19	250	0.652	3	3
20	250	0.652	3.5	4
21	250	0.785	1.8	2
22	250	0.785	2.5	1
23	250	0.785	3	4
24	250	0.785	3.5	3
25	250	0.896	1.8	3
26	250	0.896	2.5	4
27	250	0.896	3	1
28	250	0.896	3.5	2
29	250	0.983	1.8	4
30	250	0.983	2.5	3
31	250	0.983	3	2
32	250	0.983	3.5	1

4.3 Results

4.3.1 Microchannel Morphology

Figure 4.2 shows the typical microchannel morphologies produced via laser ablation as measured via 3D optical profilometry. Across all samples, the microchannels produced had a v-shaped morphology, which is consistent with previous work on infrared laser ablation of COP with deeper microchannels having a more pronounced V-shape. Along the base of the microchannels were isolated wells, which became less pronounced as the microchannels became deeper. This was attributed to the pulsed nature of the applied scanning beam of radiation. Outside the ablation site, condensed melt and debris was seen, again being more evident with deeper channels. For deeper microchannels, the debris was seen to be smoother, suggesting that melting occurred.

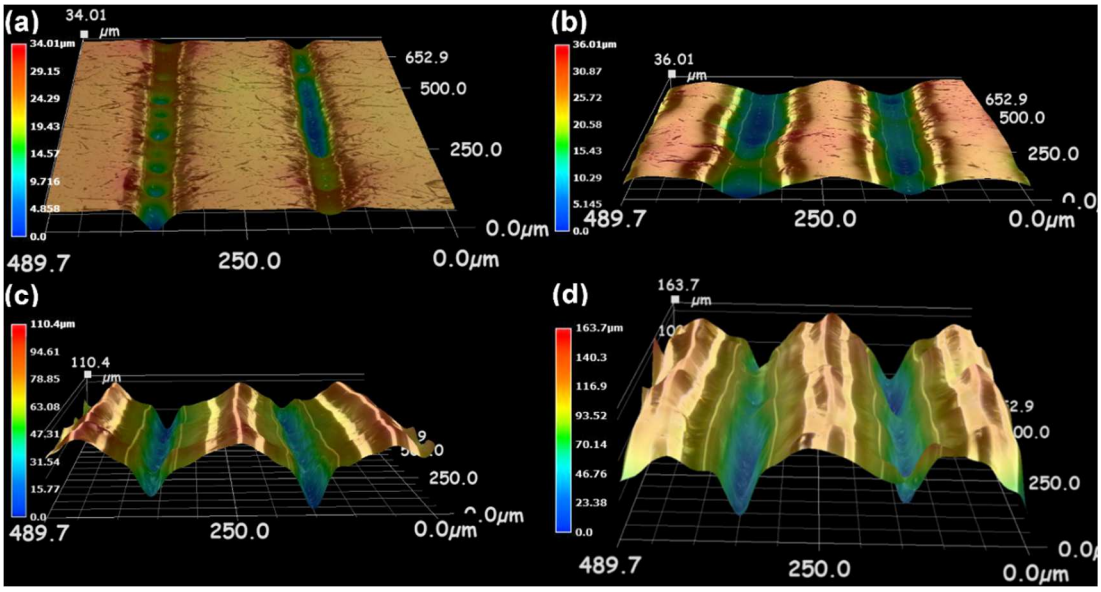

Figure 4.2: 3D Optical Profilometry images showing the formation of (a) 6 µm, (b) 25 µm and (c) 87 µm microchannels on ZF14-188 and (d) an 83 µm microchannel on ZF16-250.

4.3.2 Signal-to-Noise Analysis

To determine which factors had the greatest effect in the model, the signal-to-noise (S/N) ratio was calculated for the depth and FWHM profilometry measurements. Many analytical devices require microchannels with high surface area-to-volume ratios, for enhanced surface-chemical interaction or increased mass transfer for

example [7,8]. As these analytical applications are of particular interest in this study, a target for high aspect ratio channels (in this case, large depth and small width) was decided.

Equations 4.3.1 and 4.3.2 show the signal-to-noise ratio, S/N, definitions used for the FWHM and depth respectively. Two different S/N ratio measurements were used to assess the outcome of these experimental goals:

$$(\mathrm{S/N})_{FWHM} = -10\log_{10}\left(\sum \frac{\mathrm{w}^2}{\mathrm{n}}\right) \qquad \textbf{Eqn. 4.3.1}$$

and

$$(\mathrm{S/N})_{Depth} = -10\log_{10}\left(\sum \frac{\mathrm{y}^{-2}}{\mathrm{n}}\right) \qquad \textbf{Eqn. 4.3.2}$$

where y is the channel depth, w is the channel FWHM and n is the number of repetitions per design point, which in this study was four. The measurement used for the FWHM was chosen to minimize the S/N ratio (i.e. the-smaller-the-better). Conversely, the measurement for the depth was chosen to maximise the S/N ratio (i.e. the-larger-the-better).

Table 4.5 outlines the calculated S/N ratios for the ZF14 experimental design, ranked in order from highest to lowest delta (i.e. the difference between the maximum and minimum recorded response values). For the ZF14 ablations, fluence showed the largest delta for both depth and FWHM, suggesting it has the largest effect on the responses.

Table 4.5: Signal-to-noise ratio of microchannel depth (the-larger-the-better) and FWHM (the-smaller-the-better) over four levels for the ZF14 ablation study.

Response	Factor	Level				Delta	Rank
		1	2	3	4		
Depth	F	12.42	21.87	29.68	29.84	17.42	1
	ν	27.92	23.20	21.67	21.01	6.91	2
	N	21.31	21.80	25.63	25.06	4.32	3
FWHM	F	-29.80	-34.49	-36.85	-35.28	7.05	1
	ν	-33.63	-33.77	-34.17	-34.84	1.21	2
	N	-33.70	-34.12	-34.05	-34.56	0.86	3

From the ZF16 study, the additional design factor, film thickness, used in the ZF16 experimental design was found to be the second ranked factor (in terms of delta) affecting the produced microchannel depth, see Table 4.6. The effect of substrate thickness was however the lowest ranked factor affecting the FWHM S/N, suggesting it has the smallest effect of all experimental factors on the FWHM over the range studied.

Table 4.6: Signal-to-noise ratios of microchannel depth (the-larger-the-better) and FWHM (the-smaller-the-better) over four levels for the ZF16 study.

Response	Factor	Level				Delta	Rank
		1	2	3	4		
Depth	F	16.10	21.58	28.80	33.26	17.16	1
	ν	26.87	24.33	24.23	24.31	2.63	3
	N	24.44	24.49	25.85	24.96	1.41	4
	d	28.14	21.73	-	-	6.41	2
FWHM	F	-28.58	-30.77	-35.63	-37.63	9.05	1
	ν	-33.22	-32.50	-33.45	-33.44	0.95	3
	N	-32.31	-32.91	-33.90	-33.49	1.59	2
	d	-33.62	-32.69	-	-	0.93	4

4.3.3 ANOVA Analysis

Table 4.7 outlines the primary Analysis of Variance (ANOVA) parameters extracted from the depth and FWHM models. All models developed had an adjusted R-squared of greater than 0.83, and were all in close agreement (within 0.1) with the model predicted R-squared. The adequate precision (i.e. the full signal-to-noise ratio of the four responses) was large, indicating that error is not a significant contribution to the model. The F-value, which compares the parameter variance with the residual variance, was also large for all models again indicating strong model significance. Full ANOVA information for both models is listed in Tables 4.7 – 4.12 and definitions of the terminology used in the ANOVA tables is available in Appendix A.

Table 4.7: Summary of the ANOVA parameters for the four Taguchi models.

Response	Material	Degrees of Freedom	Adjusted R-Squared	Predicted R-Squared	Adequate Precision	F value
FWHM	ZF14	6	0.985	0.973	34.276	167.32
	ZF16	7	0.854	0.811	15.7	26.94
Depth	ZF14	4	0.947	0.911	25.1	67.35
	ZF16	7	0.828	0.770	16.3	22.25

Table 4.8: ANOVA of the depth response for the design of the ZF14–188 ZeonorFilm®.

Source	Sum of Squares	df	Mean Square	F Value	p-value (Prob > F)
Model	0.275614	4	0.068903	67.3542	< 0.0001 significant
F	0.02454	1	0.02454	23.98814	0.0005
N	0.025638	1	0.025638	25.06201	0.0004
FN	0.024814	1	0.024814	24.25653	0.0005
F^2	0.028973	1	0.028973	28.32147	0.0002
Residual	0.011253	11	0.001023		
Cor Total	0.286867	15			
R-Squared	0.960773		Pred R-Squared		0.911214
Adj R-Squared	0.946508		Adeq Precision		25.12639

Table 4.9: ANOVA of the FWHM response for the design of the ZF14–188 ZeonorFilm®.

Source	Sum of Squares	df	Mean Square	F Value	p-value (Prob > F)
Model	3330.642	5	666.1285	25.3565	< 0.0001 significant
F	744.6646	1	744.6646	28.34601	0.0003
ν	159.0075	1	159.0075	6.052696	0.0337
N	181.5339	1	181.5339	6.910175	0.0252
Fν	146.2114	1	146.2114	5.565608	0.0400
F^2	810.5034	1	810.5034	30.85219	0.0002
Residual	262.7053	10	26.27053		
Cor Total	3593.348	15			
R-Squared	0.926891		Pred R-Squared		0.816209
Adj R-Squared	0.890337		Adeq Precision		13.41669

Table 4.10: ANOVA of the depth response for the design of the ZF16–100 and ZF16-250 ZeonorFilm®.

Source	Sum of Squares	df	Mean Square	F Value	p-value (Prob > F)
Model	24.38372	7	3.483389	22.24774	< 0.0001 significant
d	0.500087	1	0.500087	3.193963	0.0865
F	18.24503	1	18.24503	116.5275	< 0.0001
ν	0.000985	1	0.000985	0.006291	0.9374
N	0.187634	1	0.187634	1.198384	0.2845
dF	0.719099	1	0.719099	4.592748	0.0425
dν	0.472094	1	0.472094	3.015172	0.0953
FN	0.17981	1	0.17981	1.148414	0.2945
Residual	3.757745	24	0.156573		
Cor Total	28.14147	31			
R-Squared	0.866469		Pred R-Squared		0.770109
Adj R-Squared	0.827523		Adeq Precision		16.3143

Table 4.11: ANOVA of the FWHM response for the design of the ZF16–100 and ZF16-250 ZeonorFilm®.

Source	Sum of Squares	df	Mean Square	F Value	p-value (Prob > F)
Model	0.033694	6	0.005616	27.22462	< 0.0001 significant
d	0.001231	1	0.001231	5.96651	0.0220
F	0.019155	1	0.019155	92.86301	< 0.0001
ν	0.001084	1	0.001084	5.257444	0.0305
dF	0.001157	1	0.001157	5.607571	0.0259
Fν	0.001065	1	0.001065	5.165116	0.0319
FN	0.001961	1	0.001961	9.504866	0.0049
Residual	0.005157	25	0.000206		
Cor Total	0.038851	31			
R-Squared	0.867267		Pred R-Squared		0.798998
Adj R-Squared	0.835411		Adeq Precision		15.13616

The equations derived from the Taguchi model were:

$$z_{ZF14} = (2.81 - 6.01F + 0.23N - 0.28FN + 3.54F^2)^{-0.5} \quad \textbf{Eqn. 4.3.3}$$

$$z_{ZF16} = \exp(1.60 - 0.01t + 1.05F + 0.44\nu - 0.70N + 0.02dF - 2.58 \times 10^{-3}t\nu + 0.89FN) \quad \textbf{Eqn. 4.3.4}$$

$$w_{ZF14} = (0.05 - 0.12F + 4.70 \times 10^{-3}\nu - 3.61 \times 10^{-4}N - 3.88 \times 10^{-3}F\nu + 0.07F^2 - 3.42 \times 10^{-4}\nu^2)^{0.68} \quad \textbf{Eqn. 4.3.5}$$

$$w_{ZF16} = (0.05 - 1.60 \times 10^{-4}d - 0.02F + 0.04\nu - 0.01N + 2.01 \times 10^{-4}dF - 0.04F\nu + 0.01FN)^{-1} \quad \textbf{Eqn. 4.3.6}$$

where z is microchannel depth (in µm), w is microchannel FWHM (µm), F is laser fluence (J/cm^2), N is number of laser passes and ν is laser beam scan speed (mm/s). The simplest model derived was for ZF-14 microchannel depth, with only 4 significant factors, and 4 degrees of freedom in the model (Equation 4.3.3). For ZF16

microchannel depth, the model was more complex with 4 factors and 7 degrees of freedom, and an exponential transformation applied, shown in Equation 4.3.4. This exponential behaviour of the model, coupled with fluence having the largest effect of all the process parameters, is an expected behaviour resulting from the *Beer-Lambert Law* whereby light absorption is exponential to the applied radiation intensity [6]. The microchannel FWHM models for ZF14 and ZF16 had 6 and 7 degrees of freedom, and 3 and 4 factors respectively (shown in Equations 4.3.5 and 4.3.6).

Non-linear factors in model equations, such as the F^2 term in Equation 3, are a measure of the saturation of the response as the factor increases [9]. From Equation 3, it was determined that a fluence of approximately 0.88 J/cm^2 was the optimal for processing of ZF14 grade COP, with a reduction in the measured depth response for fluences beyond 0.88 J/cm^2. Similarly, two non-linear factors, scan speed and fluence, were evident in the model for microchannel width on ZF14, as shown in Equation 5.

No other factors effecting the saturation of microchannel depth or width was evident for either the ZF14 or ZF16 grade polymers. This is due to limitations in the Taguchi method being optimised to accurately map the process space in a minimal number of experimental runs. As such, this limitation makes it difficult to extrapolate beyond the process space. It is possible that if the process space is extended beyond the maximum level chosen in this study, the saturation in microchannel depth will become evident for ablations on ZF16.

4.3.4 Microchannel Depth

The microchannel depth was analysed via optical profilometry and results for both the ZF14 and ZF16 models are shown in Figure 4.3 – 4.5. The ZF14-188 model predicted a maximum microchannel depth of 23 µm (Figure 4.3a), while depths of 50 µm and 36 µm (Figures 4.4a and 4.5a) were predicted for the ZF16-100 and ZF16-250 respectively. For four laser passes (the maximum trialled), increased microchannel depths were evident on all substrates. Maximum depths of up to 87 µm were predicted via the Taguchi model for ZF14 (Figure 4.3c). For ZF16-100 and ZF16-250, depths of 81 µm and 58 µm were found respectively (Figures 4.4c and 4.5c), similar to the ZF14 model. Smaller minima were predicted for the microchannel depths for multiple pass ablations when compared to the single pass.

4.3.5 Microchannel Full-Width Half-Maximum

As in Section 4.3.3, the microchannel FWHM was examined using optical profilometry, results of which are shown in Figures 4.3 – 4.5. For single pass laser ablation of ZF14-188, the model predicted maximum channel widths of 71 µm was found (Figure 4.3b). At both high and low scan speeds, the FWHM was seen not to scale linearly with fluence. This non-linearity is consistent with previous work in Chapter 3 which showed a logarithmic increase of microchannel width, though with decreasing reproducibility [6]. The model predicted microchannel width was also seen to be highly dependent on scan speed, with higher scan speeds resulting in wider channels. This suggested that plume occlusion was also an important mechanism at slower scan speeds, with the plume opacity inversely proportional to scan speed.

The ZF16 model predicted a maximum of 112 µm and 69 µm for ZF16-100 and ZF16-250 respectively, as shown in Figure 4.4b and 4.5d respectively. The discrepancy in FWHM between the two thicknesses was attributed to the thicker substrate having a larger thermal mass, thus maintaining a higher ablation threshold during processing as a result of a decreased incubation effect. Maximum microchannel widths of 124 µm were seen for four laser passes on ZF14 (Figure 4.3d), which was higher than that previously reported for 1064 nm laser ablation of that grade of COP [6].

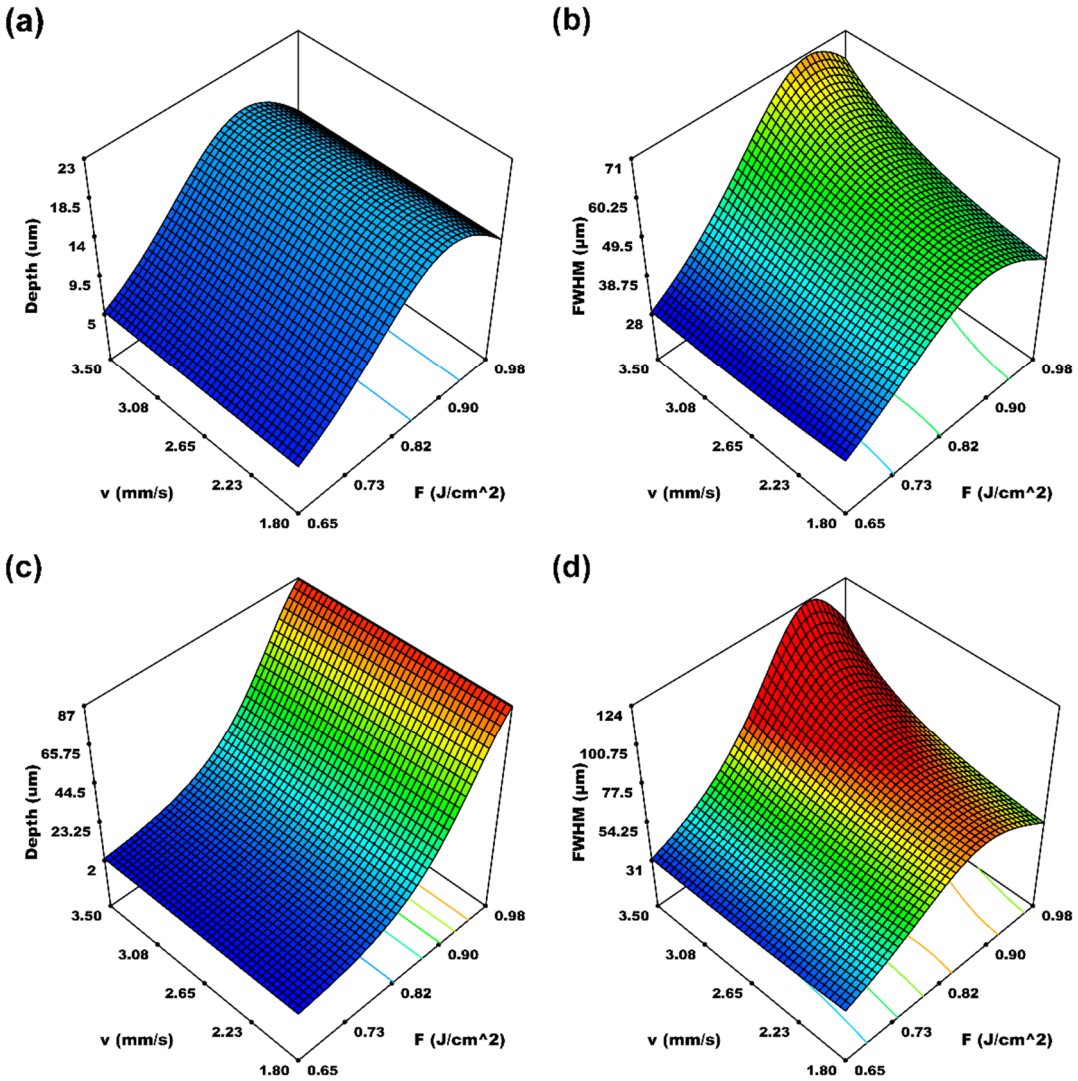

Figure 4.3: Surface plots of the modelled effect of fluence and scan speed on the microchannel depth and FWHM responses on ZF14-188 for one laser pass (a-b) and four laser passes (c-d).

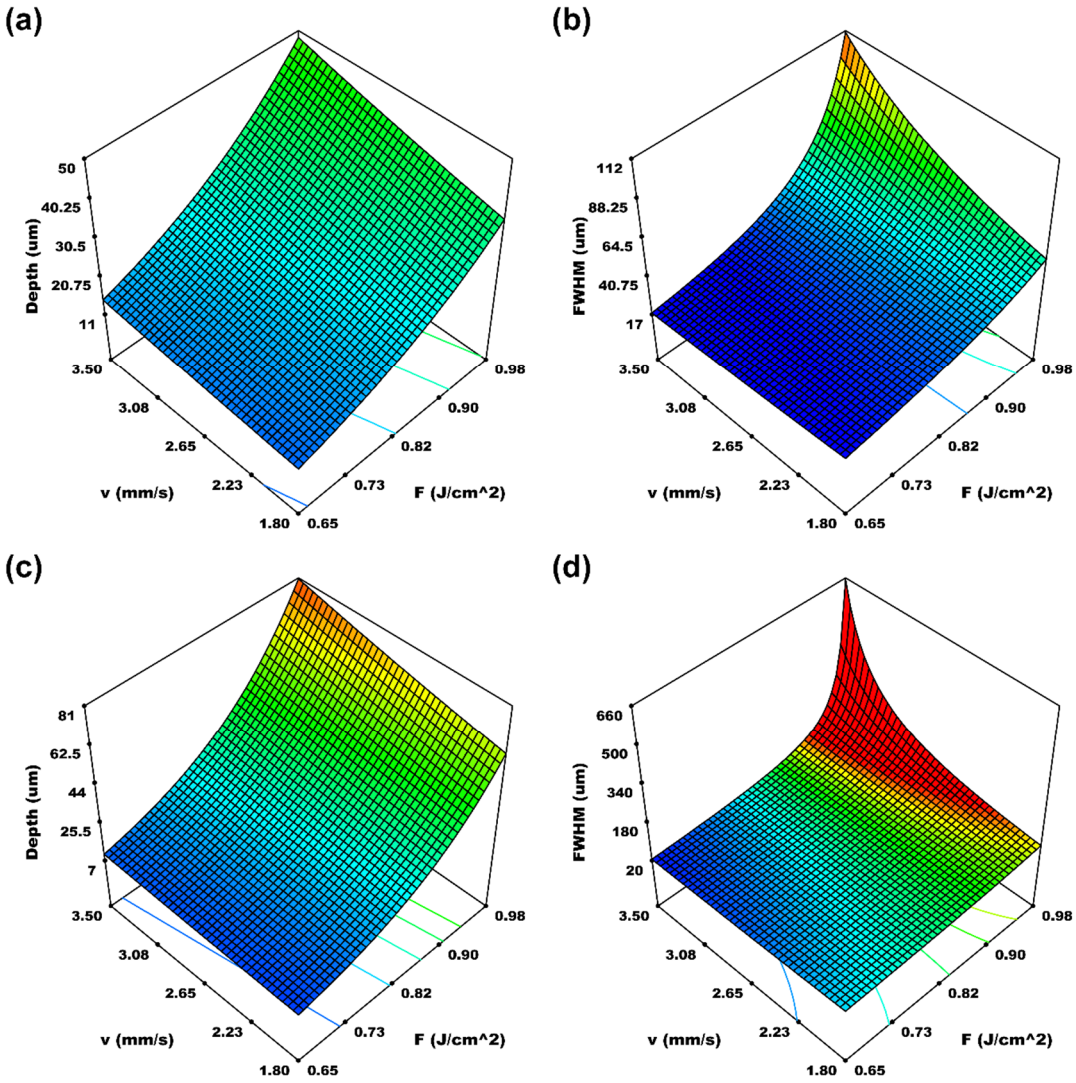

Figure 4.4: Surface plots of the modelled effect of fluence and scan speed on the microchannel depth and FWHM responses on ZF16-100 for one laser pass (a-b) and four laser passes (c-d).

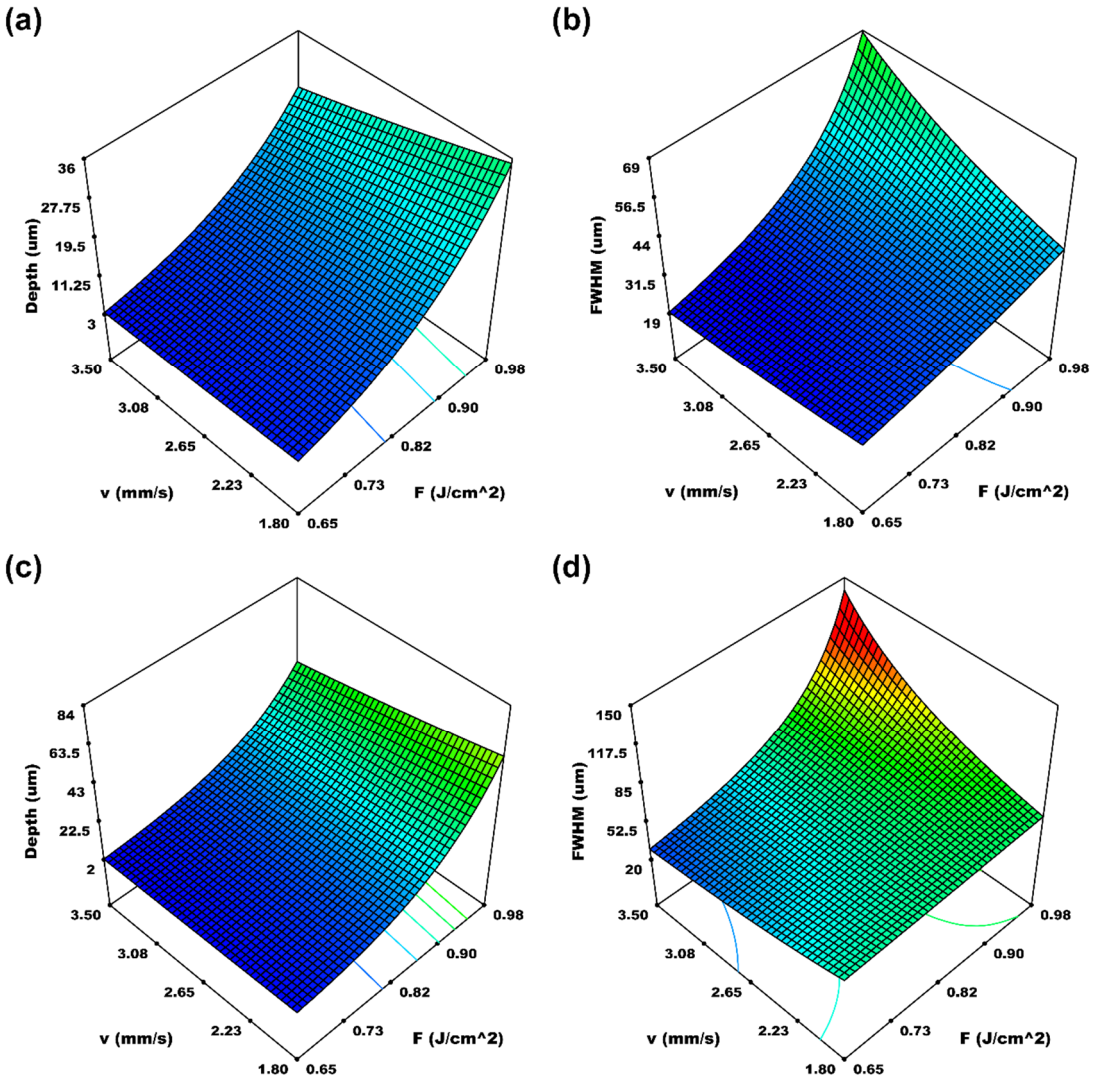

Figure 4.5: Surface plots of the modelled effect of fluence and scan speed on the microchannel depth and FWHM responses on ZF16-250 for one laser pass (a-b) and four laser passes (c-d).

4.4 Discussion

The non-linearity of the depth response to fluence is consistent to that previously reported for 1064 nm laser ablation of ZF14-188, which was attributed to plume occlusion, whereby the ablation plume becomes opaque at the laser wavelength thus reducing fluence at the ablation site [6].

Ablation on the ZF16 polymers revealed a positive linear correlation between both fluence and number of passes, and microchannel depth over the range modelled. This was partly attributed both to ZF16 having a higher glass transition temperature (T_g) than ZF14 [5] and the differing substrate thicknesses. Previous studies have shown an inverse relationship between laser ablation rate, R, and the glass transition temperature of polymers, however other material properties such as the melting enthalpy and heat capacity also play a significant role [10]. As the ablation mechanism is photothermal in nature for the laser parameters used in this study, these properties may also result in differing sizes of the heat affected zone. A larger heat affected zone would result in increased melt and macro-particulates ejected from the ablation site, thus compounding the occlusion of the substrate surface by the ablation plume during processing.

The difference between the maximum predicted depth of channels on the ZF16-100 and ZF16-250 could be attributed to the thicker substrate having a larger thermal mass limiting the "incubation effect" as described in Chapter 3 and in the literature [11]. The incubation effect can lead to lower ablation threshold values as a function of number of laser shots as the substrate builds up heat during processing. The linearity of the depth response with both fluence, beam scan speed and number of passes suggests that plume occlusion is not a significant effect for ZF16 within the examined process space.

For ZF14 ablations, a higher maximum microchannel FWHM was found than previously in Chapter 3, though the process conditions and channel measurements differed slightly in the two studies. The non-linear relationship between FWHM and the processing parameters, again most likely due to plume occlusion, suggested an optimal processing conditions are possible for maximising microchannel width. Previous studies on 1064 nm laser ablation of ZF14 have seen melting and warping of the substrate for high numbers of passes. Again, this discrepancy was attributed to the thicker substrate having a larger thermal mass, thus maintaining a lower working

temperature and thus a lower ablation threshold during processing. The large maximum value modelled on ZF16-100 suggested that the model was at the edge of the usable process space for the material prior to melting or warping occurring.

4.5 Conclusions

In conclusion, this chapter presents the first model developed for the laser ablation of two different grades of ZeonorFilm® COP. It was demonstrated that using an industrial Nd:YAG laser, it is possible to finely control the machining of microchannels on the surface of COP, with differing responses for different grades of COP. The primary factor effecting the microchannel depth and FWHM on both ZF14 and ZF16 was the laser fluence, Interestingly, the model developed for laser structuring of ZF16 showed that substrate thickness was the second most significant factor effecting the depth and FWHM responses. When comparing two thickness of the ZF16 polymer, the thermal bulk of the two thicknesses was attributed to be a primary reason for different responses of the two materials. This differing thermal bulk would result in different rates in heat accumulation and the working temperature during processing. Some limitations of the Taguchi model were seen when examining the edge of, and when extrapolating beyond, the process space. Ultimately, the developed model presented allows for the use of laser ablation for the fabrication of microchannel-based UTLC platforms but may also prove useful towards the implementation of predictive control of surface structuring of ZeonorFilm® COP via laser ablation over the process space examined.

References

[1] Anawa EM, Olabi AG. Using Taguchi method to optimize welding pool of dissimilar laser-welded components. Opt Laser Technol. 2008 Mar;40(2):379–88.

[2] Acherjee B, Kuar AS, Mitra S, Misra D. Application of grey-based Taguchi method for simultaneous optimization of multiple quality characteristics in laser transmission welding process of thermoplastics. Int J Adv Manuf Technol. 2011 Oct 26;56(9–12):995–1006.

[3] Xiansheng N, Zhenggan Z, Xiongwei W, Luming L. The use of Taguchi method to optimize the laser welding of sealing neuro-stimulator. Opt Lasers

Eng. 2011 Mar 1;49(3):297–304.

[4] Canel T, Kaya AU, Çelik B. Parameter optimization of nanosecond laser for microdrilling on PVC by Taguchi method. Opt Laser Technol. 2012 Nov 1;44(8):2347–53.

[5] ZeonorFilm® isotropic optical film properties [Internet]. Zeon Corporation [Internet]. 2017 [cited 2017 Jun 1]. p. Available from: Available from: http://www.zeon.co.jp

[6] McCann R, Bagga K, Groarke R, Stalcup A, Vázquez M, Brabazon D. Microchannel fabrication on cyclic olefin polymer substrates via 1064 nm Nd:YAG laser ablation. Appl Surf Sci. 2016 Nov;387:603–8.

[7] Hansson J, Yasuga H, Haraldsson T, van der Wijngaart W. Synthetic microfluidic paper: high surface area and high porosity polymer micropillar arrays. Lab Chip. 2016;16(2):298–304.

[8] Dong Z, Yao C, Zhang Y, Chen G, Yuan Q, Xu J. Hydrodynamics and mass transfer of oscillating gas-liquid flow in ultrasonic microreactors. AIChE J. 2016 Apr;62(4):1294–307.

[9] Savriama G, Baillet F, Barreau L, Boulmer-Leborgne C, Semmar N. Optimization of diode pumped solid state ultraviolet laser dicing of silicon carbide chips using design of experiment methodology. J Laser Appl. 2015 Aug;27(3):032009.

[10] Pham D, Tonge L, Cao J, Wright J, Papiernik M, Harvey E, et al. Effects of polymer properties on laser ablation behaviour. Smart Mater Struct. 2002 Oct 1;11(5):668–74.

[11] Ben-Yakar A, Byer RL. Femtosecond laser ablation properties of borosilicate glass. J Appl Phys. 2004;96(9):5316.

Chapter 5

Pulsed laser deposition of plasmonic nanostructured gold on flexible transparent polymer in air

Publication Status: Published

McCann R, Hughes C, Bagga K, Stalcup A, Vázquez M, Brabazon D. Pulsed laser deposition of plasmonic nanostructured gold on flexible transparent polymers at atmospheric pressure. J Phys D 2017;50(24).

DOI: 10.1088/1361-6463/aa7193

Abstract

In this chapter, a novel technique for the deposition of nanostructured thin films utilizing a modified form of pulsed laser deposition (PLD) is presented. This is called Confined Atmospheric PLD (CAP) and is presented here for the deposition of gold on cyclic olefin polymer substrates. The deposition process is a modified form of conventional PLD, with the deposition conducted under atmospheric conditions and with the substrate and target in close proximity. It was found that this confinement results in the deposition of nanostructured thin films on the substrate. Infrared spectroscopy showed no significant change of polymer surface chemistry as a result of the deposition process, and optical spectroscopy revealed plasmonic behaviour of the resulting thin film. The effect of laser fluence on the deposition process was also examined with more uniform films found to be deposited at higher fluences.

5.1 Introduction

Nanomaterial and nanostructured thin films have become of increasing interest in recent years. However, one roadblock to their full-scale adoption is the ability to deposit these nanomaterials on large area substrates. In addition to conventional deposition techniques such as plasma-enhanced chemical vapour deposition (PE-CVD) [1] and spray coating [2], pulsed laser deposition (PLD) has demonstrated promising potential for nanomaterial deposition, though the potential for scalability has yet to be fully explored.

PLD is a mature technique for the creation of nanostructured thin and ultrathin films [3,4] with control of parameters such as plasma density and electron temperature during deposition having a large influence over the characteristics of resultant deposited material [5]. This control can be achieved through laser parameters such as fluence [5], wavelength [6–8] or pulse repetition frequency [9], or through process parameters such as target-to-substrate distance [10] or background gas pressure [11]. When conducted in a vacuum or low-pressure background gas, stoichiometric transfer of material from the target to the substrate occurs forming a solid film upon deposition.

Ablation using an ultrashort femtosecond (fs) pulsed laser irradiation can generate nanoparticles within the plume, with the mechanism of nanoparticle formation being fragmentation and decomposition of the target material due to rapid heating [12]. The ultrafast nature of fs laser ablation produces a cooler and less dense plasma due to reduced laser-plume interaction when compared to picosecond or nanosecond ablation [13]. Plume velocities are also much greater in fs ablations resulting in the ability to deposit material prior to in-plume aggregation occurring [13].

The use of fs ablation has also been exploited via Laser-Induced Forward Transfer (LIFT) and Laser-Induced Reverse Transfer (LIRT) which has been shown to be successful in the creation of metal and metal-hybrid ultrathin films on transparent substrates [14,15]. LIFT utilises a target of a prepared film coated on optically transparent media (referred to as a donor), typically glass or a polymer, which is then subject to laser irradiation. This irradiation results in material transfer from the donor to a substrate, referred to as the acceptor. The use of fs lasers ensures limited laser-plume interaction, thus allowing ultrathin films to be deposited in a uniform manner. Similarly, LIRT can be used to produce ultrathin films, but with laser irradiation of

the donor occurring through an acceptor which is transparent to the laser radiation. LIRT can also be used with bulk donor material, eliminating the need for prepared films prior to material transfer.

PLD in air has also been achieved, and is conventionally performed by placing the target within several millimetres of, and at an acute angle with respect to, the substrate with target irradiation occurring parallel to the substrate [16]. This technique has been successful for the creation of nanostructured gold [17] and diamond-like carbon [18] films.

Another successful variant of PLD for nanostructured film creation is Confined PLD which is achieved through spatially confining the expansion of the plasma plume by placing a transparent substrate in close proximity (approximately 50 μm) to the target, with target illumination occurring through the substrate. This proximity confines the plume in the direction of travel, sustaining a higher plasma density and election temperature at the deposition site with the plume condensing in the form of a nanomaterial film [19]. To date, this technique has been reported for depositions at high vacuum (10^{-5} mbar).

In this chapter, a new variant of PLD is presented, which is termed "*Confined Atmospheric PLD*" (CAP), whereby confined PLD is demonstrated for the first time at ambient atmospheric pressure using a picosecond pulsed solid-state laser. This technique is demonstrated for the deposition of nanostructured gold thin films, with the resultant film analysed in terms of morphology, optical properties, surface chemistry and crystalline structure.

5.2 Experimental Method

5.2.1 Laser Deposition Setup

The laser ablations were performed using the laser system described in Section 3.2. The experimental setup is a simplified form of conventional PLD whereby a transparent substrate is placed either in direct contact with a metallic target or with a spacer in between the target and substrate with the ablation performed under the prevailing ambient (atmospheric) conditions, see Figure 5.1. For the results presented here, the target-to-substrate distance was 50 μm with the substrate fixed in place mechanically for the duration of processing.

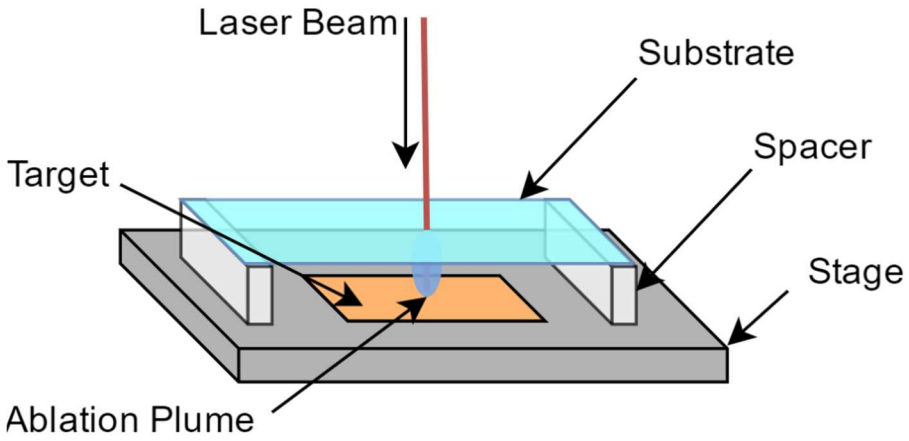

Figure 5.1: Schematic of the confined atmospheric pulsed laser deposition setup.

For the experiments performed in this study, the laser beam was focused to a spot diameter of 140 µm and unidirectionally rastered at a rate of 10 mm/s across the target, mapping out a 5 × 5 mm area in parallel lines with a 50 µm step between each successive line. The current experimental setup allows for depositions over areas up to 100 cm^2 but can be easily increased through alteration of the optical setup of the laser. This process is differentiated from the similar technique LIRT by the use of longer laser pulse widths allowing for increased plume/laser interaction.

5.2.2 Materials

The target material was a gold foil (99.9% metals basis, Agar Scientific, UK) with a thickness of 100 µm. The substrate material was a 188 µm thick ZeonorFilm ZF14 (ZF14-188, Zeon Chemical L.P., Japan) cyclic olefin polymer (COP). The laser beam is incident on the target though the substrate, with the resultant ablation plume travelling towards the substrate. This offers a promising opportunity to rapidly deposit nanostructured materials on transparent thin substrates, with enhanced adaptability. The use of flexible substrates also allows for the process to be adapted for high volume roll-to-roll production.

5.2.3 Substrate Characterisation

The metrology of the deposited nanomaterial was analysed using Scanning Electron Microscopy (SEM) with an Evo LS50 (Zeiss, Switzerland). The samples were carbon coated to ensure conductivity prior to analysis with an Scancoat Six (Edwards, United Kingdom) sputter coater. Changes to the optical properties of the COP after deposition were examined using a Cary 50 UV-Vis-NIR spectrometer (Agilent, USA) scanning

from 200 to 1100 nm at a rate of 600 nm/min. Attenuated Total Reflectance Fourier-Transform Infrared Spectroscopy (ATR-FTIR), which has a sampling depth up to 2 μm, was used to examine changes to the chemistry of both the surface and subsurface of the substrates after deposition using a Spectrum 100 (PerkinElmer, USA). Four scans were taken over the range 4000 – 600 cm^{-1} at resolution of 1 cm^{-1}. The crystalline structure of the gold nanoparticles (AuNPs) was investigated using X-Ray Diffraction (XRD) with an AXS D8 (λ = 0.154 nm) x-ray diffractometer (Brucker, Germany).

5.3 Results

5.3.1 Surface Morphology

Figure 5.2 shows SEM images of the gold nanoparticles (AuNPs) deposited on the COP substrates via CAP at laser fluences of 0.22 J/cm^2 and 0.48 J/cm^2. For the lower fluence depositions a film was evident along with discrete clusters of aggregated nanostructured particles ranging from hundreds of nanometres to tens of microns in diameter, see Figure 5.2a. At higher fluence depositions (Figure 5.2b) the film was seen to be more uniform with less meso- and microparticle aggregates than for lower fluence depositions.

As of yet, the upper limit of film thicknesses deposited via the CAP technique has not been determined, though thicknesses up to 18 μm have been found, as shown in Figure 5.3. Work on gold films deposited via LIRT found that the process window for deposition was quite small (at pulse energies from 36 – 40 nJ) [15]. Depositions via the CAP technique were performed at larger pulse energies and over a larger range (from 18 – 37 μJ) allowing for higher material removal from the target as well as higher plume velocities, which may allow ultimately higher film thicknesses to be deposited.

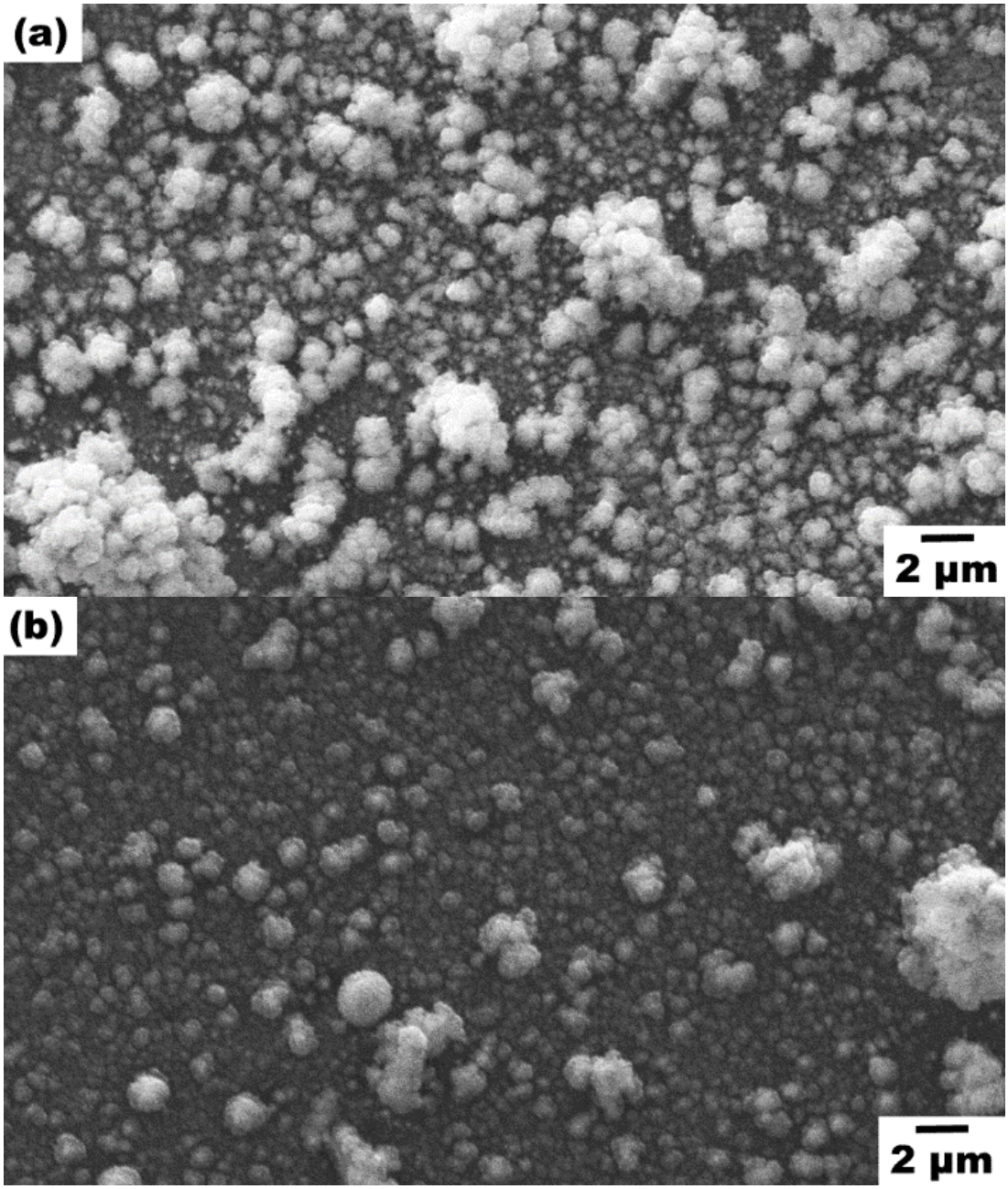

Figure 5.2: SEM images of gold nanoparticles deposited on COP via CAP using a laser fluence of (a) 0.22 J/cm2 and (b) 0.48 J/cm^2.

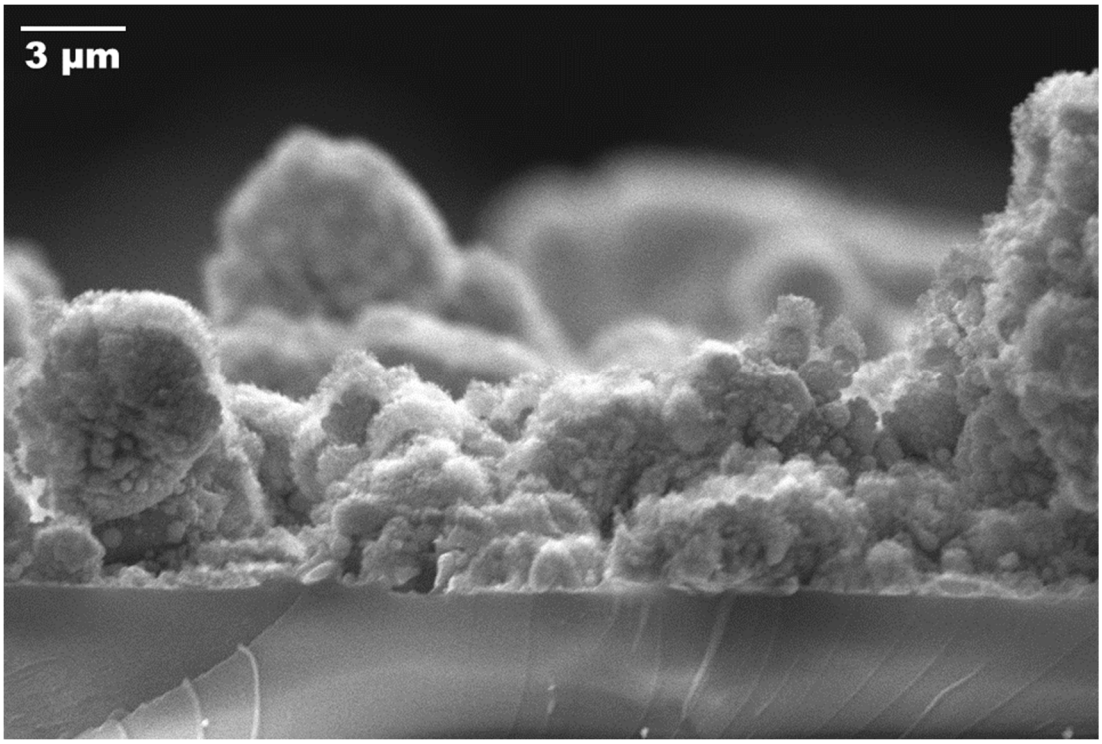

Figure 5.3: Cross-sectional SEM image of nanostructured gold particles deposited at a laser fluence of 0.22 J/cm^2.

5.3.2 Optical Properties

As native COP is noted for its high transparency from the NIR to Mid-UV wavelengths [20], which can be useful for photometric sensing applications, UV-Vis-NIR spectroscopy was performed to examine changes in the optical properties of the COP substrate after deposition. The transmission spectra of the COP before and after deposition is shown in Figure 5.4. After deposition, a broadband decrease in transmission of between 10% - 80% across all wavelengths was observed with this decrease becoming higher at longer wavelengths.

The plasmonic behaviour of the film was also analysed using UV-Vis-NIR absorbance spectroscopy which showed the appearance of a broad absorbance band after deposition, centred at 598 nm (inset Figure 5.4). This peak position is indicative of a surface plasmon resonance found for gold nanoparticles, however the broad nature of the band may indicate a large size dispersion of the deposited film [21].

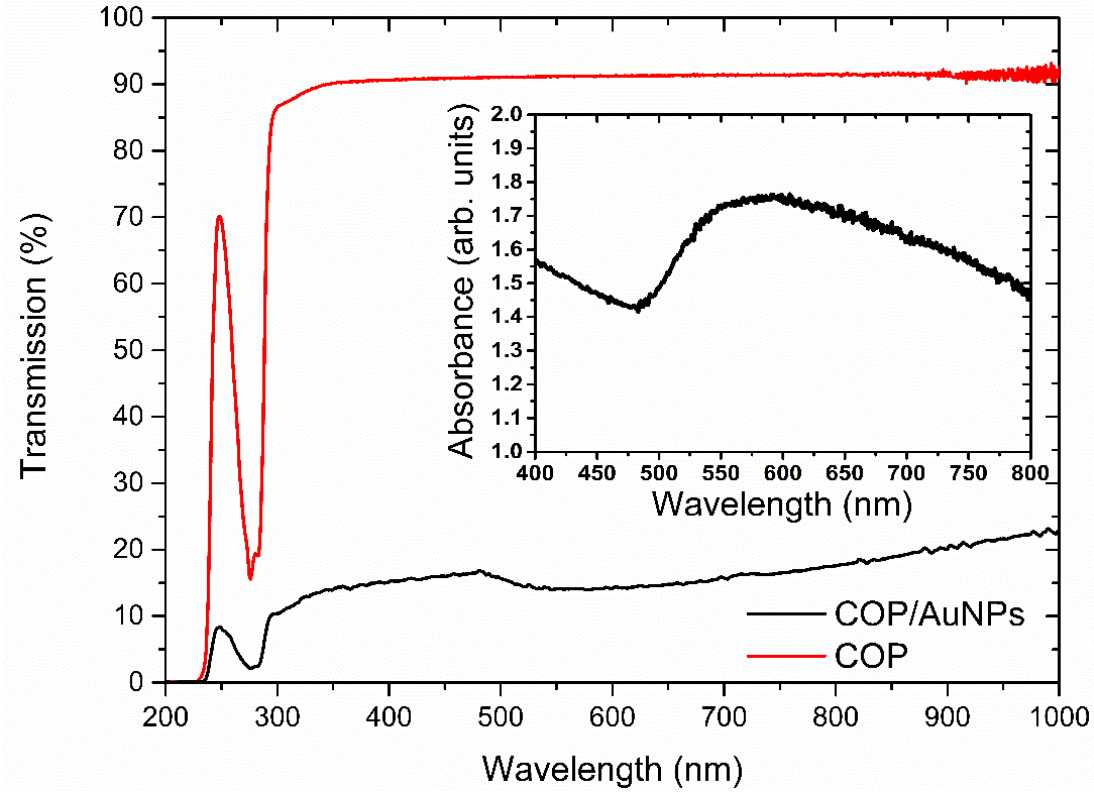

Figure 5.4: UV-Vis-NIR transmission spectra of the native COP substrate and COP after deposition of AuNPs. Inset shows the post-deposition spectrum converted to absorbance from 400 – 800 nm highlighting the appearance of an absorbance band centred at 598 nm.

5.3.3 Surface Chemistry

Changes in the surface chemistry of the polymer film as a result of the laser deposition process were examined using ATR-FTIR spectroscopy, see Figure 5.5. Samples processed at the maximum fluence (0.48 J/cm^2) were chosen for analysis as any thermal degradation of the substrate would be more evident than when compared to lower fluence ablations. The largest features in the IR spectra before and after deposition were two large absorbance peaks between 2900 – 2800 cm^{-1}, attributed to C–H stretching, and another at approximately 1480 cm^{-1} attributed to C-H bending. A smaller peak was seen at approximately 1700 cm^{-1} which was attributed to carbonyl groups [22]. Though no new features were seen in the sample post-deposition, there was a broadband decrease in transmission across the full wavenumber range for all samples, attributed to the deposited material reducing the sampling depth into the polymer bulk.

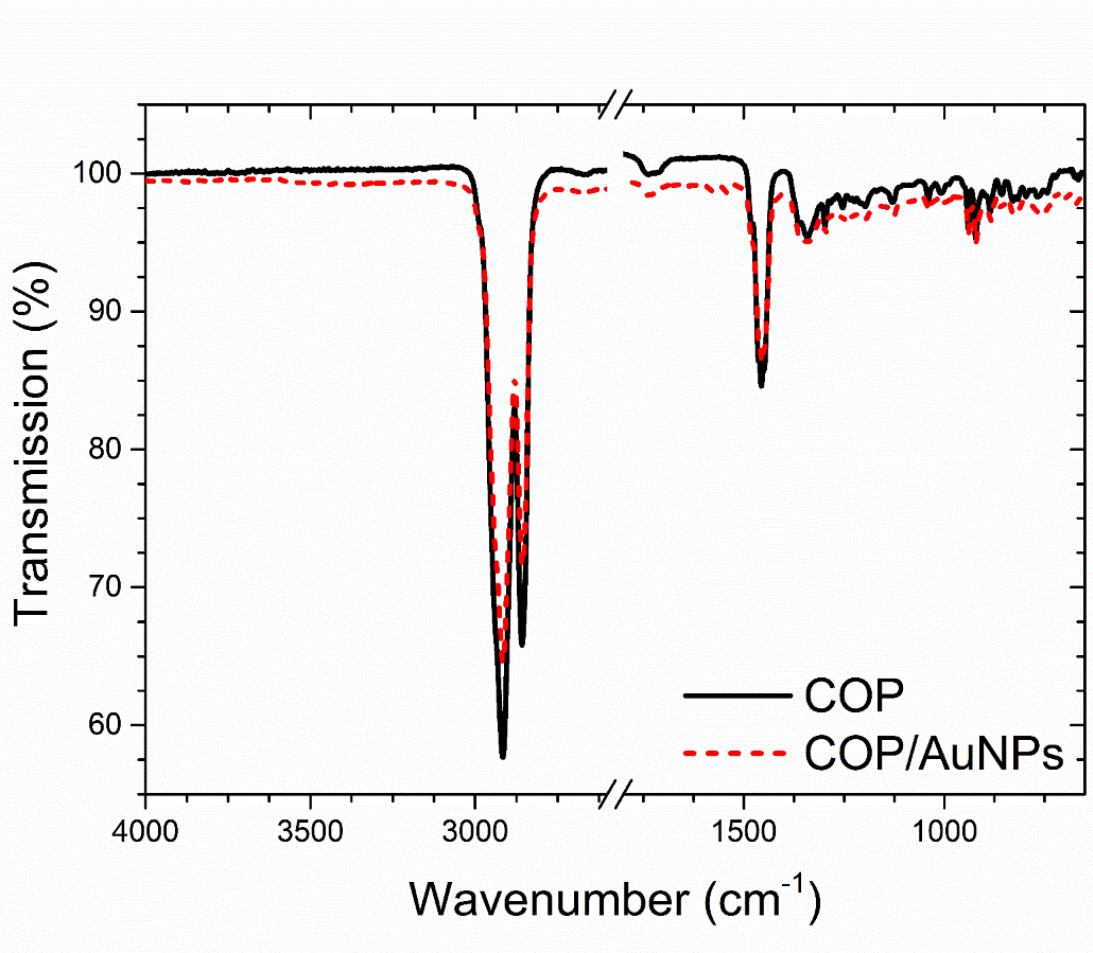

Figure 5.5: ATR-FTIR spectra of COP substrate and COP and after AuNP deposition at a fluence of 0.48 J/cm2.

5.3.4 Crystalline Structure

XRD analysis was performed to examine the crystalline structure of the substrate and deposited gold nanoparticles, and the resultant spectrum is shown in Figure 5.6. A large broadband diffraction peak is noted from the amorphous COP substrate from 10º to 30º. The presence of four characteristic peaks was also noted, corresponding to the (111), (200), (220) and (311) peaks of face-centred cubic gold. The peak at 25° was attributed to the crystalline nitrocellulose in the adhesive tape used to affix the sample within the XRD sample stage, which may also contribute to the broadband diffraction peak below 20° [23]. An average crystallite size of 6.60 Å was estimated using the Scherrer equation, which is widely used to determine the crystallite size of polycrystalline samples [24], using the (111) peak [25].

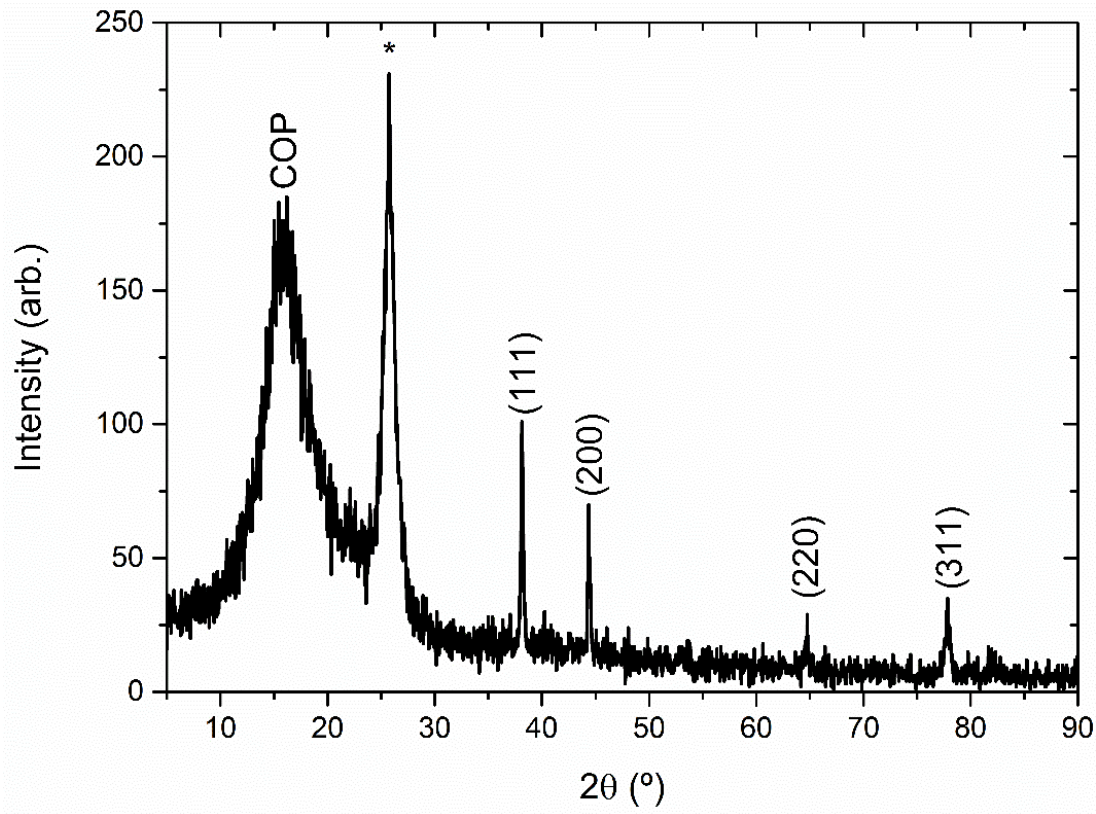

Figure 5.6: XRD spectrum of AuNPs deposited on a COP substrate with principal Bragg reflections labelled. The peak at 25° was attributed to the nitrocellulose-based adhesive tape used to affix the sample on the XRD stage.

5.4 Discussion

As the larger nanostructured aggregate particles were less evident at the higher fluence depositions, it can be asserted that they are likely a result of in-plume aggregation due to colder plasma temperatures at lower ablation fluences [26]. Target fragmentation was ruled out as the mechanism for the larger aggregated particle formation, as at higher fluences larger ablated particulates would have been both more preferentially generated and would have sufficient kinetic energy to reach the substrate and thus would have been more evident as fluence increased. As seen for low-pressure confined PLD, the spatial confinement of the plume, achieved by placing the substrate in close proximity of the target, allows for high plasma temperatures which drive the formation of nanomaterial deposition at the substrate surface [19,27]. Through reducing the target-to-substrate distance, and thereby allowing deposition at higher plasma temperature and ablation fluence, it may be possible to further reduce the size of the

deposited nanoparticles. The higher temperature depositions may remove the larger, aggregated particles with sizes outside of the nanoscale.

The broadband nature of the plasmonic peak found via absorption spectroscopy suggests a large nanoparticle size dispersion, while the largest portion of the band trending towards longer wavelengths is indicative of a dispersity weighted towards larger nanoparticles sizes as evident from Figure 5.4 [28]. Tailoring of both the optical transmission and the plasmonic response of the thin film may be possible through alteration of the thickness of the deposited material and the deposited nanoparticle size respectively.

Previous work on the thermal degradation of COC has seen the formation of spectral features such as increased C=O stretching at 1710 cm^{-1}, increased C-H stretching (2900 – 2800 cm^{-1}) and the formation of a large band at 4000 – 3000 cm^{-1} (indicative of hydroxyl group formation) [22,29].

As the C-H and C=O bonds are at similar intensities before and after deposition, there has been limited oxidation and dehydrogenation of the surface due to the laser deposition process. Though some reduction in transmission was evident, this was attributed to the deposited gold film reducing the sampling depth into the COP bulk. Similarly, though some reduction in the C–H stretching mode was evident at 2950 – 2800 cm^{-1}, there was no corresponding reduction in the C–H bending mode signal which would be expected at 1500 cm^{-1}.

Though no significant degradation was seen over the range of fluences examined in this work, previous studies have demonstrated substrate melting at fluences of 0.34 J/cm^2 and substrate warping at fluences of 0.79 J/cm^2 [29]. Neither warping or melting was evident from the morphological examination both visually and via SEM, however it is possible that damage may become evident if a larger laser fluence range is examined. It may be possible to mitigate this damage through the use of focusing optics (allowing for a smaller beam waist at the target than the substrate) or through increasing target-to-substrate distance.

From the XRD analysis, the peak positions for the principal Bragg reflections are similar to that reported previously for AuNPs synthesized via wet chemical and biological techniques [30–32]. A value of 1.185 was found for the ratio of the (200) and (111) peaks. This ratio, being close to unity, indicates limited preferential growth along the (200) or (111) planes [25] while the appearance of the less prominent (220) and (311) peaks may suggest an anisotropic nature of the deposited particles [25]. The

emission at 25°, which was attributed to the nitrocellulose adhesive tape used to affix the sample in the XRD, is also consistent with other data using the same method for XRD sample preparation [23].

Ultimately, this method allows for the rapid and scalable deposition of gold nanomaterials on COP surfaces, which would have potential applications in bioelectrochemical detection [33], selective protein extraction platforms [34], and stationary and pseudo-stationary phases for gas chromatography [35]. Though not explored further in this thesis, if suitable target materials were used (such as aluminium or titanium which have been previously demonstrated for UTLC applications) this novel technique would allow for the deposition of nanomaterial stationary phase materials in COP-based UTLC platforms.

5.5 Conclusions

In conclusion, the CAP process shows significant scope for the production of nanostructured thin films in ambient pressure conditions via laser ablation. Of specific interest is the ability for the fabrication of gold nanostructured thin films on polymer substrates for sensing applications. The polymer substrate showed no significant signs of degradation due to pulsed laser deposition, and the deposited gold film was seen to be plasmonically active. By varying the laser fluence, it was possible to alter the coverage and morphology of the deposited gold film. Though demonstrated for small areas in this work, when scaled, the process will allow for single step deposition of large area nanomaterial thin films on flexible substrates while being compatible with roll-to-roll processing for production scale-up. Future work towards optimization of the CAP process should lead to a simplified process for the fabrication of flexible electrodes suitable for chemical sensing and surfaces suitable for surface plasmon resonance spectroscopy, or solid-phase extraction. If more suitable materials were used, such as silicon, titanium or aluminium, this method could be applied towards the deposition of stationary phases for planar chromatographic platforms.

References

[1] Monaghan E, Michna T, Gaman C, O'Farrel D, Ryan K, Adley D, et al. Characterisation of thin film silicon films deposited by plasma enhanced chemical vapour deposition at 162MHz, using a large area, scalable, multi-tile-

electrode plasma source. Thin Solid Films. 2011 Aug;519(20):6884–6.

[2] Scardaci V, Coull R, Lyons PE, Rickard D, Coleman JN. Spray Deposition of Highly Transparent, Low-Resistance Networks of Silver Nanowires over Large Areas. Small. 2011 Sep 19;7(18):2621–8.

[3] Boyd IW. Thin film growth by Pulsed Laser Deposition. Ceram Int. 1996 Jan;22(5):429–34.

[4] Rebollar E, Sanz M, Esteves C, Martínez NF, Ahumada Ó, Castillejo M. Gold coating of micromechanical DNA biosensors by pulsed laser deposition. J Appl Phys. 2012;112(8).

[5] Escobar-Alarcón L, Arrieta A, Camps E, Romero S, Fernandez M, Haro-Poniatowski E, et al. Influence of the plasma parameters on the properties of aluminum oxide thin films deposited by laser ablation. Appl Phys A. 2008 Nov;93(3):605–9.

[6] Cueto M, Sanz M, Oujja M, Gámez F, Martínez–Haya B, Castillejo M. Platinum Nanoparticles Prepared by Laser Ablation in Aqueous Solutions: Fabrication and Application to Laser Desorption Ionization. J Phys Chem C. 2011 Nov 17;115(45):22217–24.

[7] Sanz M, De Nalda R, Marco JF, Izquierdo JG, Bañares L, Castillejo M. Femtosecond pulsed laser deposition of nanostructured CdS films. J Phys Chem C. 2010;114(11):4864–8.

[8] Sanz M, opez-Arias ML, Marco JF, de Nalda R, Amoruso S, Ausanio G, et al. Ultrafast Laser Ablation and Deposition of Wide Band Gap Semiconductors. J Phys Chem C. 2011;115:3203–11.

[9] Guan L, Zhang D, Li X, Li Z. Role of pulse repetition rate in film growth of pulsed laser deposition. Nucl Instruments Methods Phys Res Sect B Beam Interact with Mater Atoms. 2008;266(1):57–62.

[10] Galca AC, Stancu V, Husanu MA, Dragoi C, Gheorghe NG, Trupina L, et al. Substrate–target distance dependence of structural and optical properties in case of Pb(Zr,Ti)O3 films obtained by pulsed laser deposition. Appl Surf Sci. 2011;257(14):5938–43.

[11] Fazio E, Neri F, Ossi PM, Santo N, Trusso S. Growth process of nanostructured silver films pulsed laser ablated in high-pressure inert gas. Appl Surf Sci. 2009;255(24):9676–9.

[12] Amoruso S, Bruzzese R, Wang X, Nedialkov NN, Atanasov PA. Femtosecond

laser ablation of nickel in vacuum. J Phys D Appl Phys. 2007 Jan 21;40(2):331–40.

[13] Zeng X, Mao XL, Greif R, Russo RE. Experimental investigation of ablation efficiency and plasma expansion during femtosecond and nanosecond laser ablation of silicon. Appl Phys A. 2005 Feb 1;80(2):237–41.

[14] Flury M, Pédri C. Laser Induced Reverse Transfer with metal and hybrid material prepared with sol–gel process used on glass substrate. Appl Surf Sci. 2013 Aug;278:142–5.

[15] Dhami G, Tan B, Venketakrishnan K. Laser induced reverse transfer of gold thin film using femtosecond laser. Opt Lasers Eng. 2011 Jul;49(7):866–9.

[16] Steigert J, Haeberle S, Brenner T, Müller C, Steinert CP, Koltay P, et al. Rapid prototyping of microfluidic chips in COC. J Micromechanics Microengineering. 2007 Feb 1;17(2):333–41.

[17] Nedyalkov N, Nikolov A, Atanasov P, Alexandrov M, Terakawa M, Shimizu H. Nanostructured Au film produced by pulsed laser deposition in air at atmospheric pressure. Opt Laser Technol. 2014;64:41–5.

[18] Kononenko T V, Konov VI, Lubnin EN, Dausinger F. Pulsed laser deposition of hard carbon coatings at atmospheric pressure. Quantum Electron. 2003 Mar 31;33(3):189–91.

[19] Donnelly T, Lunney JG. Confined laser ablation for single-shot nanoparticle deposition of silver. Appl Surf Sci. 2013 Oct;282:133–7.

[20] Khanarian G, Celanese H. Optical properties of cyclic olefin copolymers. Opt Eng. 2001 Jun 1;40(6):1024.

[21] Amendola V, Pilot R, Frasconi M, Maragò OM, Iatì MA. Surface plasmon resonance in gold nanoparticles: a review. J Phys Condens Matter. 2017 May 24;29(20):203002.

[22] Suriano R, Kuznetsov A, Eaton SM, Kiyan R, Cerullo G, Osellame R, et al. Femtosecond laser ablation of polymeric substrates for the fabrication of microfluidic channels. Appl Surf Sci. 2011 May;257(14):6243–50.

[23] Inguva S, Vijayaraghavan RK, McGlynn E, Mosnier J-P. High quality interconnected core/shell ZnO nanorod architectures grown by pulsed laser deposition on ZnO-seeded Si substrates. Superlattices Microstruct. 2017;101:8–14.

[24] Tiago F, Muniz L, Aurélio M, Miranda R, Morilla C, Santos D, et al. The

Scherrer equation and the dynamical theory of X-ray diffraction. Acta Cryst. 2016;72:385–90.

[25] Kumar A, De A, Saxena A, Mozumdar S, Maye M M LJHLKNN and ZCJ, M HM and D, et al. Environmentally benign synthesis of positively charged, ultra-low sized colloidal gold in universal solvent. Adv Nat Sci Nanosci Nanotechnol. 2014 May 13;5(2):025017.

[26] Gamaly EG, Madsen NR, Rode A V., Goldberg D. Formation of Nanoclusters in Expanding Laser Plume. Int J Nanosci. 2010 Aug;09(04):371–5.

[27] Gao X, Liu L, Song C, Lin J. The role of spatial confinement on nanosecond YAG laser-induced Cu plasma. J Phys D Appl Phys. 2015 May 8;48(17):175205.

[28] Longobucco G, Fasano G, Zharnikov M, Bergamini L, Corni S, Rampi MA. High stability and sensitivity of gold nano-islands for localized surface plasmon spectroscopy: Role of solvent viscosity and morphology. Sensors Actuators B Chem. 2014;191:356–63.

[29] McCann R, Bagga K, Groarke R, Stalcup A, Vázquez M, Brabazon D. Microchannel fabrication on cyclic olefin polymer substrates via 1064 nm Nd:YAG laser ablation. Appl Surf Sci. 2016 Nov;387:603–8.

[30] Narayanan KB, Sakthivel N. Coriander leaf mediated biosynthesis of gold nanoparticles. Mater Lett. 2008 Dec;62(30):4588–90.

[31] Chen Y, Gu X, Nie C-G, Jiang Z-Y, Xie Z-X, Lin C-J. Shape controlled growth of gold nanoparticles by a solution synthesis. Chem Commun. 2005;104(33):4181.

[32] Singaravelu G, Arockiamary JS, Kumar VG, Govindaraju K. A novel extracellular synthesis of monodisperse gold nanoparticles using marine alga, Sargassum wightii Greville. Colloids Surfaces B Biointerfaces. 2007;57(1):97–101.

[33] Kang H, Zhu Y, Yang X, Shen J, Chen C, Li C, et al. Gold/mesoporous silica-fiber core-shell hybrid nanostructure: a potential electron transfer mediator in a bio-electrochemical system. New J Chem. 2010;34(10):2166.

[34] Alwael H, Connolly D, Clarke P, Thompson R, Twamley B, O'Connor B, et al. Pipette-tip selective extraction of glycoproteins with lectin modified gold nano-particles on a polymer monolithic phase. Analyst. 2011 Jun 21;136(12):2619–28.

[35] Duan A-H, Xie S-M, Yuan L-M. Nanoparticles as stationary and pseudo-stationary phases in chromatographic and electrochromatographic separations. TrAC Trends Anal Chem. 2011 Mar;30(3):484–91.

Chapter 6

Direct Laser Fabrication of Microstructured Cyclic Olefin Polymer-based Planar Chromatography Platforms

Publication Status: Under-Preparation

McCann R, Bagga K, A, Stalcup A, Vazquez M, Brabazon D. Direct laser fabrication of microstructured cyclic olefin polymer-based planar chromatography platforms

6.1 Introduction

The current fabrication methods for UTLC platforms (mentioned in Chapter 2) tend towards labour- and cost-intensive techniques such as CVD and ALD. Though these techniques are suited towards the fabrication of the structures and functionalities required for planar chromatography, the per-device cost is high. As planar separation techniques are typically used as low-cost alternatives to (or for method development of) liquid or gas chromatography, there is a need to keep device costs down for any UTLC platform. As discussed in Section 2.3, laser fabrication techniques offer an excellent low-cost alternative for the creation of micro- and nanoscale features on a range of materials.

Cyclic olefin polymer (COP) was chosen as the substrate material for its superior optical properties and chemical resistance [1,2]. As mentioned in Section 3.1, COP is finding increasing uses in analytical applications such as lab-on-a-chip systems [3] and substrates for capillary electrophoresis [4], DNA microarrays [5]. Though to date it has never been applied directly as the separation medium, its resistance to common acids, bases and polar solvents make it an excellent candidate material.

As the surface functionality has a large effect on the resulting separation capabilities, it would be beneficial if functionalisation of the substrate material was possible to allow for platform adaptability. Various surface modification routes for COPs and COCs have been noted in the literature including oxygen [6,7] and oxygen-argon [8] plasma treatments and chemical functionalization [9], further making COP an excellent material of choice for a planar chromatography platform.

This chapter presents an investigation into the fabrication of planar chromatography platforms using laser ablation. The solvent flow capabilities of three different plate morphologies were examined using coloured dye, to determine an optimal plate morphology. As the initial spot size has a large effect on the resultant separation, an examination into controlling sample spot size via suspending the sample in acetone was performed. The plate was then used to perform the separation of organic dyes as a proof-of-concept test, which was then compared to a commercial reversed-phase C18 TLC plate. Also examined was functionalisation of the COP platforms via oxygen plasma exposure and APTES treatment and the effect of this on separation capabilities.

6.2 Experimental Methods and Materials

6.2.1 Materials

The substrate material for this study was cyclic olefin polymer (COP) of 188 µm thickness (manufactured by Zeon Chemical L.P., Japan sold from Ibidi, Germany).

6.2.2 UTLC Plate Design and Fabrication

The laser used to fabricate the UTLC plates was a 1064 nm diode-pumped solid-state neodymium-doped yttrium aluminium garnet (Nd:YAG) laser (BrightSolutions, Italy) with a maximum pulse energy of 180 µJ and pulse width of 600 ps. The laser beam was focused to a spot size of 100 µm. The same scanning galvanometer and nanoposition stage as described in Section 3.2 was used as before. The preparation method for laser ablation was straightforward, the electrostatic film removed from the COP before ablation, and the substrates washed with IPA and dried using compressed clean dry air after processing was complete. For SEM and 3D profilometric analysis the samples were coated in gold for analysis as described in Section 3.2.

Figure 6.1 shows SEM images of the three plate morphologies. Each "platform" consisted of an 80 mm × 30 mm piece of COP with three individual plates per platform. The plates consisted of microchannels over a 25 mm × 65 mm area. The plates were comprised of v-shaped microchannels with a 100 µm gap between channels. Three microchannel morphologies were trialled to examine their flow behaviour: parallel, crosshatched with a 45° angle relative to the direction of flow, and crosshatched with a 23° angle.

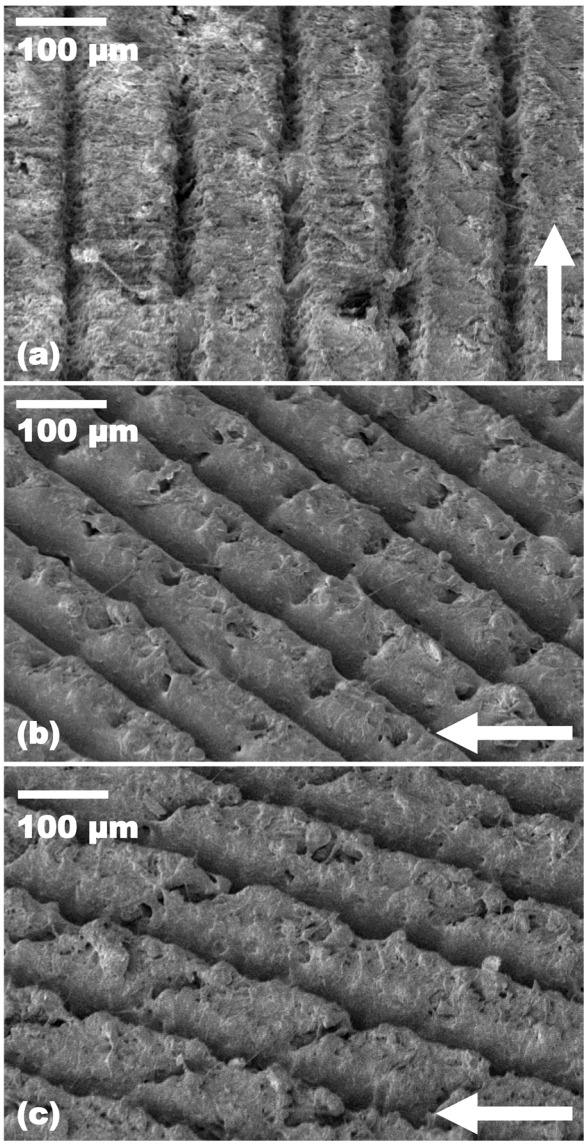

Figure 6.1: SEM images taken at a 45° tilt to the three plate surface morphologies showing (a) parallel channels, (b) 45° interconnected channels and (c) 23° interconnected channels with the direction of mobile phase flow indicated.

SEM analysis showed high surface areas within the microchannels, with further condensed debris around the channel crests and interchannel areas. 3D optical profilometry was used to measure the microchannel depths and widths, shown in Figure 6.2. The two crosshatched patterns exhibited differing microchannel depths depending on their angle relative to the direction of flow, with channels having a positive angle (which were ablated first, as shown in Figure 6.2) being larger in both depth and width than those with a negative angle.

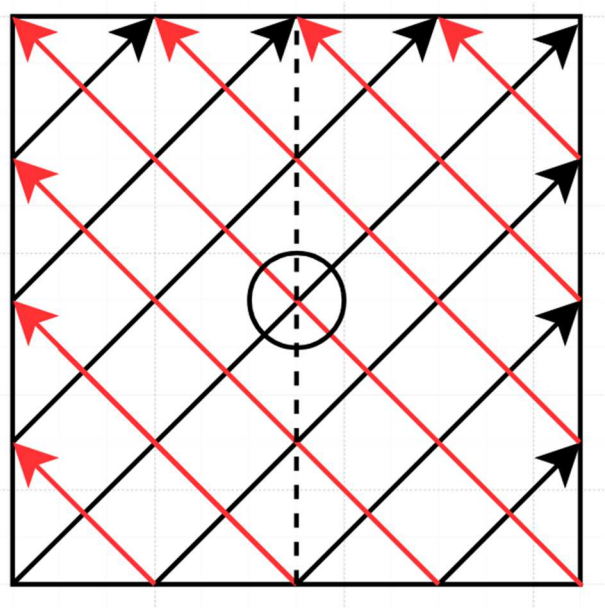

Figure 6.2: Laser scanning pattern the production of a 45° crosshatched plate, with the direction of scan indicated. The lines with a positive (+) angle with respect to the plate development direction (shown in black) are ablated first. Those with a negative (-) angle are ablated after all positive lines have been scanned.

Table 6.1: Dimensions for the three microchannel morphologies.

Morphology	Angle	Depth (µm)	Width (µm)
Parallel	N/a	13.5 ± 4.2	58.6 ± 2.8
45°	+	23.7 ± 10.8	67.7 ± 3.9
	–	10.9 ± 4.3	55.8 ± 10.1
23°	+	25.1 ± 5.6	78.6 ± 3.2
	–	5.4 ± 1.0	56.9 ± 13.6

6.2.3 Solvent Flow and Plate Spotting Study

The solvent flow study on the UTLC plates was performed by immersing the plates in 2 mL of a 1 mg/mL aqueous methylene blue solution. The solution was placed in a sealed container for 10 minutes prior to the plate being introduced to the solution to condition the atmosphere inside the container, after which the plate was introduced to the solution for a set time. The plate was then removed from the solution, the plate base was dried to stop the capillary action, and the position of the solvent front measured optically using a TLC plate imager (Camag, Switzerland). For these studies,

each plate contained three different microchannel morphologies, and each test was repeated three times.

The plate spotting test was performed using Analtech TLC Test Dye 30-03, which comprises of an aqueous solution of Fast Green FCF, Sudan Red, Bismark IV and Rhodamine 6G. The dye was applied at various volumes to the 45° crosshatched UTLC platform and a commercial RP-TLC plate. The dye was allowed to dry in ambient conditions for 5 minutes prior to imaging.

6.2.4 Surface Modification

Two surface modification strategies were examined: the use of air plasma treatment and the use of amination via chemical surface modification. The air plasma treatment was performed using a Harrick PDC-32G plasma cleaner. The plasma exposure was performed for 10 minutes, after which the plates were used immediately for separations to limit the effect of depassivation and recovery of the plate hydrophobicity. Previous studies using the same plasma cleaner for a 10-minute treatment showed a reduction in the contact angle of the COP from its native 88° to approximately 20° [10,11].

The surface aminiation was performed by first plasma treating the COP substrates as before, and subsequently immersing the plates in a 5% aqueous solution of (3-Aminopropyl)triethoxysilane (APTES; ≥98 % Sigma Aldrich) for 1 h at 50 °C. After removal from the APTES solution, the plates were washed with DI water and dried using nitrogen and used for separations as normal. Studies on APTES treated COP showed a reduction in the contact angle to approximately 47° after a combination of both O_2 plasma and APTES exposure [9]. This surface modification route should therefore provide an intermediate contact angle when compared to the hydrophobic untreated COP and hydrophilic plasma-treated COP.

6.2.5 Chromatographic Separations

In this study, the 45° crosshatched microchannel UTLC plates were compared to commercial RP-TLC plates (aluminium-backed RP-18 (C18) modified silica gel with F254s fluorescent indicator, Merck Millipore). The plates had a 200 µm layer thickness, and a pore size of 60 Å. The sample used to examine separation capabilities was a methanol solution of 1 mg/mL of both Fast Green FCF (Fast Green For Food

Colouring; ≥90%, SigmaAldrich) and Rhodamine 6G (~95%, SigmaAldrich) at a 1:1 ratio.

Samples were applied using a standard laboratory pipette which was held in contact with the with plate for 3 seconds to ensure the volume had fully dispensed. Sample volumes of 300 nL were used for separations on RP-18 plates, while 3 repeat sample applications of 300 nL (for a total of 900 nL sample applied) were used for the UTLC plates. The greater sample volume allowed for easier visual identification post-separation. After sample application, the plates were dried in an oven at 37 ˚C for 30 minutes prior to development to ensure the dye solution had thoroughly dried.

Three mobile phase compositions with differing percentages of ethyl acetate (EtAc; ChromaSolv® ≥99.7%, Sigma), methanol (MeOH; ChromaSolv® ≥99.9%, Sigma) and Deionised (DI) Water (Milli-Q water purification system, Merck Millipore, USA) were trialled to examine the effect on separation, as outlined in Table 6.2.

Post-separation analysis was performed via densitometric analysis via plate imaging. The RP-TLC plates were imaged using a TLC Analyser (Camag, Switzerland) and the UTLC plates were imaged with an iPhone SE (Apple, USA) in high dynamic range mode. Analysis of the recorded images was performed using ImageJ (National Institutes of Health, USA). Greyscale values were extracted for each chromatogram, and the data analysed using OriginPro 9 (OriginLab, USA) with a background subtraction applied to reduce noise resulting from the ambient lighting conditions. As the mobile phase front was not visualiable after separation on the UTLC plates, for the retention factor calculations presented below the position of the solvent front used was Z_x = 30.2 ± 0.5 mm.

Table 6.2: The mobile phase compositions used in the separation comparison test.

Component	Mobile Phase 1 (MP1)	Mobile Phase 2 (MP2)	Mobile Phase 3 (MP3)
EtAc	67%	50%	33%
MeOH	17%	25%	33%
DI Water	17%	25%	33%

6.3 Results

6.3.1 Effect of plate morphology on solvent flow

The flow behaviours of the three different plate morphologies were examined by immersing the plates in an organic dye solution and recording the position of the dye after a set time. The maximum and minimum position of the solvent/dye mixture after 30 s, 90 s, 180 s and 270 s is shown in Figure 6.3 and Figure 6.4 respectively. Of the three morphologies, the parallel microchannels showed the fastest development times, the 45° crosshatched channels showing the slowest development times.

The parallel microchannels showed a maximum solvent position of 42.7 mm after 30 s, and eluting off the end (at 65 mm) after 270 s. Similarly, the 23° microchannels had a maximum position of 21.3 ± 0.6 mm after 30 s and 60 ± 2.2 mm after 260 s. The 45° microchannels had a lower minimum and maximum position for across all measurements with a position of 21.3 ± 0.6 after 30 s up to 36.3 ± 1.0 mm after 270 s. From this result, it was decided to proceed with separations using the 45° crosshatched channel pattern UTLC plates.

Table 6.3 shows the average of the sample standard deviations of the solvent positions. The 45° microchannels had a significantly higher repeatability in solvent front positions lower average standard deviation in both the minimum and maximum positions than both the 23° and parallel channels. From this result, it was decided to proceed with separations using the 45° crosshatched channel pattern UTLC plates.

Table 6.3: Mean standard deviations of the maximum and minimum solvent positions for the three microchannel morphologies.

Standard Deviation	Parallel	45°	23°
Minimum Position (mm)	3.2	1.3	5.7
Maximum Position (mm)	3.4	1.45	5.6

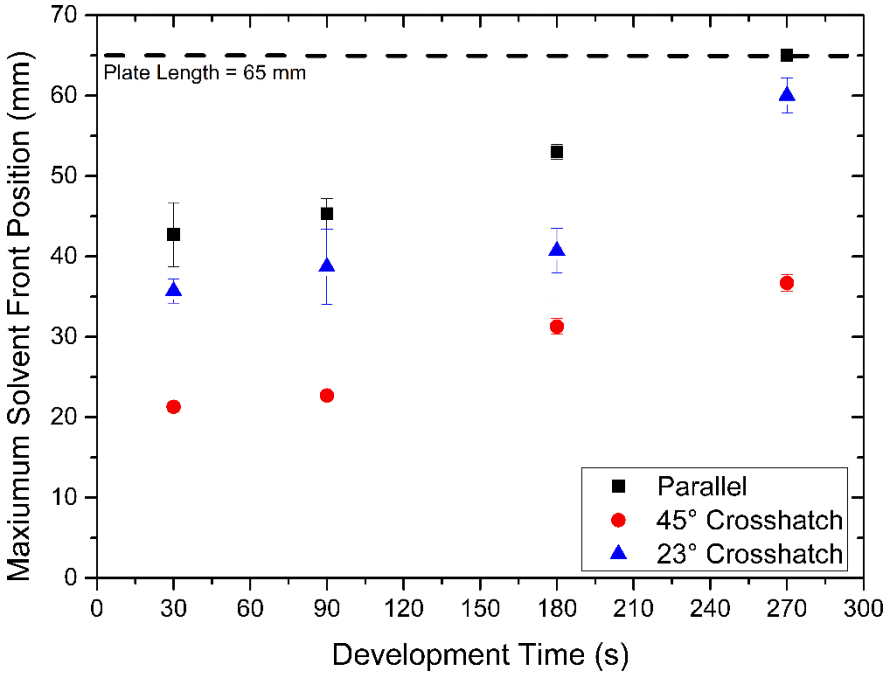

Figure 6.3: Maximum solvent front position for three UTLC plate morphologies. The total plate length was 65 mm, n = 3.

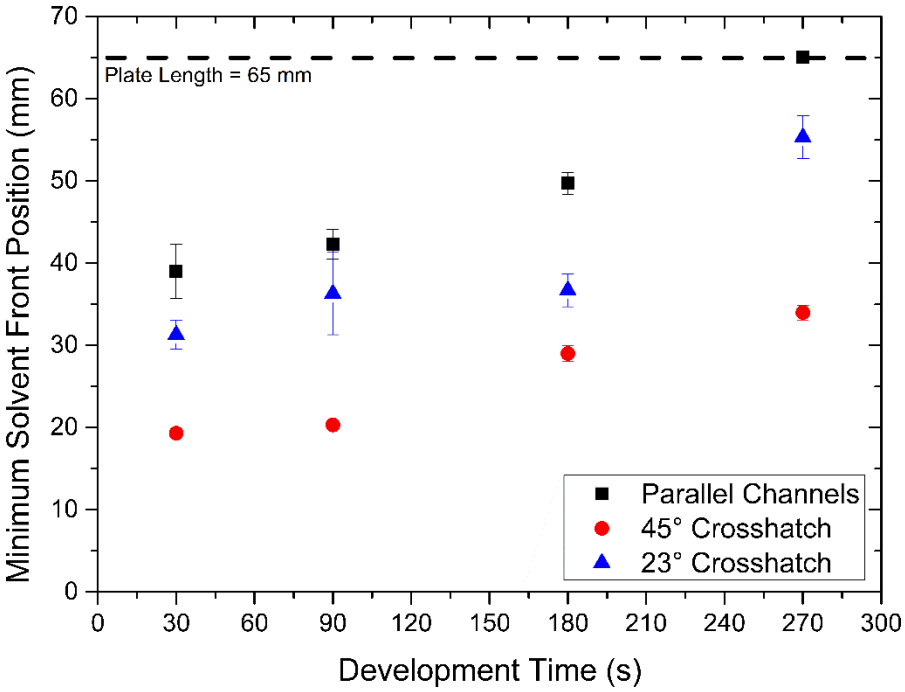

Figure 6.4: Minimum solvent position as a function of time for three different UTLC plate morphologies. The total plate length was 65 mm, n = 3.

6.3.2 Effect of liquid application volume of initial spot size

As described in Section 2.1.2, the initial liquid spot size can have a significant effect on the resulting separation, therefore the effect of the application liquid spot size was examined. Also examined was the effect of suspending the dye in a fraction of acetone which can act as a drying agent, potentially reducing initial liquid spot size further.

Figure 6.5 shows the effect of applied liquid volume and dye concentration on the resultant spot area. As expected, the larger application volumes resulted in larger spot areas, however the dye concentration in acetone also had a noted effect on the resultant spot area. For an application volume of 1000 nL and a 50% dye concentration, a spot area of 3.29 ± 0.36 mm^2 was found. For the same dye concentration and an application volume of 600 nL as spot area of 3.03 ± 0.03 mm^2 was found. At lower application volumes, spot areas ranged from to 0.37 ± 0.01 mm^2 for 100 nL and a 50% dye fraction, to 1.59 ± 0.14 mm^2 for a 300 nL application and an 80% dye fraction. For 300 nL volumes, the spot area was seen to plateau at dye fractions of 80% and above. For 100 nL applications, there was a linear increase up to a maximum 1.39 ± 0.08 mm^2 for a 100% dye fraction. From these results, 300 nL was chosen as the optimal value to compare with the UTLC plates.

The spotting of the UTLC plate revealed that the plate wets in a diagonal pattern (Figure 6.6). This is related to the nature of the laser tool-path, whereby channels of negative positive angle (with respect to the direction of flow) were ablated prior to a second pass writing those with a positive angle.

Figure 6.7 shows the comparison of spot areas on the commercial RP-TLC and the laser produced UTLC plates for a 300 nL application. The UTLC platform had a larger average spot area for all dye fractions used, peaking at 3.57 ± 0.35 mm^2 for a dye fraction of 80%. The smallest spot area for UTLC was for 50% dye at a spot area of 2.57 ± 0.38 mm^2. Though the smallest spot area was for a 50% dye fraction, the 100% dye solution had the smallest standard deviation with an area of 3.13 ± 0.15 mm^2. In comparison, the commercial RP-18 plate had smaller spot areas ranging from 0.89 ± 0.14 to 1.59 ± 0.14 mm^2 for dye fractions of 50% and 80% respectively. The spot areas were seen to plateau after 80% and had similar reproducibility across all dye fractions.

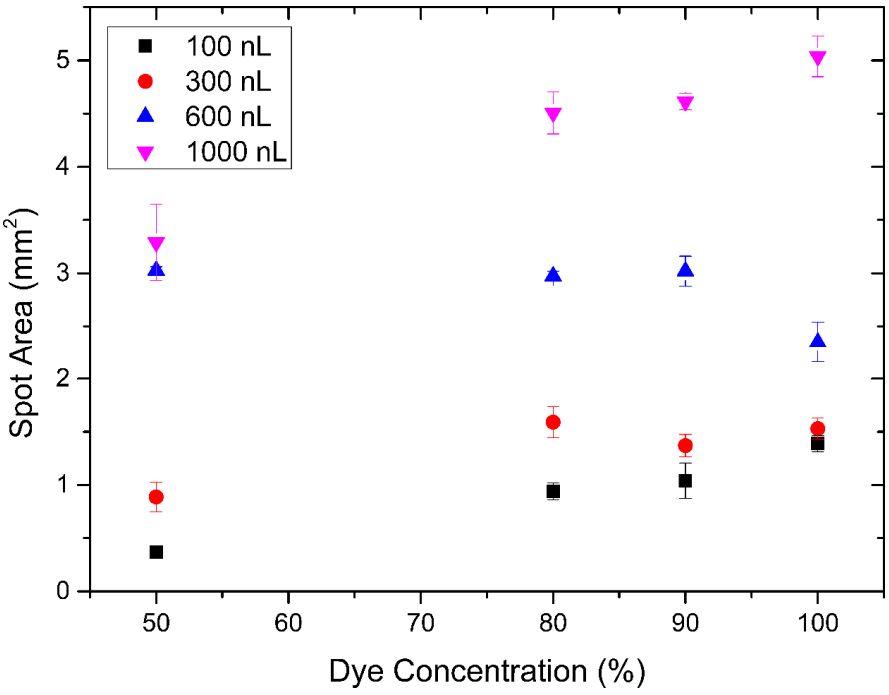

Figure 6.5: Spot areas for a range of application volumes and varying dye/acetone fractions applied to an RP-TLC plate, n = 3.

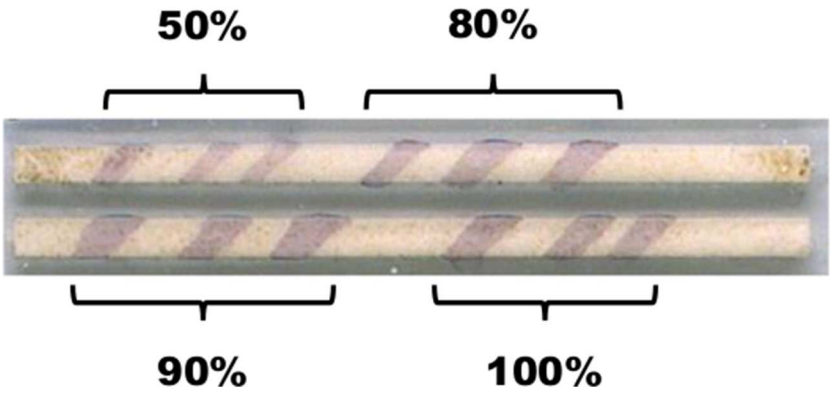

Figure 6.6: Results of the spotting test on the UTLC plate. The sample dries in a characteristic diagonal pattern, itself related to the microchannel network structure.

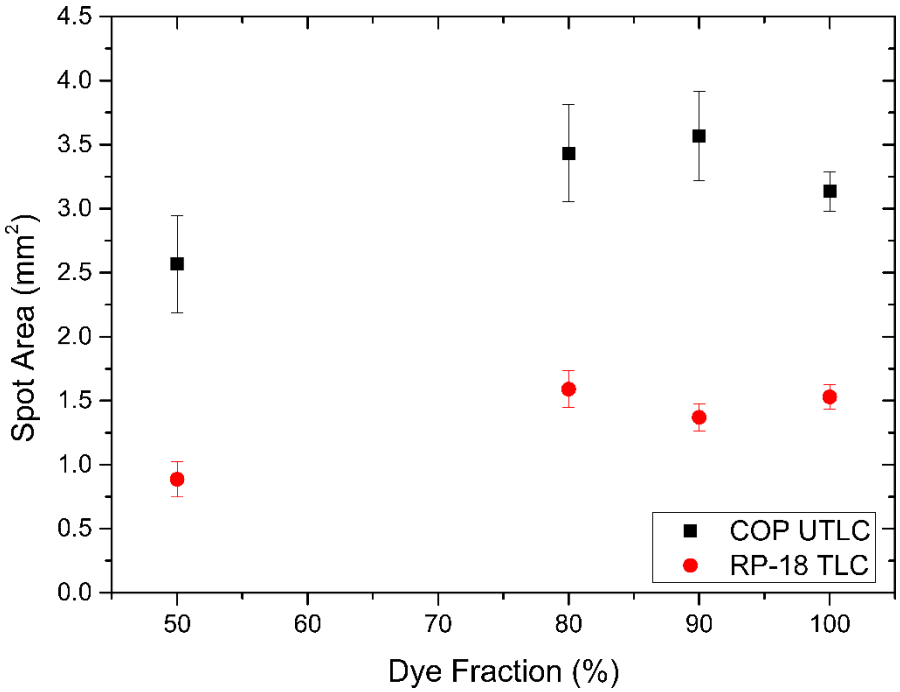

Figure 6.7: Comparison of spot areas on RP-TLC and UTLC plates with a 300 nL application of various acetone/dye fractions, n = 3.

6.3.3 Separation of Organic Dyes

To examine their chromatographic capabilities, the UTLC plates were applied towards the separation of a binary organic dye mixture: Fast Green FCF and Rhodamine 6G. The capabilities of the UTLC platform were compared under the same chromatographic conditions to commercially available RP-TLC C-18 plates.

Figure 6.8 shows the comparison between the UTLC plate and the commercial RP-TLC plate and the resulting chromatograms using Mobile Phase Composition 1 (an

8:2:2 ratio mix of EtAc, MeOH and DI Water) and the resultant chromatograms. The RP-TLC plate showed a lower retention factor for the Fast Green, with an R_f of 0.10 ± 0.07, and a higher retention factor for the Rhodamine 6G of 0.57 ± 0.08 (Figure 6.8a and c). There was a significant amount of tailing (evidenced by a faint streak behind the analyte) for the Rhodamine 6G. The tailing was less evident for the Fast Green, though the distance travelled by the analyte was comparatively less.

Similarly, the UTLC platform demonstrated a high retention factor of the Fast Green (0.00 ± 0.09) and a lower retention for the Rhodamine (0.18 ± 0.11) shown in Figure 6.8b and 6.6d. Unlike the reversed-phase plate, the two analytes were not separated by space. Also of note was some dye evident outside the edges of the channelled area of the plate. The dyes were separated over approximately 11 mm of length of the plate, compared to 9 mm of length of the reversed-phase plate.

6.3.4 Effect of Mobile Phase Composition

To further examine the separation capabilities of the UTLC platform, three different mobile phases were trialled with various fractions of ethyl acetate, methanol and water again for the separation the binary organic dye mixture. In keeping with the precedent set by other UTLC platforms, the separation time was 3 minutes.

Table 6.4 and 6.5 list the retention factors for the two dyes separated using three mobile phase compositions on both the UTLC and RP-TLC plates. Successful separations were achieved for mobile phase compositions 1 and 3. Mobile Phase 1 (an 8:2:2 ratio of EtAc, MeOH and DI Water) resulted in the Fast Green being fully retained by the stationary phase with an R_f value (i.e. ratio of the distance travelled by the analyte to the distance travelled by the mobile phase relative to the initial spotting position) of 0.00 ± 0.09, while the Rhodamine 6G had less affinity with the stationary phase demonstrating an R_f value of 0.18 ± 0.11 (Figure 6.8c and d). When Mobile Phase Composition 2 (a 4:2:2 ratio of EtAc, MeOH and DI Water) was trialled on the reversed-phase plate, the Fast Green and Rhodamine 6G had retentions of 0.90 ± 0.03 and 0.27 ± 0.06 respectively (shown in Figure 6.9a and b). When trialled on the UTLC platform, separation was only partially evident on one of the three plates, with the dye mixture appearing to streak up the length of the plate. Mobile Phase 3 (a 2:2:2 ratio of EtAc, MeOH and DI Water) showed somewhat similar separation to Mobile Phase 2, with a broad streak of dye along the length of the plate. Differing retention properties

of the Mobile Phase 3 (MP3) separations were seen when compared to Mobile Phase 1 (MP1) with the Fast Green having a higher of R_f value than previously of 0.65 ± 0.15, while the Rhodamine 6G was retained at a lower R_f of 0.34 ± 0.20 (see Figure 6.9c and d).

When the mobile phase compositions were used for separations on the reversed-phase TLC plates, similar retention behaviours were found. MP1 showed higher retention factors for the Rhodamine 6G, while the inverse was seen for MP3.

Table 6.4: Retention factors for Fast Green FCF for the three mobile phase compositions trialled on the UTLC and RP-TLC plates.

Mobile Phase Composition	UTLC	RP-TLC
MP1	0.00 ± 0.09	0.10 ± 0.07
MP2	–[5]	0.90 ± 0.03
MP3	0.65 ± 0.15	0.87 ± 0.03

Table 6.5: Retention factors for Rhodamine 6G for the three mobile phase compositions trialled on the UTLC and RP-TLC plates.

Mobile Phase Composition	UTLC (R_f)	RP-TLC (R_f)
MP1	0.18 ± 0.11	0.57 ± 0.08
MP2	-[1]	0.27 ± 0.06
MP3	0.34 ± 0.20	0.10 ± 0.06

[5] For MP2, the Fast Green was only separated in one of the three trialled separations, appearing with a higher retention factor than the remaining sample, which appeared as a streak along the length of the plate.

6.3.5 Effect of Surface Modification

Two surface modification strategies were trialled to examine the effect on the separation capabilities of the UTLC platform: plasma surface treatment and surface amination via APTES treatment. These plates were applied to the separation of the binary dye mixture as before using Mobile Phase Composition 1 so analyse the effect of surface modification, shown in Figure 6.10.

Table 6.6 shows the resulting retention factors for the dye mix on both the plasma and APTES modified UTLC plates. The plasma modified plate showed similar retention behaviours to that of the unmodified plates with the Fast Green being retained at a lower R_f than the Rhodamine 6G. However, both analytes travelled further along the plate, with the Fast Green and Rhodamine 6G having R_f values of +0.08 and +0.24 respectively when compared to the unmodified plate.

The APTES-modified plates again showed similar retention properties to that of the unmodified plates with Rhodamine 6G showing a +0.16 change in R_f. The Fast Green was not successfully resolved, though a dark blue band was evident between the initial spotting position and the Rhodamine 6G.

Table 6.6: Retention factors for the Fast Green and Rhodamine 6G dyes on the APTES- and Plasma-modified plates.

Surface Modification	Fast Green FCF (R_f)	Rhodamine 6G (R_f)
Plasma	0.08 ± 0.26	0.42 ± 0.13
APTES	-[6]	0.34 ± 0.14

[6] Fast Green was not successfully separated on the APTES functionalised plate, being retained within a blueish mixture possibly containing Rhodamine 6G.

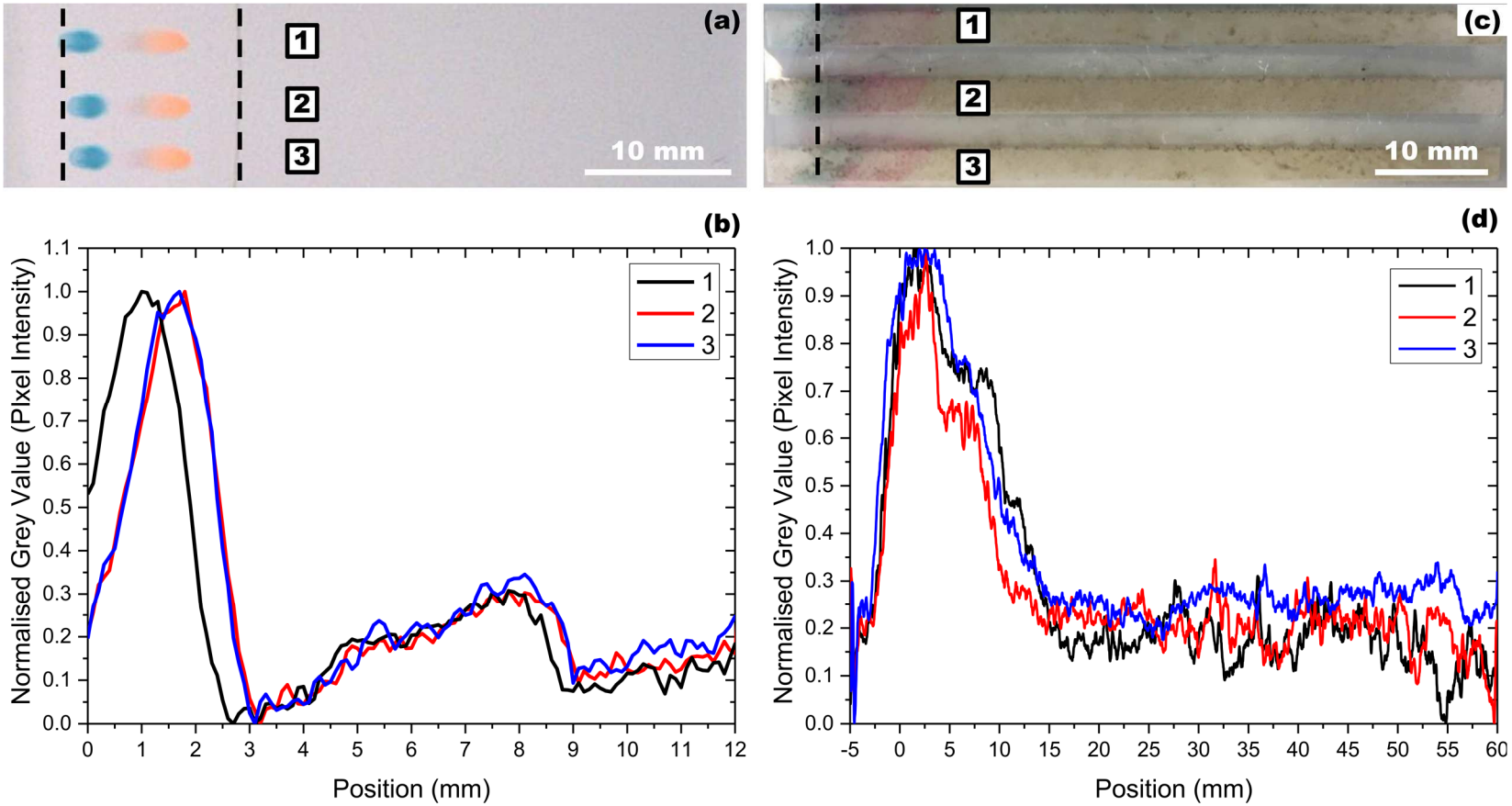

Figure 6.8: Comparative retention of Fast Green FCF (blue) and Rhodamine 6G (orange/pink) on a (a) commercial RP-18 TLC plate and (c) the UTLC platform under the same chromatographic conditions and development time (3 minutes). The grey pixel intensity was extracted from the recorded images with (b) and (d) showing the resulting chromatograms for both the RP-TLC plate and UTLC plate respectively, n = 3.

6.4 Discussion

The flow behaviour study showed that of the three trialled morphologies, the 45° crosshatched pattern had the highest repeatability in both the maximum and minimum position (shown in Figure 6.3 and 6.3). Both the parallel microchannels and the 23° crosshatched demonstrated higher flow rates, with an exponential increase from 180 s onwards. This higher flow rate would lower the interaction time between the analyte and polymer. The 45° crosshatch exhibited a more linear flow rate, while also having the highest repeatability in solvent front position. As such, it was decided to apply the 45° crosshatched UTLC plates towards the organic dye separation later in this study. A study on 3D printed planar chromatography plates showed significant streaking with parallel microchannels, with separated analytes having spot sizes of 5 – 20 mm [10]. The 45° crosshatch may also help to mitigate the streaking seen with parallel microchannels by allowing increased flow.

The COP-based UTLC platform demonstrated a much higher spot application size when compared to that of commercial RP-TLC plates (shown in Figure 6.7). This is to be expected as the RP-TLC stationary phase is comprised of a 200 µm thickness porous layer, which allows more dye to be retained in the bulk of the application site. As the UTLC platform is comprised of non-porous microchannels, the applied sample will spread out from the application site. The spot areas seen for the RP-TLC plates were smaller when compared to the UTLC, which varied from 0.89 – 1.59 mm^2 compared to 2.57 – 3.75 mm^2. The repeatability of the applied spot areas was lower for the UTLC plate than that for the RP-TLC plates over all the dye/acetone fractions used, however the highest repeatability was seen on the UTLC plate for a 100% dye fraction. This is due to the surface being highly hydrophobic, therefore reducing the spread of the applied aqueous dye sample.

When the separation capabilities of the UTLC platform are compared to that of a commercial RP-TLC plate under the same chromatographic conditions, the two plates show similar retention behaviours (Figure 6.8). The two dyes showed the same retention characteristics on both plates, with the Rhodamine 6G travelling further along each plate, while the Fast Green FCF was retained close to the initial spotting position. Total separation distances of 15 mm compared favourably to the RP plates which separated over 9 mm in the same time. Other UTLC platforms showed similarly

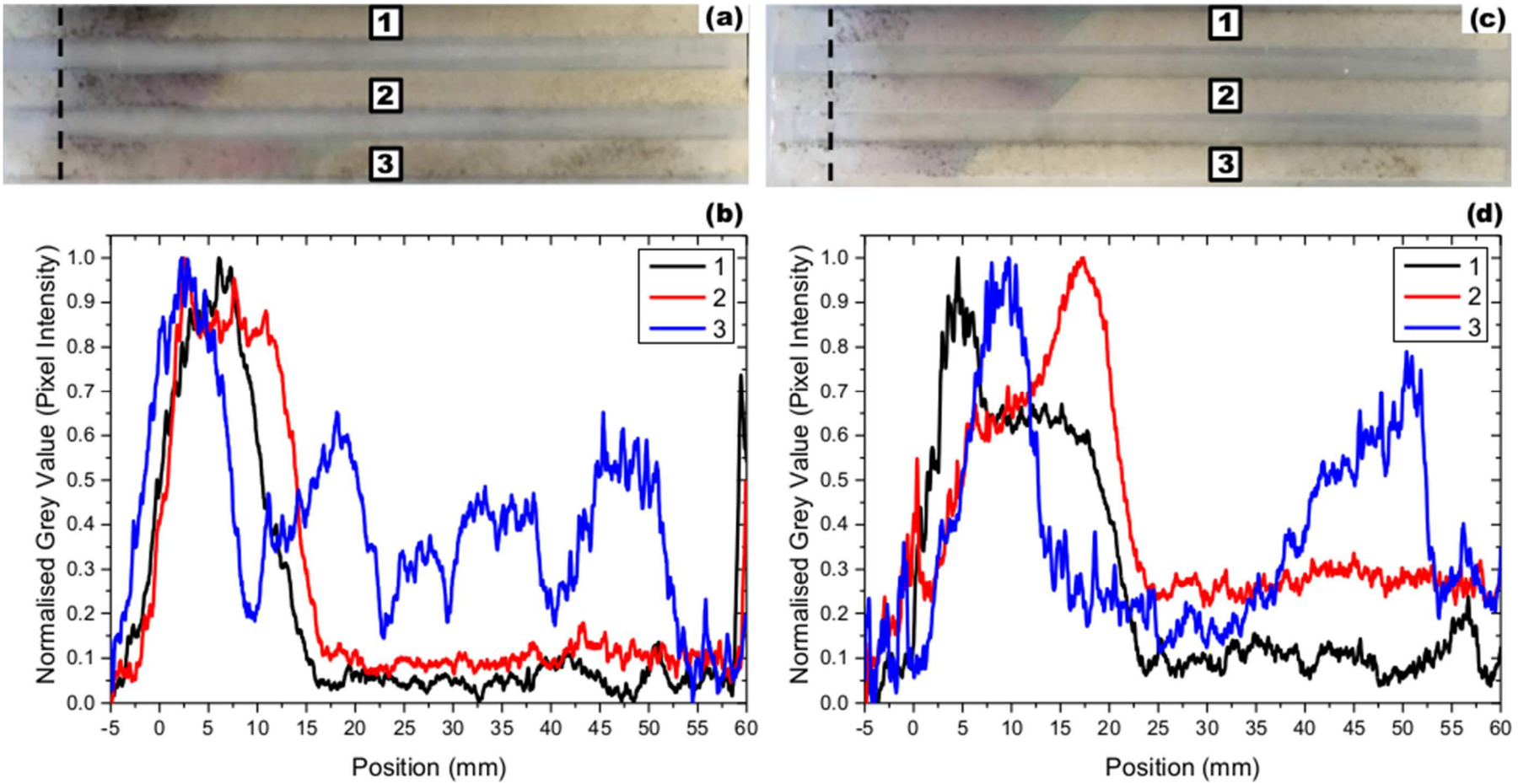

Figure 6.9: Post-separation images and resulting chromatograms of the UTLC platform using (a and b) Mobile Phase Composition 2 and (c and d) Composition 3 (c and) treatment for a 3-minute separation of Fast Green FCF and Rhodamine 6G, n = 3. Only one successful separation (number 3) was evident for MP2, however MP3 showed a streaking separation with the Fast Green having the largest retention factor.

short distances ranging from 5 mm on metal-oxide nanowire UTLC plates [11] to 30 mm on CNT-based plates [12].

Of note was the streaking characteristic of the UTLC plate, with some amount of dye being retained along a large segment of the microchannels. It may be possible to mitigate this though the use of longer separation times, thus allowing more mobile phase/analyte interaction. Another potential mitigation strategy is to ensure that the channels are fully cross connected. As shown in Figure 6.1, the channels with a positive angle (with respect to the direction of flow) are shallower than those with a negative angle. Optimisation of both the laser parameters and optical setup may allow for the fabrication of microchannels in both directions with the same dimensions thus allowing the dye to more easily move up the plate, while retaining the high solvent front repeatability of the 45° microchannels.

Changing mobile phase compositions resulted in significantly different retention behaviours. Though Mobile Phase Composition 2 only resolved the analytes in one separation from three, highlighting the importance of mobile phase selection in TLC. However, Composition 3 showed successful separations with the Fast Green having a higher R_f than the Rhodamine 6G. Again, this was similar to that shown for the RP-TLC plates, suggesting the UTLC plate has a reversed-phase functionality which stems from its surface functionality being similar to the hydrocarbon-based RP plate's functionality.

The COP used in this study was sourced at a price of €116.87/m^2 or a cost of €0.28/platform (80 mm × 30 mm) of three plates. The RP-TLC plates were sourced from Merck at a cost of €376.25 for 20 plates, or €14.69/plate, while plates fabricated via 3DP (Section 2.2.2) were reported at a cost of US$3.50/platform of three plates [10]. This illustrates how the laser fabrication technique is highly price-competitive in the fabrication of planar chromatography platforms.

6.5 Conclusions

In conclusion, this chapter presents the first investigation into the laser fabrication of a polymer-based planar chromatography platform. The laser fabricated UTLC plate performed in a similar manner when compared to a reversed-phase plate when separations were performed using a range of mobile phase compositions. Surface modification of the UTLC plates was successful as measured by changes in the

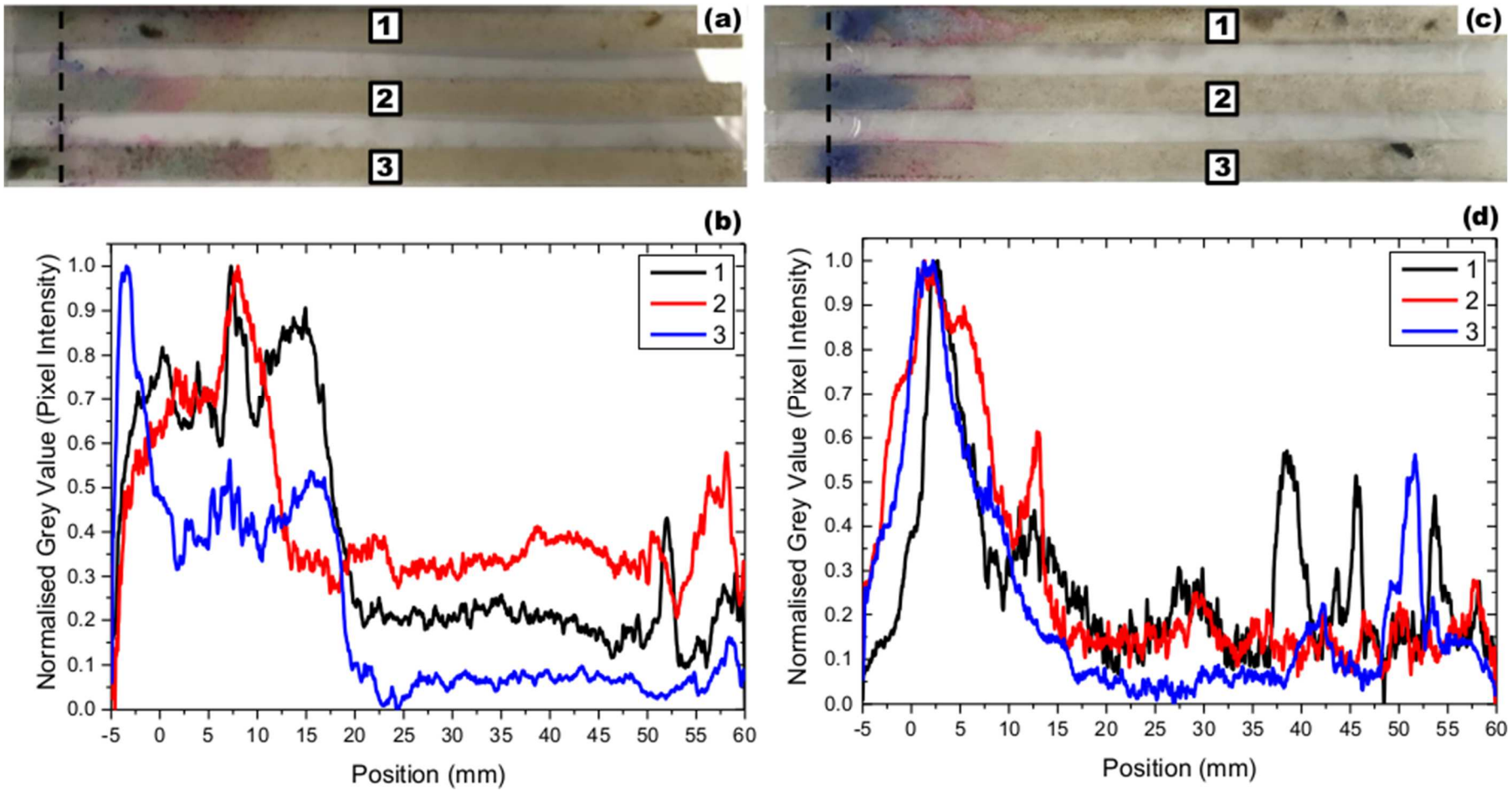

Figure 6.10: Post-separation images and resulting chromatograms of the UTLC platform (a and b) after plasma and (c and d) after APTES treatment for a 3-minute separation of the Fast Green FCF and Rhodamine 6G, n = 3.

retention behaviour of the plate post-modification. The ability to tailor the surface chemistry shows some scope for the adaptability of the UTLC plate, which would not be possible with traditional TLC plates consisting of porous layers. Furthermore, the UTLC plates exhibited a lower per device cost, two orders of magnitude lower than commercial RP-TLC plates, and one order of magnitude lower than 3D-printed plates. Overall, this work shows the promising capability for the development of planar chromatographic platforms fabricated via laser ablation.

References

[1] Khanarian G. Optical properties of cyclic olefin copolymers. Opt Eng. 2001 Jun 1;40(6):1024.

[2] Nunes PS, Ohlsson PD, Ordeig O, Kutter JP. Cyclic olefin polymers: Emerging materials for lab-on-a-chip applications. Microfluid Nanofluidics. 2010 Apr 7;9(2–3):145–61.

[3] Hansen M, Nilsson D, Johansen DM, Balslev S, Kristensen A. A nanoimprinted polymer lab-on-a-chip with integrated optics. In: Goodman TD, editor. Proceedings of SPIE. San Diego, CA., USA: Advancements in Polymer Optics Design, Fabrication, and Materials; 2005. p. 58720A.

[4] Trichur R, Kim S, Lee SH, Abdelaziez YA, Starkey DE, Halsall HB, et al. A New Plastic CE Chip with Wide Optical Clarity Using Cyclic Olefin Copolymers (COC). In: Micro Total Analysis Systems 2002. Dordrecht: Springer Netherlands; 2002. p. 560–2.

[5] Saaem I, Ma K-S, Marchi AN, LaBean TH, Tian J. In situ Synthesis of DNA Microarray on Functionalized Cyclic Olefin Copolymer Substrate. ACS Appl Mater Interfaces. 2010 Feb 24;2(2):491–7.

[6] Hwang S-J, Tseng M-C, Shu J-R, Her Yu H. Surface modification of cyclic olefin copolymer substrate by oxygen plasma treatment. Surf Coatings Technol. 2008 Apr;202(15):3669–74.

[7] Raj J, Herzog G, Manning M, Volcke C, MacCraith BD, Ballantyne S, et al. Surface immobilisation of antibody on cyclic olefin copolymer for sandwich immunoassay. Biosens Bioelectron. 2009 Apr;24(8):2654–8.

[8] Roy S, Yue CY, Lam YC, Wang ZY, Hu H. Surface analysis, hydrophilic enhancement, ageing behavior and flow in plasma modified cyclic olefin

copolymer (COC)-based microfluidic devices. Sensors Actuators B Chem. 2010 Oct;150(2):537–49.

[9] Cortese B, Mowlem MC, Morgan H. Characterisation of an irreversible bonding process for COC–COC and COC–PDMS–COC sandwich structures and application to microvalves. Sensors Actuators B Chem. 2011 Dec;160(1):1473–80.

[10] Macdonald NP, Currivan SA, Tedone L, Paull B. Direct Production of Microstructured Surfaces for Planar Chromatography Using 3D Printing. Anal Chem. 2017 Feb 21;89(4):2457–63.

[11] Bezuidenhout LW, Brett MJ. Ultrathin layer chromatography on nanostructured thin films. J Chromatogr A. 2008 Mar 7;1183(1–2):179–85.

[12] Jensen DS, Kanyal SS, Madaan N, Miles AJ, Davis RC, Vanfleet R, et al. Ozone priming of patterned carbon nanotube forests for subsequent atomic layer deposition-like deposition of SiO_2 for the preparation of microfabricated thin layer chromatography plates. J Vac Sci Technol B, Nanotechnol Microelectron Mater Process Meas Phenom. 2013;31(3):31803.

Chapter 7
Conclusions and Outlook

7.1 Conclusions

The aim of this thesis stated in Chapter 1 was:

A technique based around laser-material processing can be developed, such that microstructured planar chromatographic platforms can be fabricated which are effective relative to commercial platforms, as evidenced by proof-of-concept applications of said platforms for organic chemical separations.

This was successfully achieved through a number of individual investigations around the theme of laser ablation of COP and finally the application of a microchannel-structured polymer surface towards organic dye separation.

The examination of laser ablation on ZeonorFilm ZF14 COP utilising an Nd:YAG laser was found to be a successful technique for the fabrication of v-shaped microchannels ranging from 12 – 47 µm in depth and 44 – 155 µm in width. Also examined was the use of multiple laser passes to further extend the process space with the resultant microchannels ranging from 22 – 77 µm in depth and 59 – 155 µm in width for up to 11 laser passes. There were minimal changes in terms of surface chemistry as investigated via ATR-FTIR and Raman spectroscopy, with some dehydrogenation and carbonisation of the microchannel surface found. This examination was then extended to include the development of a Taguchi method model, to fully investigate the process space. An examination of the interaction of laser fluence, number of laser passes and laser beam scan speed was performed on two grades of COP (ZeonorFilm ZF14 and ZF16), with two thicknesses of ZF16 examined.

In the course of this work, a new method for the deposition of nanostructured material coatings at ambient conditions was implemented and termed “Confined Atmospheric Pulsed Laser Deposition”. The CAP process allows for the rapid and scalable deposition of nanomaterial thin films, and was applied to the deposition of nanostructure gold on the COP substrates. The deposited gold was plasmonic in nature, and film thicknesses up to tens of microns were observed. Though this technique was not applied for the deposition of functional coatings for chemical separation, it could in future allow the rapid functional of the UTLC platform with a range of nanomaterials. The CAP process also has applications towards the fabrication of electrochemical sensors and optically active coatings.

Finally, a proof-of-concept was achieved for a microchannel-based polymer UTLC platform with the separation of an organic dye mixture. The UTLC platform was compared to a commercial reversed-phase TLC plate, with similar dye retentions found. The provision to further functionalise the surface via chemical- and plasma-surface modification was examined, with changes to the dye retentions found, thus allowing the possibility to tailor the UTLC plate to separations. Plasma modification showed significant changes in the separation distances, with the modified UTLC plate showing separation distances twice that of the untreated plate under the same chromatographic conditions. Chemical functionalisation with APTES resulted in only one of the two analytes being resolved, which may be a result of an aminated surface being unsuitable for the separation of the chosen dye mixture.

7.2 Outlook and Future Work

The UTLC platform developed in this thesis has large scope for further application in separation science. Though proof-of-concept was achieved, as was the goal of the project, there remains a number of challenges to fully realise the platform as a competitive alternative to existing technologies.

Further optimisation of the laser process could allow for faster manufacturing times. Changes to the optical setup, such as the implementation of beam shaping, and the use of faster pulse width lasers (into the low pico- or femtosecond range) would allow for a wider range of morphologies, while a switch to higher power lasers would reduce fabrication time. The fabrication process could also be optimised through the use of roll-to-roll processing of the polymer, rather than the current batch processing.

Furthermore, though not explored in any detail in this work, the application of nanomaterial coatings to the COP-based UTLC platform could allow for more targeted separations to be realised. Nanoparticles such as carbon nanotubes, fullerenes, silica and metal-oxide have been demonstrated in a wide range of chromatographic applications [1,2]. The CAP process described in Chapter 5 would allow for single step functionalisation of the platform using the same process. Furthermore, the incorporation of conductive material on the platform would allow for the possibility of electrochemical detection to be coupled for combined separation and sensing in a single platform. Previous work on nanoparticle functionalisation of COP has been demonstrated for the creation of biomimetic platforms using drop-cast carbon nanoparticles on microchanneled COP [3]. A similar technique may allow for a simple functionalisation route for the UTLC separation platform. Though surface functionalisation was briefly explored in the form of both plasma and APTES treatment, further work is required to fully understand the extent of the capabilities of the modified plates. As mentioned in Chapter 2, amine-bonded silica gel stationary phases are particularly suited for the separation of compounds such as carbohydrates. An examination of the separation of such compounds using the UTLC plates may demonstrate this form of functionalisation as a viable route to extend the capabilities of the platform.

The separation of two diterpene molecules, cafestol and kahweol, have been noted of particular interest for future application of the laser-fabricated UTLC platform. Typically separated via HPLC, these compounds form a portion of the lipophilic fraction of brewed coffee. These diterpenes and their related compounds have been noted for their anticarcinogenic, antioxidant and hepatoprotective properties [4–7], however more recent studies have identified a causal link between cafestol and hypercholesterolemia [8]. Separation and quantitation of cafestol, kahweol and their derivatives in naturally occurring quantities allows for accurate examination of their effects on biological systems. Identification of their relative occurrence in various types of coffee beans also allows for both taxonomic classification and quality assurance checks in food. Application of the laser-fabricated platform towards diterpene separations would allow validation of the platform for the separation of highly similar compounds in an industrially relevant context. While this is just one example, the myriad of applications of current commercial TLC provide many possibilities for the future application of laser-produced UTLC platforms.

References

[1] Duan A-H, Xie S-M, Yuan L-M. Nanoparticles as stationary and pseudo-stationary phases in chromatographic and electrochromatographic separations. TrAC Trends Anal Chem. 2011 Mar;30(3):484–91.

[2] Nilsson C, Nilsson S. Nanoparticle-based pseudostationary phases in capillary electrochromatography. Electrophoresis. 2006 Jan;27(1):76–83.

[3] Bagga K, McCann R, O'Sullivan F, Ghosh P, Krishnamurthy S, Stalcup A, et al. Nanoparticle functionalized laser patterned substrate: an innovative route towards low cost biomimetic platforms. RSC Adv. 2017;7(13):8060–9.

[4] Lee KJ, Jeong HG. Protective effects of kahweol and cafestol against hydrogen peroxide-induced oxidative stress and DNA damage. Toxicol Lett. 2007 Sep 10;173(2):80–7.

[5] Lee KJ, Choi JH, Jeong HG. Hepatoprotective and antioxidant effects of the coffee diterpenes kahweol and cafestol on carbon tetrachloride-induced liver damage in mice. Food Chem Toxicol. 2007 Nov 1;45(11):2118–25.

[6] Kim HG, Hwang YP, Jeong HG. Kahweol blocks STAT3 phosphorylation and induces apoptosis in human lung adenocarcinoma A549 cells. Toxicol Lett. 2009 May 22;187(1):28–34.

[7] Cavin C, Holzhaeuser D, Scharf G, Constable A, Huber W., Schilter B. Cafestol and kahweol, two coffee specific diterpenes with anticarcinogenic activity. Food Chem Toxicol. 2002 Aug 1;40(8):1155–63.

[8] Halvorsen B, Ranheim T, Nenseter MS, Huggett AC, Drevon CA. Effect of a coffee lipid (cafestol) on cholesterol metabolism in human skin fibroblasts. J Lipid Res. 1998 Apr 1;39(4):901–12.

Appendix A

ANOVA Definitions

Table A1: Definitions for the terminology used in ANOVA analysis, as listed in the DesignExpert7 Software.

Parameter	Definition
Degrees of Freedom (df)	The number of levels in the term minus 1
Adjusted R-Squared	The measure of the amount of variation about the mean explained by the model.
Predicted R-Squared	The measure of how good the model predicts a response value.
Adequate Precision	The signal-to-noise ratio
F Value	A comparison of the model variance with the error variance
Sum of Squares	The sum of the squared deviations from the mean
Mean Square	The Sum of Squares divided by the Degrees of Freedom
p-value (Prob > F)	The probability of getting an F Value of this size if the term did not have an effect on a response
Residual	The portion of the Corrected Total Sum of Squares that could not be explained by the model.
Corrected Total (Cor Total)	The total of the Sum of Squares for the model corrected for the mean.